2014

Measurement of Fluid and Particle Transport through Narrow Passages

Christopher Ghazi
University of Vermont, cghazi@uvm.edu

MEASUREMENT OF FLUID AND PARTICLE TRANSPORT THROUGH NARROW PASSAGES

A Thesis Presented

by

Christopher J. Ghazi

to

The Faculty of the Graduate College

of

The University of Vermont

In Partial Fulfillment of the Requirements
for the Degree of Master of Science
Specializing in Mechanical Engineering

October, 2014

Accepted by the Faculty of the Graduate College, The University of Vermont, in partial fulfillment of the requirements for the degree of Master of Science, specializing in Mechanical Engineering.

Thesis Examination Committee:

_____ Advisor
Jeffrey S. Marshall, Ph.D.

_____
Yves Dubief, Ph.D.

_____ Chairperson
Britt A. Holmén, Ph.D.

_____ Dean, Graduate College
Cynthia J. Forehand, Ph.D.

Date: August 8, 2014

ABSTRACT

There are many instances where fluid and particles traveling through a narrow passage, such as a crack in a window or door, have large but sometimes unseen effects on our daily lives. For instance, in the cold months of the year a pressure gradient can exists between the inside and outside of a building which causes cold, outdoor air to flow inside through any cracks; significantly decreasing heating efficiency. This inflow of atmospheric air can bring with it dangerous contaminant particles to the inside of a building. Pollution can also occur inside a structure from internal sources of contamination, such as smoke generation from a fire. This thesis represents a two-fold examination of these phenomena.

The first part of the thesis showcases a method for local measurement of air leakage flow rate, which can be used to quickly assess leakage rates across a surface, such as a window. The method uses a small local enclosure with constant volume placed about a region on the structure under investigation, which is depressurized and injected with a small concentration of carbon dioxide as a tracer gas. The time variation of the pressure and carbon dioxide concentration inside the enclosure are monitored and used to quantify the leakage flow rate as a function of pressure difference. Because of the small size of the enclosure, advanced data processing techniques are necessary to reduce uncertainty in determination of the rate of change of the carbon dioxide concentration that arises from sensor variability. Results of a laboratory demonstration of the proposed leakage detection and characterization device are reported for the problem of leakage through a circular hole in a plate with prescribed pressure differences. Experimental results from the laboratory tests are found to be in excellent agreement with results of a numerical simulation of leakage flow through a hole, as well as predictions from a number of empirical equations for this problem found in the literature.

The second part of the thesis is a numerical study of particle capture in the entrance region of a crack, which is a phenomenon previously not well understood or accounted for in empirical correlations. The computational domain for laminar flow through a crack consists of the crack channel and both inlet and exit reservoirs that are much larger than the channel width. The simulations examined different mechanisms for particle capture within the channel entrance region, including collision on the inlet reservoir wall just outside the crack channel, collision within the crack channel due to cross-stream inertia imparted by the entrance flow, collision induced by Brownian diffusion both on the inlet reservoir wall outside of the channel and within the channel, and gravitational collision within the channel. A detailed study of the variation of the entrance penetration factor with parameters such as the Stokes, Peclet, and Froude numbers was performed, and comparison of the numerical predictions with different theoretical expressions were made when the latter were available. Validity of the assumption of penetration factor independence was also examined for cases where both entrance region inertia and gravitational settling are significant.

CITATIONS

Material from this thesis has been published in the following form:

Ghazi, C.J., Marshall, J.S.. (2014). A CO2 tracer-gas method for local air leakage detection and characterization. Flow Measurement and Instrumentation, 38, 72-81.

AND

Material from this thesis has been submitted for publication to the *Journal of Aerosol Science* on July, 18, 2014 in the following form:

Ghazi, C.J., Marshall, J.S.. (2014). Influence of the entrance region on particle capture during transport through a crack. Journal of Aerosol Science.

ACKNOWLEDGEMENTS

First and foremost, I would like to thank my advisor, Dr. Jeffrey Marshall. I am very grateful for all of the opportunities you have given me over the years. What I have learned working under you has been invaluable, and I am so thankful for the countless times you have put other things aside to assist me whenever I needed it. I would also like to thank Dr. Yves Dubief and Dr. Britt Holmén, not only for serving on my thesis committee but also giving me important input into my thesis work.

I want to thank my lab-mates and office neighbors Andy Furhmann, Curtis Saunders, Melissa Faletra, Adam Green, Simtha Sankaran, Kyle Sala, and Ian Pond for all the great times, coding help, homework sessions, and conversations we have had over the last few years. Sometimes just talking a problem through with you guys was all I needed to find a solution.

I would like to thank Alex Vizard, who was instrumental in the early stages of the leak measurement design, as well as Kurt Anthony and Carl Silver for assistance with measurement instrumentation and construction of the experimental apparatus. This work was funded by the National Center for Preservation Technology, an office of the National Park Service, under grant P11AC71049 and by the U.S. National Science Foundation under grant CBET-1332472.

TABLE OF CONTENTS

Page

LIST OF FIGURES

Figure Page

CHAPTER 1: INTRODUCTION

1.1. Motivation

There are many aspects in engineering which deal with a fluid flowing through a narrow passage. In many cases this represents a carefully controlled environment, such as microfluidic flows, radiators, filtration devices, and other such applications. However, flow through a narrow passage is also a component of several unwanted or harmful processes. Most notably are cases of flow through cracks, gaps, leaks, etc., passing across a boundary that is intended to be air-tight. Such flows can also give rise to transport of particles and other contaminants, often undesirable or even harmful, through these cracks.

One of the biggest contributions to domestic energy loss, often times unseen or unknown to many people, is airflow through cracks in windows, doors, joints, etc., in houses and buildings. Air will flow through such cracks in a building when a gradient of pressure is seen between the inside and outside of the building, and is often defined as air infiltration. While there are many phenomena that can cause such a pressure difference, the two main causes of air infiltration are wind acting on the outside of a building and temperature differences between the inside and outside of the building (Lyberg 1997). Fluid forces from wind can cause regions of high pressure on the outside of a building, causing a significant pressure difference between the inside and outside of the building. This pressure difference causes an inflow of atmospheric air into the building through any cracks or gaps in the building structure.

Similar pressure differences can alternatively be caused by temperature differences between the inside and outside of a building, leading to a type of air infiltration often called the ‘stack effect’. A difference in temperature between the inside and outside of a building introduces a two-fold mechanism for air infiltration. First, the heating or cooling of air inside a building necessitates convective air movement that will create low/high pressure regions inside. This leads to pressure differences between the inside and outside of the building and consequent air infiltration. Secondly, temperature differences will cause gradients in air density, where colder, more dense air will have a preference to flow to areas of low density via cracks in the building.

Air infiltration via these mechanisms, especially in the stack effect, is most prevalent in the “heating season” of the year, where colder outside temperatures call for heating of homes and buildings. Hot air rises inside of a building, causing a low pressure zone towards ground level and cold air infiltration into the building through cracks, augmented by the gradient in density between the warm inside air and the cold outside air. This effect of cold air entering the building can be enhanced by wind pressure on the outside of the building. Excess air infiltration in such a manner is one of the leading causes of domestic heat and energy loss. A study performed by Liddament and Orme (1998) reported statistics from tests across multiple counties on energy loss through air infiltration. They stated statistics from member countries of the Organization for Economic Co-operation and Development which concluded that, depending on climate conditions and presence

of leaks, upwards of 50% of heating energy can be lost via air infiltration. In a look at the United States alone, a report by Sherman (1980) on energy loss across all sectors found that approximately between 6 and 9% of the Nation's total energy budget is lost due to air infiltration. The detection and repair of significant leakage areas thus has the potential to produce huge energy saving. While it can be extremely costly or aesthetically destructive to perform entire-building upgrades, there is a need for localized detection of leak sites for problem-areas in air infiltration.

Leakage of a fluid or gas can also have large consequences on a myriad of other industries. One of the most common examples is storage of compressed gases, in which case a leak could be costly through a loss of stored gas, dangerous if the gas in question is toxic, or, if the leak is big enough, cause propulsion of a gas cylinder. Leaks in pipelines of fluids such as natural gas can be costly, environmentally polluting, and extremely dangerous due to the explosive nature of the gas. Industrial vacuum equipment, such as that used in nuclear power, has extremely high standards for leakage. The event of a leak in such equipment could lead to a dangerous radiation release, and consequently leak detection is a required and integral part of the system. For manned spaceflight, it is imperative that a spacecraft be leak-free in order to retain oxygen for astronauts. Impacts, such as that of debris or small meteorites, can easily cause a threatening leak in such a spacecraft. Leak detection is therefore a serious priority in any manned spaceflight.

For all of these issues, detection of leakage rates and locations in a timely fashion is paramount for conservation and safety. There are a number of existing techniques that are used to analytically estimate or physically test for gas leakage; however, such techniques often trade-off design parameters such as accuracy, flow measurement capabilities, and detection of specific leakage locations (as will be discussed in Chapter 2).

Fluid traveling through cracks, leaks, gaps, etc., can also bring with it potentially harmful or unwanted particles. Smoke traveling through a building during a fire is a prime example of fluid and particle propagation through cracks. Building fires, especially when the fire is contained to certain regions or rooms, create large gradients of temperature and pressure between zones in a building. This causes air and smoke particles to have high flow rates through any cracks or gaps in doors, junctions, windows, etc. Smoke can spread through a building quickly via this conduit. During a building fire, the most common cause of human death is from smoke inhalation, rather than a result of burns, due to the many toxins found in smoke, including cyanide among others (Jones et. al. 1987). Between 50 and 80% of deaths in fires can be attributed to smoke inhalation from the propagation of smoke between rooms during a fire. Aside from the obvious hazards to life, smoke can travel into cabinets and chests, ruining the contents inside. In a similar matter, dust and smoke infiltration into containers of precious objects (such as museum displays) can be a cause for degradation of its contents.

Along with a potential loss of energy, air infiltration into buildings can also bring with it damaging or harmful particles. Atmospheric contaminants, such as dust, allergens, pollutants, tobacco smoke, and even radioactive materials can all be transported into buildings via air infiltration. Over time, particles and other contaminants can build up inside buildings, particularly in places such as large urban centers with poor atmospheric air quality, leading to dangerous exposure levels for building residents. There are many sources of particular matter which can cause adverse effects to the human body (Arden-Pope and Dockery 2006, Owen and Ensor 1992), all of which can enter residences via leaks in windows, doors, and joints. The realization of this danger has prompted numerous studies into particle infiltration into buildings, especially in urban areas of high pollution such as Los Angeles, CA and Hong Kong (Sarnat et. al. 2006, Tung 1999). Besides harmful particles, air infiltration into building through cracks can also carry with it water droplets that are damaging to the building structure.

With such a great number of potential issues surrounding particle infiltration through cracks, there is a need to understand, measure, and model both fluid and particle infiltration rates. However, existing methodologies and models are basic and often neglect important physics. As will be discussed in Chapter 2, the leakage detection methods are often inaccurate and of only qualitative value, and the analytical models for particle infiltration omit the important effect of the crack entrance region in estimating particle capture during transport through cracks.

1.2. Objective and Scope

This thesis conducts a two-fold examination of the propagation of fluid and particles through narrow passages, such as through a crack in a window. The first part focuses on experimental measurement of fluid transport through leaks, while the second part focuses on numerical modeling of particle capture during transport through such a passage. As such, the body of the thesis is split into two chapters, relating to these two areas of study.

The first part of the thesis presents and examines the accuracy of a local tracer-gas method for detecting and characterizing leakage flow rate through a select region in a structure, which might correspond to hatch or window, or some other trouble-prone part of a larger structure. A small enclosure was used for this problem in order to minimize the time required for the measurement and to allow the tests to be more local and less disruptive to system use. However, use of a small enclosure for a tracer-gas leakage test also poses significant difficulties. The most significant of these is the fact that the tracer gas concentration measurements are subject to significantly more noise than for larger-scale tests, which is particularly challenging because the leakage rate is dependent on the time derivative of the tracer gas concentration. Advanced data filtering and smoothing techniques are presented to overcome this difficulty, and the resulting method is validated against both numerical simulations and existing empirical correlations for leakage through a circular hole.

The second part of the thesis examines the effect of the entrance region on capture of particles passing through a rectangular crack. The effect of particle inertia, Brownian motion, and gravitational settling on flow near the entrance region are all examined. The validity of the common assumption that the effects of inertia and gravitational settling can be modeled by multiplying penetration factors which represent capture due to each effect individually (e.g., Liu and Nazaroff, 2001) is also examined. The reason for studying particle transport and capture in crack entrance regions is twofold - (1) particle transport and capture within crack entrance regions is not well understood and (2) some interesting particle dynamics occurs within the entrance region for finite-inertia particles. By contrast, diffusive and gravitational capture of particles within straight channels are well understood problems governed by simple dynamics. The study employs a computational approach that uses a finite-volume code to compute two-dimensional fluid flow and a particle dynamics model to compute particle transport within a computational domain consisting of a thin crack and rectangular inlet and outlet reservoirs. The particle dispersion relative to fluid streamlines is dominated by the large streamline curvature at the entrance to the passage, which is particularly acute near the corners where the inlet reservoir meets the crack channel. The drift of particles relative to the fluid streamlines within the entrance flow both modifies the capture of particles near the mouth of the crack and it influences the initial distribution of particles at the channel inlet.

Chapter 2 of the thesis gives a review of literature for both of the topics under investigation. Chapter 3 of the thesis examines the local tracer-gas method for leak detection, and contains several sub-sections which provide an overview of the experimental and numerical methods used, presents the data reduction methods used and uncertainty estimates, and describes and validates the results of the proposed leakage sensor approach. Chapter 4 of the thesis focuses on particle capture in the entrance region of a channel, with a computational domain that includes both inlet/outlet reservoirs and the crack channel. The chapter includes a description of the computational methods used for fluid and particle flow simulations, results with varying Stokes and Peclet numbers, and comparison with previous analytical theories. Chapter 5 presents conclusions and discusses possible future work to be done on these studies.

CHAPTER 2: LITERATURE REVIEW

Reflecting the two-part nature of the thesis research, the literature review is split into two sections. Section 2.1 is an account of literature pertaining to measurement of fluid leakage through cracks or gaps, including measurement techniques as well as empirical estimations. Section 2.2 is a review of the literature pertaining to particle infiltration through cracks as well as estimations of models for predicting penetration factor.

2.1. Detection and Measurement of Fluid Leaks

With gas leakage having significant effects on a number of industries, it is not surprising that a number of techniques have been developed to detect or measure gas leakage. These techniques vary drastically depending on the manner and fluid involved with the leak, with some techniques focusing more on leakage detection and others focusing on quantification of leakage rates. This section reviews current leakage detection and measurement techniques, as well as analytical estimations for fluid leakage rate.

For measurements of air infiltration into and out of buildings, there are currently two industry-standard techniques. Guidelines for the proper usage of these techniques are set by ASTM International (formerly the American Society for Testing and Materials, ASTM) (ASTM E1186, 2009). The first, and arguably most common, testing technique is the ‘blower door test,’ involving pressurization or depressurization of a building or subsection of a building and measurement of fan

flow rates required to maintain this pressure. The second, more accurate technique is known as the 'tracer-gas dilution method,' involving the injection of some gas other than air into the building zone and monitoring of its concentration as a function of time. Benefits and drawbacks of each of these methods are discussed below.

Specific standards for using a blower door test in residences or buildings are given by ASTM International (ASTM E1827). This technique is a modification of the fan pressurization technique for quantifying air leakage (ASTM E779). This method utilizes a 'blower door,' which is placed in an entry to the building or zone under consideration. This blower door has strong fans which can blow air into or out of the zone in order to pressurize or depressurize it. By measuring the pressure inside and outside of the zone and the flow rate of air through the blower door, leakage flow rate can be found. A sample schematic of this method can be seen in Figure 1. Additionally, pressure measurements are taken before and after testing, with all accessible ports to the zone open and the blower door turned off. Combining the pressure measurements with temperature and altitude readings, air density and viscosity can be calculated during testing both inside and outside of the zone. The industrial standard for blower door tests is to set the pressure difference between the zone and the outside air to 50 Pa (ASTM E1827). Air leakage through the zone envelope at constant pressure can be related to the flow rate of air through the blower door and the ratio of inside to outside air density. For depressurization, total envelope leakage flow rate Q_{env} can be calculated

$$Q_{env} = Q_{fan} \frac{\rho_{in}}{\rho_{out}}, \tag{2.1}$$

where Q_{fan} is the recorded flow rate through the blower door, ρ_{in} is the calculated air density inside of the zone, and ρ_{out} is the calculated density outside of the zone.

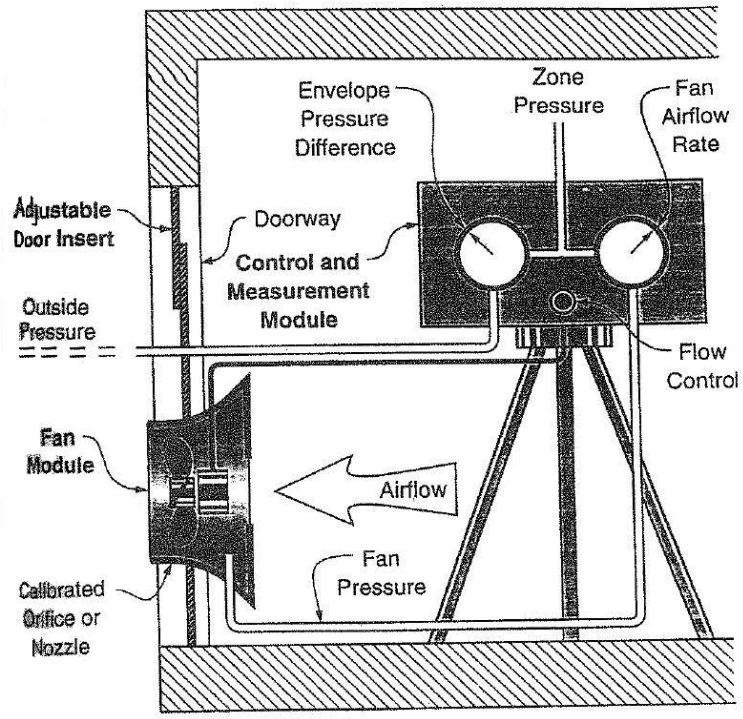

Figure 1. Simplified schematic of the blower door test method as stated by ASTM International (ASTM E1827).

The blower door test is a simple way of quantifying the presence of leaks in buildings; however, it has many drawbacks. First and foremost, this test only collects leakage data for the entire building or subsection under examination.

Information about leakage through localized sites, such as individual windows or doors, cannot be determined. This type of building-wide test disrupts normal usage of the building, effectively 'shutting down' the area in order to maintain proper testing conditions. Testing is also only performed at a single, specified pressure difference which does not represent the range of actual conditions to which buildings might be subject (ASTM E779, E1827). Data taken from blower door tests are really only for comparison's sake; overall rates of building leakage can be inferred from comparison to other testing data.

Many other issues can arise involving sensitivity to testing conditions and uncertainty in testing results. Natural pressure differences due to wind and stack effect can greatly skew blower door testing data, so testing can only be performed during times of mild temperatures and low wind (ASTM E1827). Depending on local climate, this can drastically limit the timing of implementing blower door testing. These tests can also be sensitive to leakages through the blower door itself, requiring further testing or compensation (ASTM E1827). Such sensitivities to testing conditions introduce high levels of uncertainty in results given by the blower door method.

A study into uncertainty estimations for various blower door tests was performed by Sherman and Palmiter (1995). In this study, three main sources of uncertainty were examined: precision error, bias error, and modeling error. Precision error is related to repeatability of results and can be defined using the standard deviation of multiple testing results. Bias error is caused by systematic

differences between the tests and actual operating conditions of the building. In the case of the study performed by Sherman and Palmiter (1995), this error is unknown and is therefore estimated using uncertainty propagation. The last type, modeling error, refers to the uncertainty involved in using an imperfect model (equation) to calculate flow rate from pressure difference. Sherman and Palmiter (1995) employed an analytical approach to calculate total uncertainty. Using individual values of uncertainty from the three sources mentioned above, they found total uncertainty using uncertainty propagation. Individual uncertainty values for precision and bias were taken from minimum standards of uncertainty in measurement equipment outlined by ASTM International (ASTM E779). Uncertainty from modeling error was found analytically from equations used to calculate flow rate from pressure difference.

Results of this study indicated that uncertainties in blower door test measurements are extremely sensitive to the chosen testing conditions. Strictly following procedures outlined by ASTM International (ASTM E779), Sherman and Palmiter (1995) found that, for the range of pressure differences used, uncertainty could vary between 7 and 45% of the measured value (with a 95% confidence level). Some improvements were suggested for lowering of uncertainty, including the use of alternative testing equipment and pressure ranges used in testing. A number of different combinations of equipment and testing conditions were examined, but even so, total uncertainty of these measurements ranged from 13 to 38% of the measured value.

The second main technique for measurement of air leakage in buildings, the tracer-gas dilution method, is less used than the more popular blower door test (ASTM E741). The basic principle behind these tests is that some tracer-gas is injecting into the space under examination such that its concentration is significantly higher than that in normal atmospheric air (or not found in air at all). As clean, atmospheric air enters the zone being testing, the tracer-gas concentration will fall, and leakage flow rates can be calculated in a number of ways. ASTM International lists three different tracer-gas dilution techniques, each with their own strengths and weaknesses. These techniques are the concentration decay method, the constant injection method, and the constant concentration method (ASTM E741).

The constant decay method is the most basic and easiest to perform out of the three methods (ASTM E741). It involves injecting a set amount of tracer gas into the building or zone under investigation. Concentrations across multiple areas of the zone are monitored until the concentration is approximately uniform. Then, data collection of tracer-gas concentration is performed. As clean, atmospheric air enters the zone through any cracks, the tracer-gas concentration decreases. Concentration levels are recorded periodically for a set amount of time. The total testing time is dependent on leakage flow rate and minimum required testing times can range between 15 minutes to four hours (ASTM E741). It should be noted that these times do not include the time it takes for the initially injected tracer gas to reach an approximately uniform concentration distribution. A simplified schematic

for testing procedures using the concentration decay method can be seen in Figure 2.

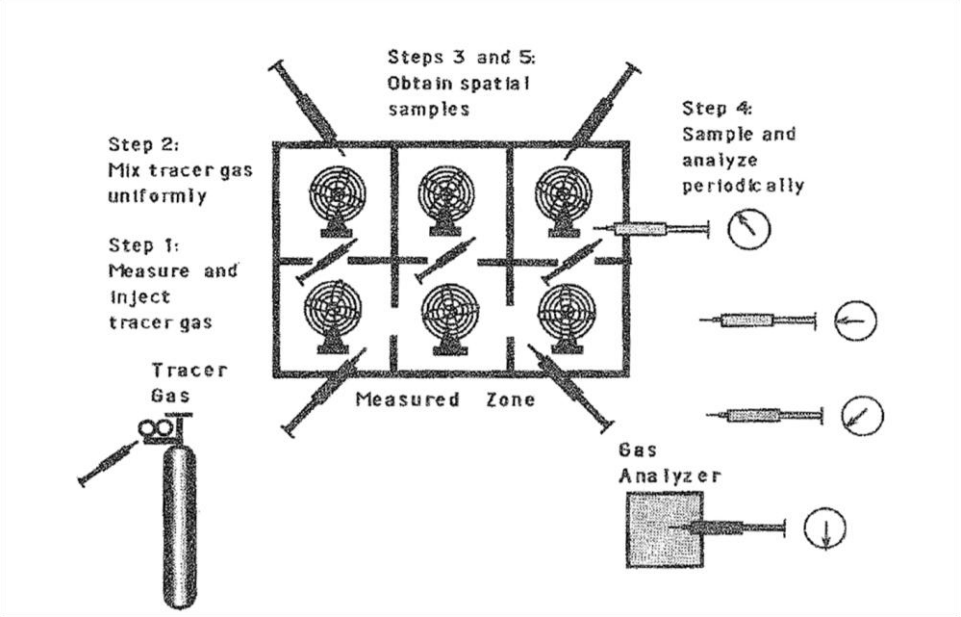

Figure 2. Simplified schematic and procedure of constant concentration decay method as stated by ASTM International (ASTM E741).

After significant concentration data has been collected, an average leakage flow rate can be calculated using the assumption that concentration decay follows a logarithmic pattern (ASTM E741). Under this assumption, the concentration profile should vary as a function of time according to

$$\ln C_i(t) = -A_{CDM}t + \ln C_i(0), \tag{2.2}$$

where $C_i(t)$ is the concentration of tracer gas inside of the zone under investigation, $C_i(0)$ is the concentration at the initialization of data collection, and A_{CDM} is an

empirically found mean air exchange rate (which can be converted into leakage flow rate), which has units of 1/s. Linear regression can be performed on the data collected from the concentration decay method to fit a profile for (2.2) and estimate the value of A_{CDM} for the given zone and testing condition. An example of this regression can be seen in Figure 3.

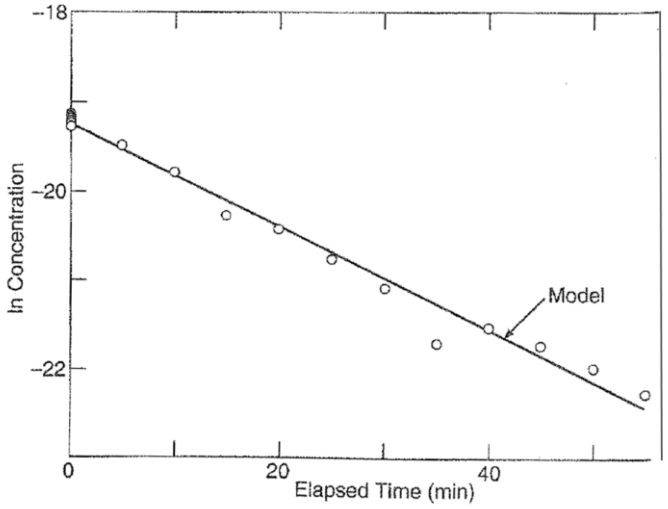

Figure 3. Example regression of logarithmic concentration data taken from a concentration decay method test (ASTM E741).

The second tracer-gas dilution method outlined by ASTM International is the constant injection method. This method is very similar to the concentration decay method, except the tracer gas is injected at a constant flow rate Q_{tracer}. This method calculates an average leakage flow rate for the testing duration. Otherwise, the testing procedure is the same; a simplified schematic of the testing using the

constant injection method can be seen in Figure 4. Calculation of the average volumetric leakage flow rate, Q_{avg}, is found using

$$Q_{avg} = Q_{tracer} \frac{1}{C_{avg}} - \frac{V_{zone}}{\Delta t} \ln\left[\frac{C_2}{C_1}\right], \tag{2.3}$$

where C_{avg} is the average tracer-gas concentration (volumetric percentage) over the testing period, V_{zone} is the total volume of the zone under investigation (must be estimated), Δt is the total time elapsed during data measurement, and C_1 and C_2 are the concentrations taken at the beginning and ending of testing, respectively.

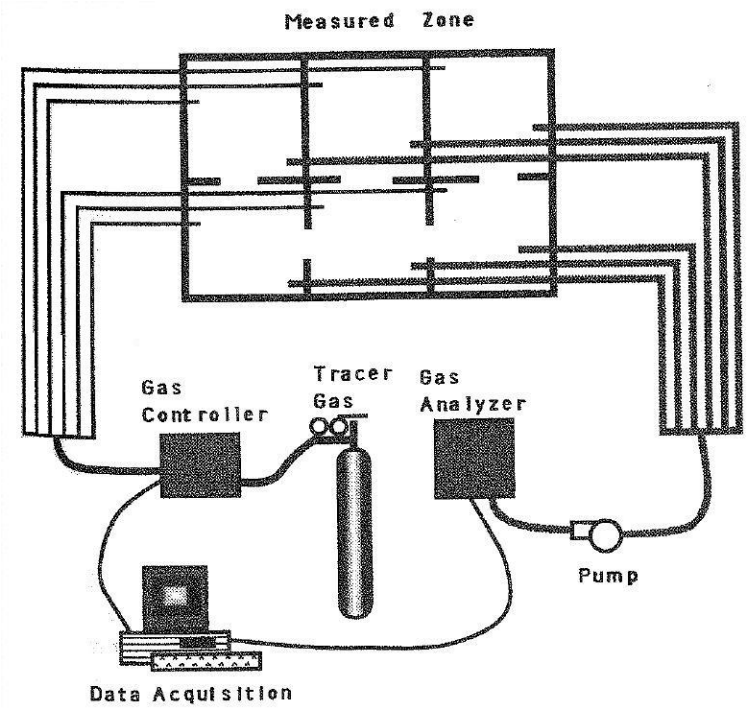

Figure 4. Simplified schematic and procedure of constant injection method as stated by ASTM International (ASTM E741).

The last tracer-gas dilution method discussed by ASTM International is the constant concentration method (ASTM E741). This is a slightly different than the first two approaches, where injection of the tracer gas is controlled such that the concentration in the zone remains roughly constant. Similarly to before, tracer gas is injected into the zone and monitored at N different sites around the zone until a uniform concentration has been obtained. Then, as atmospheric air enters the zone through cracks (which would cause the tracer gas concentration to decrease), a computer is used to change the injection rate of tracer gas such that the average concentration across all monitoring sites remains a constant value C_{target} (volumetric percentage). Data of actual concentration is monitored across all concentration sensors for a set amount of time, with sampling performed at least every five minutes (ASTM E741). A simplified schematic of this method can be seen in Figure 5. Leakage flow rate, as a function of time, can be calculated with

$$Q_{avg} = \frac{\sum_{i=1}^{N} Q_{tracer}(t,i)}{C_{target}}, \tag{2.4}$$

where i is an index relating to each concentration sensor.

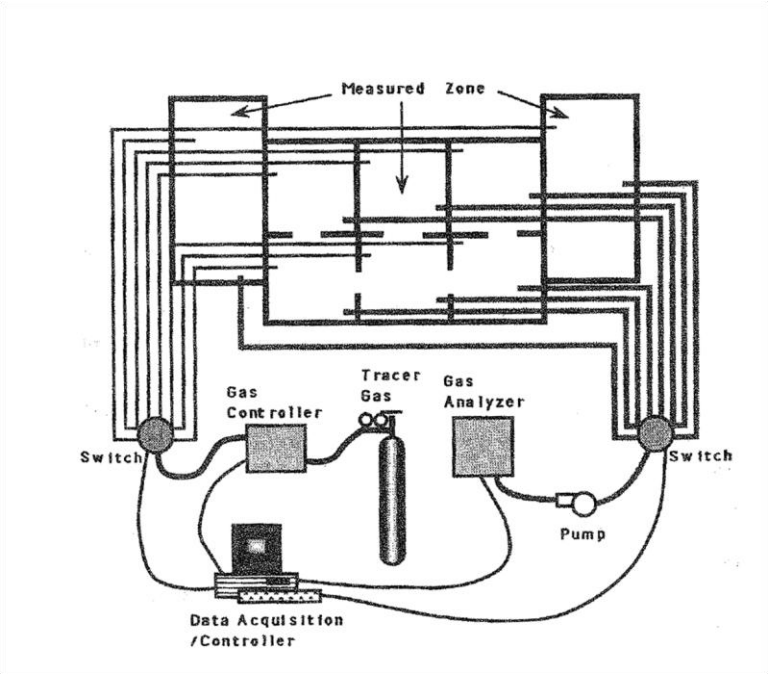

Figure 5. Simplified schematic and procedure of constant concentration method as stated by ASTM International (ASTM E741).

The tracer-gas dilution method offers improvements in measurement accuracy over the blower door test. For one, it can measure leakage due to the actual conditions buildings will face in their use. Measurement data taken from tracer-gas dilution tests are also more accurate than that of blower door testing. However, this method has a number of the same issues as the blower door test, as well as some others. Like the blower door test, the tracer-gas dilution method disrupts the normal use of the area under investigation and has no localized measurement of air leakage. Depending on the gas used for testing, post-test fumigation may also be required. This test also requires a significant amount of time for the system (building) to come to a steady state condition before recording

of data may begin (ASTM E741). Additionally, testing over such a large area as a building or subsection brings up questions of tracer-gas concentration non-uniformity. Furniture, nooks, crannies, recirculation regions, etc. can cause local differences in tracer-gas concentration, falsifying one of the key assumptions used in leakage measurement via the tracer-gas dilution test (Sherman 1988). These differences in concentration can have the potential to cause large systematic error in the recorded measurements. Accurate estimation of this error can be challenging because physical mechanisms behind this problem are extremely complex. This leads to the neglecting of this form of error, such as was done in the analytical study of uncertainty in tracer-gas dilution tests by Sherman (1988).

While uncertainty in measurements by tracer-gas dilution tests can be lower than that of blower door tests, depending on testing conditions they can still be fairly high. Sandberg and Blomqvist (1985) ran a number of tests of the tracer-gas dilution method in order to estimate uncertainty in their measurements. There were 21 tests were performed for two of the standard tracer-gas dilution methods; the decay method and the constant concentration method. One ‘test house’ was used for all trials, which was a single story building with five different rooms. Flow between rooms as well as from outside air was monitored at different flow rates. Outside air was supplied via two sets of in/out ducts which could control flow rate of air into the house. A schematic view of the test house can be seen in Figure 6. Varying numbers of fans were placed inside the house to test mixing. Results from the tests concluded that uncertainty for the decay method of the total house was 11±6%.

However, the authors noted that, when examining flow rate by a room to room basis, certain rooms had more errors than others. The 'worst case scenario' room had an uncertainty of 16±7%. Uncertainties for the constant concentration tests were lower, with a best case scenario of 6±3%. The authors state, however, that these values are probably underestimates of the true uncertainty. This is because, as discussed by Sherman (1988), a uniform tracer-gas concentration could not be achieved and wasn't accounted for in the uncertainty calculations.

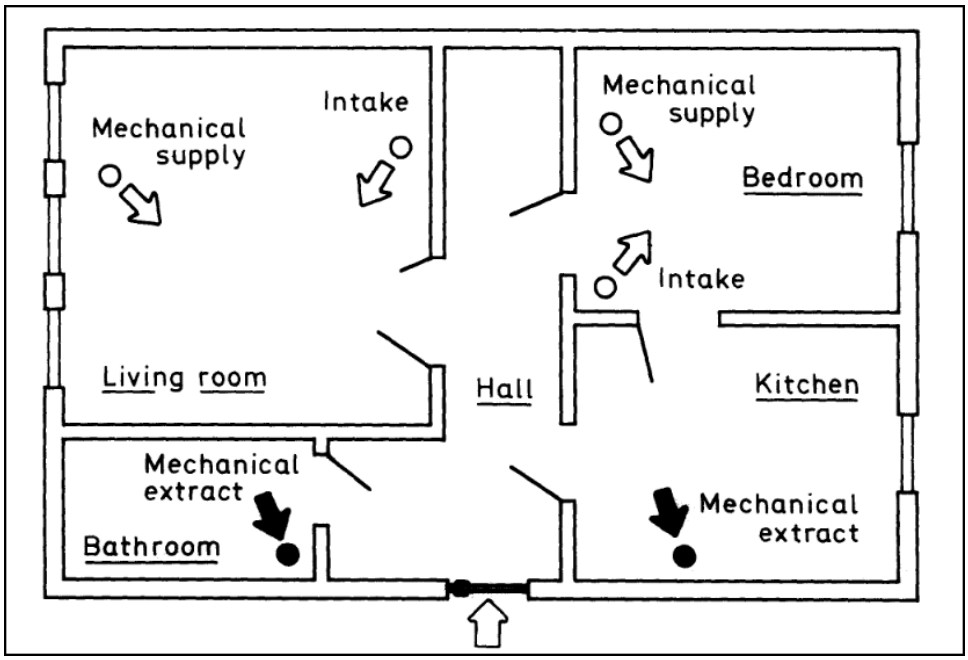

Figure 6. Schematic drawing of building used in uncertainty tests by Sandberg and Blomqvist (1985). Controlled air flow in and out of the building is shown as mechanical supply and mechanical extract, respectively.

Separately from the use of physical testing inside of a building in question, rough estimates of air infiltration can be calculated using analytical approximations.

If a pressure difference across the building envelope is known (or estimated analytically), flow rates through leaks can be found by assuming that the total area of leakage cracks can be combined into an effective leakage area (ELA) of a circular orifice (Sherman 1987). Many empirical equations have been developed to estimate flow rates through such orifices. The most common equation used is known as the power law relationship (Sherman 1987), where volumetric flow rate Q is given by

$$Q(\Delta P) = C_{PL}\Delta P^{n}, \tag{2.5}$$

where ΔP is the pressure difference across the building envelope, C_{PL} is the leakage coefficient, and n is the leakage exponent. Values for C_{PL} and n are generally found empirically, and C_{PL} has units of $m^{n+3}s^{2n-1}/kg^{n}$. There are other, more accurate models for predicting flow rates; however, these will be discussed in more detail in Section 3.3 of this thesis.

As this method requires knowledge of ΔP, various correlations have been developed to calculate a pressure difference from common environmental factors, such as wind pressure and the stack effect. These two effects can have highly non-linear interactions with each other when causing pressure differences and flow rates through cracks. A study by Walker and Wilson (1993) investigates four different analytical techniques for estimating combined leakage flow rates. All of these techniques involve calculating contributions from wind and stack effects separately,

and then combining their results. Pressure difference from the stack effect, ΔP_s, is given by

$$\Delta P_s = \rho_{out} g (h_s - h_o) \frac{\Delta T}{T_{in}}. \tag{2.6}$$

Here, ρ_{out} is the density of outside air, g is gravitational acceleration, h_s is the height at which the pressure is being calculated, h_o is the height at neutral pressure, ΔT is the temperature difference between the inside and outside air, and T_{in} is the temperature of the inside air, in absolute units. Similarly, the pressure difference from wind, ΔP_w, can be estimated by

$$\Delta P_w = \frac{\rho_{out}}{2} (C_{w,p} - C_{w,o}) U^2, \tag{2.7}$$

where $C_{w,p}$ and $C_{w,o}$ are the empirical, dimensionless pressure and internal pressure coefficients, respectively, and U is the average wind speed outside of the house. From these pressure differences, equation (2.5) can be used to estimate flow rate.

The first method examined by Walker and Wilson (1993) is to calculate separate flow rates using (2.5) and simply add them together. This method is highly inaccurate and practically never used, and was only added to the study for investigative purposes. The second approach, specified by the ASHRAE Handbook

of Fundamentals (1989), is to calculate flow rates separately and then add them in quadrature, such that

$$Q_{total} = (Q_s^2 + Q_w^2)^{1/2}, \tag{2.8}$$

where Q_s and Q_w are flowrates found using (2.7) and (2.8), respectively. When stack and wind effects are roughly equal, (2.8) has been shown to highly overestimate flow rates (Walker and Wilson 1993). An improvement for such a case is presented by Walker and Wilson (1993), dubbed the Alberta Infiltration Model (ALM-2), where

$$Q_{total} = \left[Q_s^{1/n} + Q_w^{1/n} + B_1(Q_s Q_w)^{1/2n}\right]^n. \tag{2.9}$$

The coefficients B_1 and n were found empirically to be approximately -0.33 and 2/3, respectively. The last technique examined by Walker and Wilson (1993) separates pressure and flow rate contributions from the laminar and turbulent aspects of the flow, dubbed the pressure additional method. This approach, presented by Etheridge (1977), uses an alternative approach for the relationship between pressure and flow rate. Instead of using (2.5), the pressure and flow rate can be related by

$$\Delta P = C_{lam} Q + C_{turb} Q^2 , \tag{2.10}$$

where $C_{w,p}$ and $C_{w,p}$ are empirical coefficients for laminar (units of $kg/m^4 \cdot s$) and turbulent (units of kg/m^7) contributions, respectively. This can be combined with (2.8) to calculate a total flow rate.

To test these four methods, Walker and Wilson (1993) performed tests in two different houses using the constant concentration tracer-gas dilution method. Results from these tests could then be compared to the results of the methods. Fan pressurization tests were used to find all empirical coefficients, as stated in the relevant papers. Comparisons of error in flow rate measurement with approximately 1,500 hours of testing data can be seen in Figure 7 for varying ratios of wind pressure to stack pressure. It can be seen that when these two pressures are close to equal, error is the highest, especially for the linear addition method. The three other methods can be seen to be drastic improvements upon the linear addition method, with the pressure addition method being the most accurate. These methods are likely to have more error than is reported, however. This is due to the fact that both the tracer-gas dilution method used in comparison and the blower door tests used to find empirical coefficients have large uncertainty associated with them, as shown by Sherman and Palmiter (1995) and Sandberg and Blomqvist (1985), stated above.

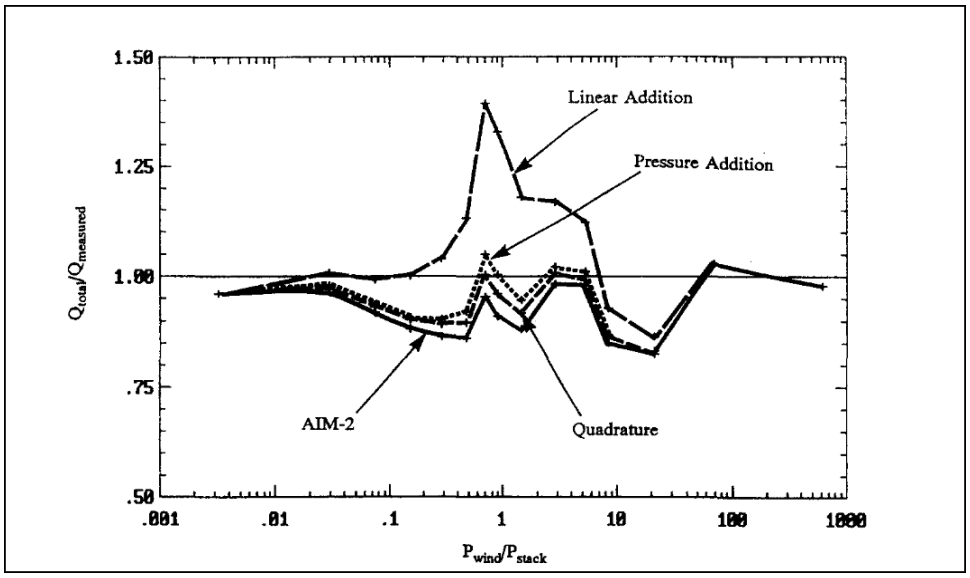

Figure 7. Error in superposition methods for estimating combination of stack and wind pressure effects on air infiltration vs. ratio of wind and stack pressures, presented by Walker and Wilson (1993). Error is defined as the analytical solutions for total flow rate divided by the flow rate found using tracer-gas dilution tests.

The detection of air, or more generally fluid, leakage is involved in a number of other industries besides building air infiltration. One of the most common cases which require leak detection is the storage of compressed gas. In gas storage units (e.g. compressed gas cylinders), aging, physical damage, corrosion, etc. can cause leaks in which the stored gas can escape. Depending on the gas in question and the leakage rate, this can potentially be quite dangerous. One of the most common methods for general leak detection of stored gasses is the use of ultrasonic leak detectors (McMaster 1982). While there are many types, ultrasonic leak detectors generally work by detecting acoustic disturbances created by gas flowing through a crack. In this method, the presence of acoustic signals above background static indicates the presence of a leak. While the strength of the

acoustic signal can be a form of judgment of leak strength, in practical purposes ultrasonic detectors only indicate or locate the presence of a leak, and do not measure leakage flow rates.

Ultrasonic leak detectors have been modified and improved to fit many specific cases, not just limited to the detection of leaks in compressed gas storage systems. For chemically active gases, surface acoustic wave (SAW) devices have been shown to be effective in detecting the presence of a leak (Fox and Alder 1989). The principle behind basic SAW methods is that the fluid barrier is coated in a material that is reactive to the gas being stored. If a leak exists, exiting gas will react with this coating. The SAW sensor itself sends acoustic waves through the fluid barrier material. The presence of a leak, and subsequently the chemical interaction between the gas and the coating, creates a phase shift in frequency of the acoustic signal, which indicates the presence of the leak (Fox and Alder 1989). This method works well, but only for very select cases. For instance, the standard SAW method does not work with inert gases and requires the envelope material to be coated, which may not be possible depending on the application.

Sheen et al. developed an alternative 'thermal SAW' method for use with inert gases, such as helium (Sheen et al. 2000). Instead of relying on chemical interactions to cause a shift in acoustic frequency, this SAW method uses the fact that the presence of helium at a leak site greatly changes the thermal conductivity from that of air. Heating can be applied to a potential leak area, and acoustic signals can be a measure of thermal conductivity via the resonance frequency of the

signaling device. A change in thermal conductivity from the presence of helium causes a change in resonance frequency of the acoustic sensor. This change therefore indicates a leak in helium. Leak sites can be detected by slowly moving the thermal SAW sensor until changes in resonance frequency are detected (Sheen et al. 2000), and a sample sweep of the thermal SAW device for two different leakage rates can be seen in Figure 8. This method has a number of drawbacks, however. For one, each individual sensor will have a unique resonance frequency and therefore repeatability of results between different sensors requires extensive calibration. Also, the range of leakage flow rates that can be detected is limited because only leaks of high flow rates generate enough helium to create a detectable difference in thermal conductivity. Leakage rates under 0.5 cm^3/min are indistinguishable from sensor noise (Sheen et al. 2000).

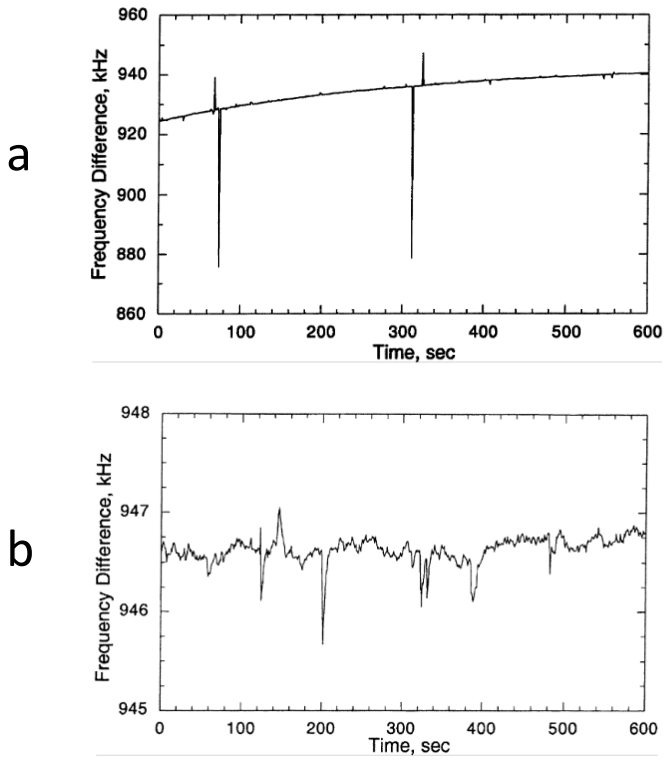

Figure 8. Sensor response to sweep over potential leakage sites for leakage rates of (a) 6 cm^3/min and (b) 0.5 cm^3/min. Spikes in resonance frequency equate to the presence of a helium leak (Sheen et al. 2000).

For accurate detection of leakages under 0.5 cm^3/min, Sheen et al. (2000) proposed a different acoustic technique for helium detection. Instead of using a change in thermal conductivity, a change in the local speed of sound of a gas mixture is the identifier for a helium leak. The sensor works by sampling gas in a potential leakage area. This gas is sucked into a testing chamber, where acoustic signals are sent through. The time of flight (TOF) of the signal across the test chamber is compared to the TOF in ambient air. Any difference indicates a change in local speed of sound and hence a helium leak. This method was tested with

varying controlled leakage flow rates, and results can be seen in Figure 9. This method was found to be an improvement upon thermal SAW testing for lower leakage flow rates (Sheen et al. 2000). However, it still shares drawbacks associated with many forms of ultrasonic leak detection as well as some of its own. While this works great for helium, the method requires the gas under question to have a speed of sound greatly different than air, drastically minimizing the cases in which this technique is effective.

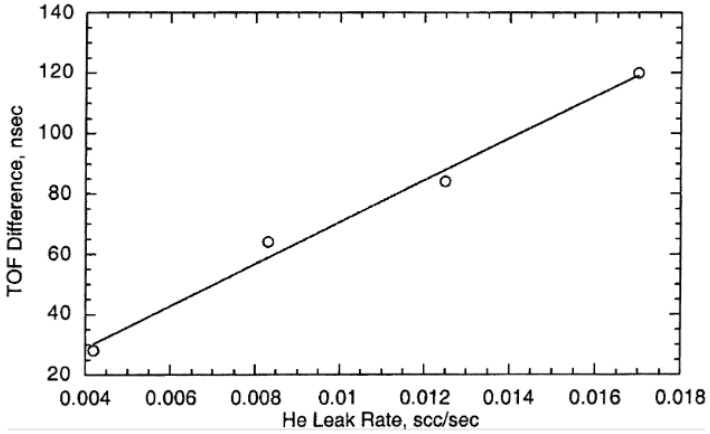

Figure 9. Time of flight differences vs. controlled helim leakage rate for sampling using the speed of sound ultrasonic leak detection method (Sheen et al. 2000).

Ultrasonic leak detectors are also extensively used in the space industry. Air leakage into space is of paramount concern to manned space missions, where loss of oxygen could lead to fires or loss of astronaut life support. Generally, astronauts are given simple, hand-held devices which detect acoustic disturbances. These devices, however, are flawed in numerous ways. Besides being relatively heavy (where kilograms of matter transported into space can cost hundreds of thousands

of dollars each), Strei et al. (2003) has shown that the signals picked up by these detection methods can be severely degraded by multi-modal elastic wave dispersion. When triangulation techniques are used with ultrasonic sensor arrays, this can lead to false leak site identification by the equipment. In order to remedy this problem, Strei et al. (2000) proposed a method using Fourier transforms to analyze cross correlation data between sensors in an array. These arrays are placed on the spacecraft hull, generally in groups of 16x16 sensors. The use of this cross correlation data was found to successfully eliminate differences in signals between sensors caused by the multi-modal nature of acoustic signals generated by leaks.

There have been additional methods which employ a similar triangulation approach to detect leakage locations while minimizing the number of required sensors. Holland et al. (2007) examined a number of array configurations which use cross correlation analysis similar to that proposed by Strei et al. (2000). Testing of these methods was performed on an aluminum plate with a small hole that is attached to a vacuum source. Sensor configurations included coupled and de-coupled two-dimensional phased arrays, a distributed discrete sensor array, and a rotating two-sensor method. The coupled and decoupled phased arrays are two sensor arrays consisting of 16x16 sensors, where the latter requires less cross-correlation calculations and thus detects leaks much more rapidly. The discrete sensor array has individual sensors, as opposed to arrays of sensors, located throughout the hull material and thus overall uses fewer sensors than the phased array. The two-sensor method uses two sensors which rotate in increments of 15º,

drastically reducing the amount of sensors required. However, the two-sensor method is more restricted in its uses, and requires access by astronauts to move the sensors (Holland et al. 2007). Examples of leakage locations found using these techniques can be seen in Figure 10.

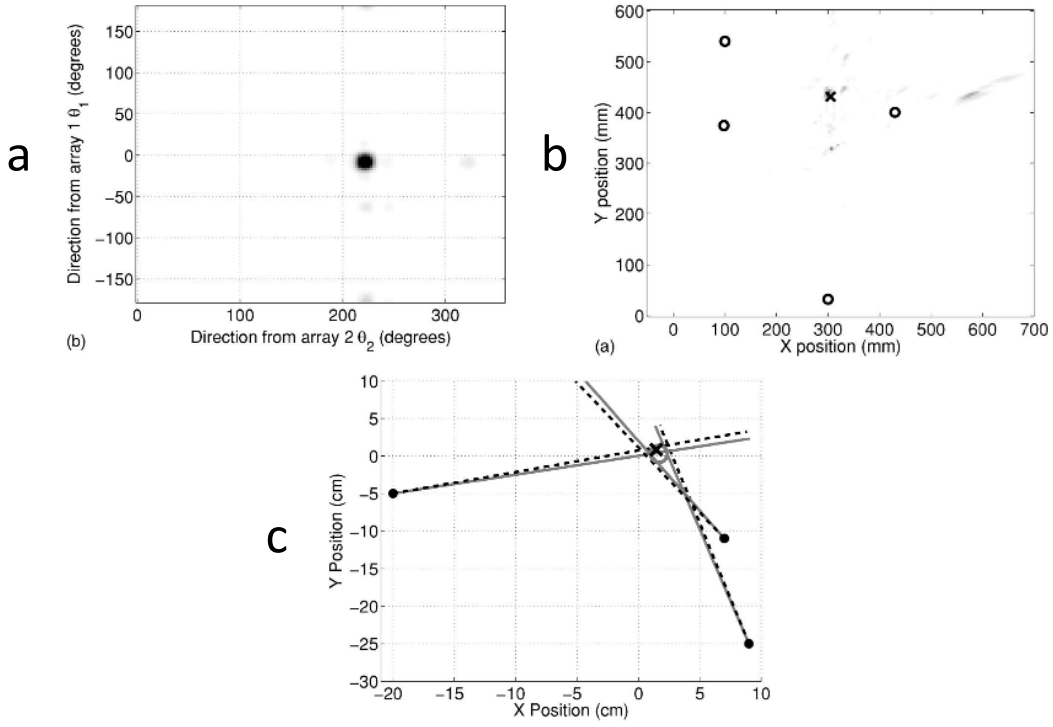

Figure 10. Example leak location detection using (a) phased arrays, (b) discrete sensors, and (c) rotating two-sensor method as presented by Holland et al. (2007).

All of the above methods for leak detection in hulls have faults relating to the scope of the detection. For one, they all require an array of sensors, sometimes in the hundreds, which can be costly and burdensome to the material under testing. Most critically, all of these acoustic methods require a existence of a hull of uniform composition and geometry in order for the acoustic processing techniques

to work. This method becomes useless for all but the simplest of geometries and materials. Liao et al. (2013) tried to use the accuracy of triangulation methods in a more versatile package. The proposed method is a portable, three sensor ultrasonic leak detector in an equilateral triangle configuration. Triangulation is performed by analyzing the time delays between the signals received by the three sensors. A schematic diagram of the sensing technique can be seen in Figure 11. The accuracy of the proposed time delay estimation ultrasonic leak detector (TDEULD) was compared to that of the industrial standard leak detection (known as the directivity-based ultrasonic leak detector, DULD). Testing was performed with a know leak location where both methods measured angle and distance to the leak from the sensor location. Error for the TDEULD method was found to be 6.5-8.3 times lower than that of the standard DULD method (Liao et al. 2013), and error results can be seen in Figure 12.

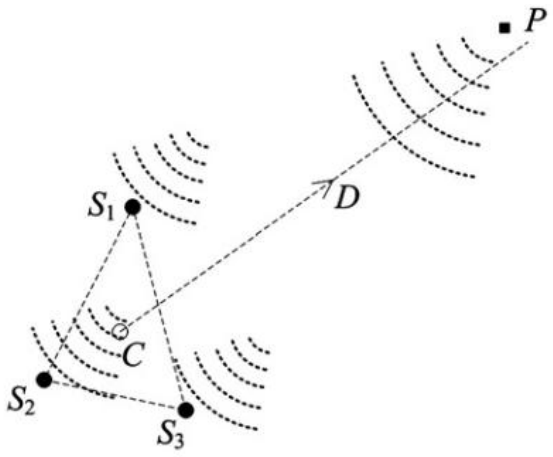

Figure 11. Schematic diagram of the TDEULD portable leak detection method (Liao et al. 2013).

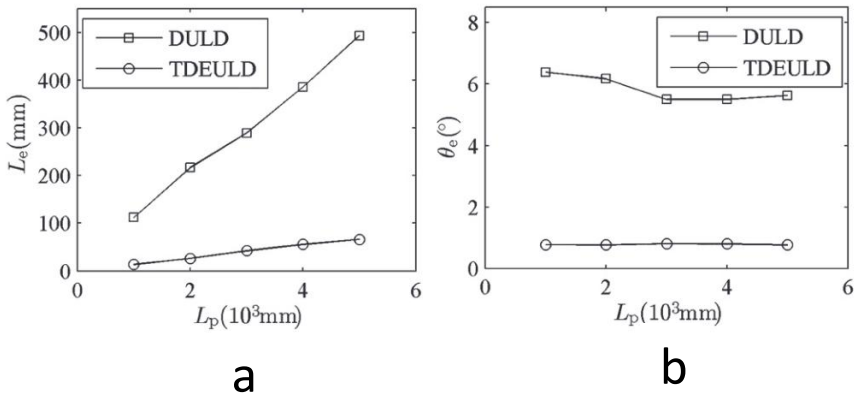

Figure 12. Experimental root-mean-squared error of the DULD and TDEULD methods for (a) distance to leak and (b) angle to leak as a function of leakage area, as presented by Liao et al. (2013).

Many other leak detection methods exist for more specific applications. For the detection of gas leaks other than air, mass spectrometry is often a popular method for the detection of such a gas within near-by air. These methods work by sampling and ionizing gas mixtures and identifying the ions present in the sample via separation. Basic mass spectrometry detectors can act as a first response alarm; notifying the user that there is a presence of the stored gas in the atmosphere around it. Hodgkinson et al. (2006) examined using mass spectrometry to detect and locate natural gas leaks from pipelines that seep up into the atmosphere through the ground. An experimental reproduction of a leak site was created in a large wind tunnel to simulate natural gas seeped out from the ground by a leak in an underground pipeline. Due to wind and atmospheric effects, plumes of natural gas leaking in this manner can be hard to track to the source via sensors. An example of such a plume can be seen in Figure 13. Using a Gaussian model for gas plume transport, techniques and parameters for optimal leak detection were examined.

Results using simple, single sensor methods were found to be extremely ineffective due to such atmospheric effects.

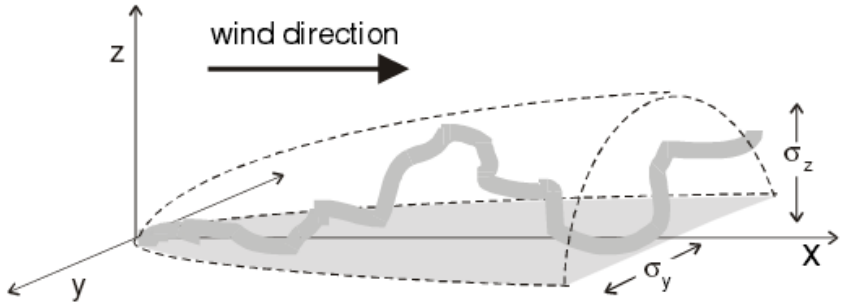

Figure 13. Schematic representation of a natural gas plume meandering in a volume defined by a Gaussian distribution (Hodgkinson et al. 2006).

Vacuum systems and equipment often have very high standards for residual leakage, and the presence of a leak could be damaging to system use. As such, many methods for detecting leaks in vacuum systems have been developed. For vacuum furnaces in the nuclear industry, Ahmed et al. (2012) has proposed an in-service method of leak detection using helium mass spectrometry. This method works by connecting the vacuum system to a contained helium mass spectrometer, as seen in Figure 14. The system is put under vacuum, and then areas of suspected leaking are sprayed with helium. If there are indeed leaks, the helium will travel inside the vacuum equipment and be detected via the mass spectrometer. Suspected leak sites can therefore be tested one at a time for the presence of leaks. However, difficulties can arise when testing multiple leakage sites in a row as the interior of the equipment can become over-contaminated with helium.

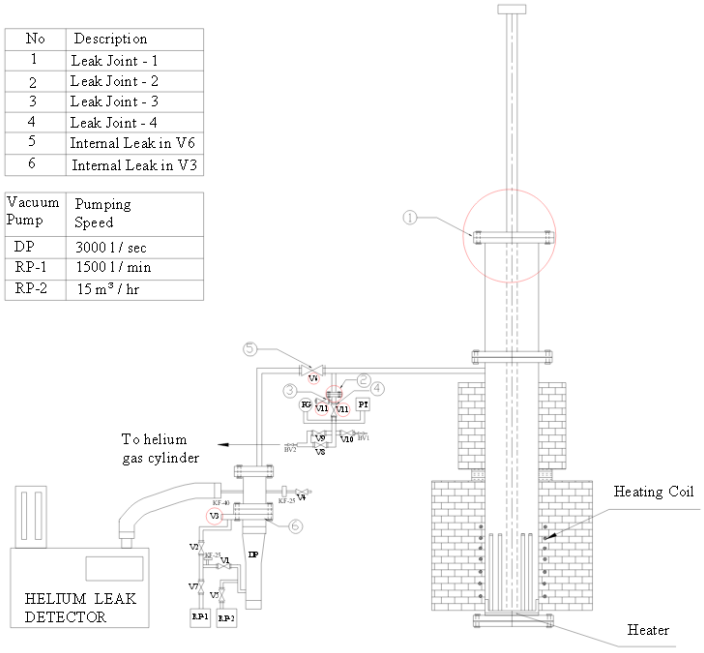

Figure 14. Sample vacuum furnace and helium leak detector schematic presented by Ahmed et al. (2012).

Another use of mass spectrometry is for detection of leaks in refrigeration systems. Morgado et al. (2010) proposed a standard method for testing entire refrigeration equipment systems. As opposed to the method used by Ahmed et al. (2013), this testing method places the entire refrigeration system under investigation in an enclosed chamber at atmospheric pressure. Refrigerant leakage into the testing chamber is measured via mass spectrometry, from which the total leakage rate over the testing period can be deduced. A schematic of this method can be seen in Figure 15. Uncertainty analyses were performed on the results from these tests, and it was found that the expanded uncertainty for leakage measurement was approximately 5% (with a 95% confidence level) (Morgado et al. 2010).

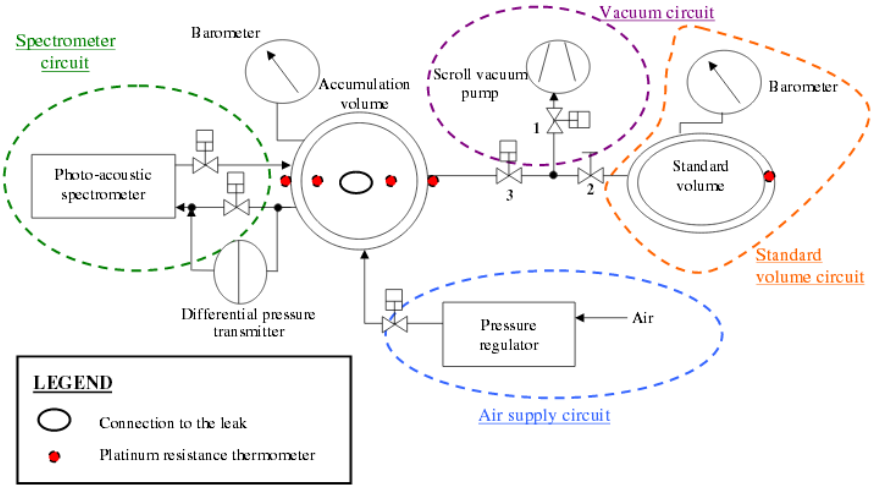

Figure 15. Schematic of the spectrometry method used to test for refrigerant leaks, as presented by Morgado et al. (2010).

An alternative to mass spectrometry for leakage detection in vacuum piping is the use of an orifice flow meter. A dual-orifice plate flow meter was proposed by Masqood et al. (2013) to measure flow rates passing through orifices. The principle behind the measurement was based upon the pressure difference between the upstream and downstream sides of the flow meter and calibration of the orifices. Testing of this device found flow rates to be linearly related to pressure difference. Two orifice (leak) sizes of 110µm (O_a) and 130µm (O_b) were tested, as seen in Figure 16. This method is very limiting in the leak testing cases, as it requires the part under consideration to be able to be fit without leaks to the testing apparatus as well as only measure leaks of relatively high flow rates of $Q = 0.0015\,\mathrm{m}^3/\mathrm{s}$ or greater.

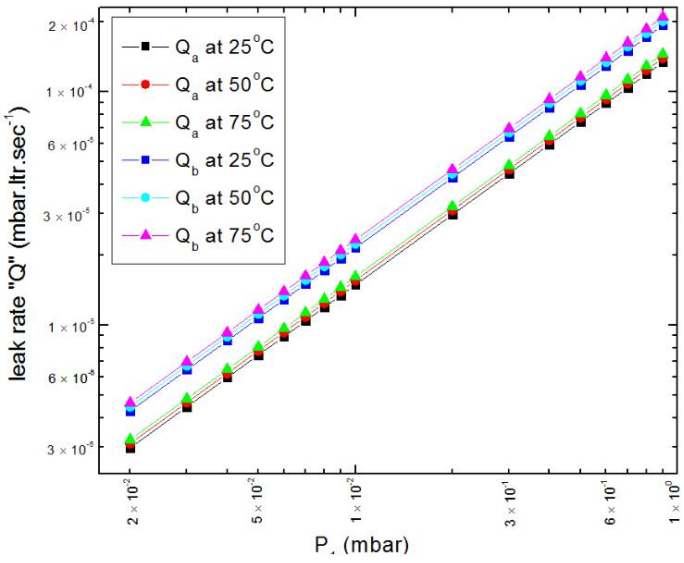

Figure 16. Flow rate vs. upstream pressure (P_1) for the two tested orifices in the study conducted by Maqsood et al. (2013).

There are a few other, much less common methods for detecting leaks. One class of such methods includes infrared, or optical fiber absorption detection, which can detect the presence of gases other than air through changes in optical properties of the gas mixture (Bévenot et al. 2000). Similarly to ultrasonic methods, optical methods are often only useful for the purposes of identifying leak areas, and not measuring leakage flow rates themselves. Overall, the standard leak detection systems currently in use either detect leakage locations, measure flow rates for entire systems, or are highly restrictive in their use. There is a need for a simple, accurate method that can provide both leak detection and flow rate characterization for local regions of a system.

2.2. Particle Infiltration through Cracks

While the transport of fluids through small channels, such as cracks or leaks, can have detrimental effects on building energy usage, the particles carried with the air flow can similarly have detrimental effects on air quality within the building or structure. Determination of the rate of particle passage into a structure is complicated by the fact that several different physical phenomena can lead to entrapment of some of the particles during transport through a crack. These mechanisms include gravitational settling, Brownian diffusion, and inertial trajectories that cause collisions between the particles and the crack channel walls. The capture of particles during infiltration through a crack is typically quantified by a penetration factor, which is equal to the ratio of the number of particles that travel through a crack to the number of particles entering a crack. This section will review previous work on particle infiltration through small passages, including analytical, experimental, and numerical studies.

Understanding of significance of particle capture during transport through a crack first developed during experiments on indoor versus outdoor levels of dust and other pollutants in the work by Alzona et al. (1979). Previously, the consensus was that building envelopes provided no protection from atmospheric contaminants, i.e. given time to equilibrate, levels of particles inside a building would be the same as that outside. The basis behind this thought was that concentrations of dust in air can be modeled as concentrations of non-reactive gases, which will always equilibrate with enough time (Slade 1968). The study by Alzona et al. (1979)

critically examined this hypothesis. Experiments were performed in numerous rooms of different buildings, as well as two different types of automobiles. Tests were performed by 'cleaning' all of the inside air before data collection, which was done using a large suction device to run the air through a fine filter until dust levels were negligible. After cleaning, periodic samples of the air were taken. This involved using suction to run some air through a clean filter. The dust trapped on the filter was examined via X-rays to identify dust species. Five different elements were examined, which represented common components of five major sources of pollution. These include lead, bromine, iron, zinc, and calcium.

Similarly, air and dust samples were taken of atmospheric air to find concentration levels for the same five elements. The penetration of particles into the building or automobile envelope was denoted by the ratio of indoor to outdoor quantities of these five elements, shortened to I/O (Alzona et al. 1979). After numerous studies, even after equilibrium indoor concentrations had been reached, for all elements examined I/O was less than unity; disproving the previous hypothesis of those such as Slade (1969). A sample test run can be seen in Figure 17. Alzona et al. (1979) found that, on average, I/O for all species were around 0.3; however, values from day to day changed drastically. This indicated that there are physics which affect particle infiltration; however, such causes were not investigated in the study.

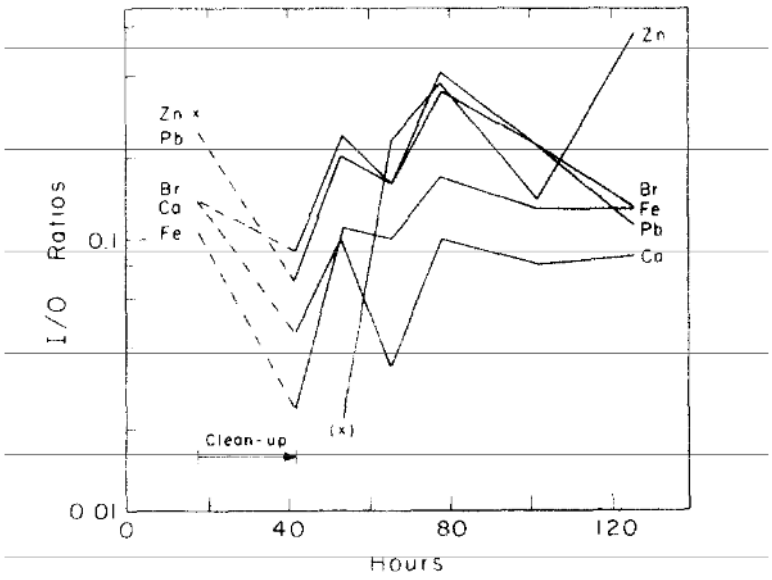

Figure 17. Ratios of indoor to outdoor concentrations for five elements found in an example trial by Alzona et al. (1979).

With the understanding that penetration factors with values less than unity can exist, even after equilibrium concentrations have been reached, many other experimental studies were performed to investigate penetration factors and indoor contaminant concentrations. One such study was performed by Dockery and Spengler (1981), in which indoor contaminant levels were examined from both indoor and outdoor sources. Experiments measuring total indoor contaminant particle concentrations in 68 homes across six different cities were performed. Measurements were taken over 24 hour periods every 6 days over the course of a year. A model for mean contaminant concentration, $\overline{C}_{ind}$, was derived based upon a mass balance approach for both particles of indoor and outdoor origin. This

approach equated the concentration to factors of particle penetration through building envelopes and indoor particle generation, where

$$\overline{C}_{ind} \approx \overline{P}\overline{C}_{out} + \frac{\overline{S}_{ind}}{Q_{tot}}. \tag{2.11}$$

In this model, $\overline{P}$ is the mean particle penetration factor for the house, $\overline{C}_{out}$ is the mean concentration of particles in the local atmospheric air, $\overline{S}_{ind}$ is the mean indoor generation of particles (units of μg/hr), and Q_{tot} is the total flow rate of air out of the house (Dockery and Spengler 1981). $\overline{P}$ and $\overline{S}_{ind}$ represent empirical terms to be found using testing approaches similar to that of Alzona et al. (1979).

The purpose of the study was to examine the effectiveness of the model given by (2.11) as well as how a few environmental factors affect mean particle concentrations. A comparison of concentration values from testing data and that given by (2.11) can be seen in Figure 18. It can be seen that the general profile of data suggests a good correlation; however, discrepancies were significant at times. Factors affecting particle penetration included the presence of central air-conditioning, storm windows, kitchen ventilation, and the type of home heating. Factors affecting indoor particle generation included the presence of cigarette smokers, the heating and cooking fuels used, and the presence of air-conditioning. It was found that, for outdoor particle penetration, the presence of full center air-conditioning was the contributing factor to mean penetration factor (Dockery and

Spengler 1981). For houses without air-conditioning, average indoor particle concentrations were around 70% of that of outdoor concentrations. With central-air, the average value was approximately 30% of outdoor concentrations.

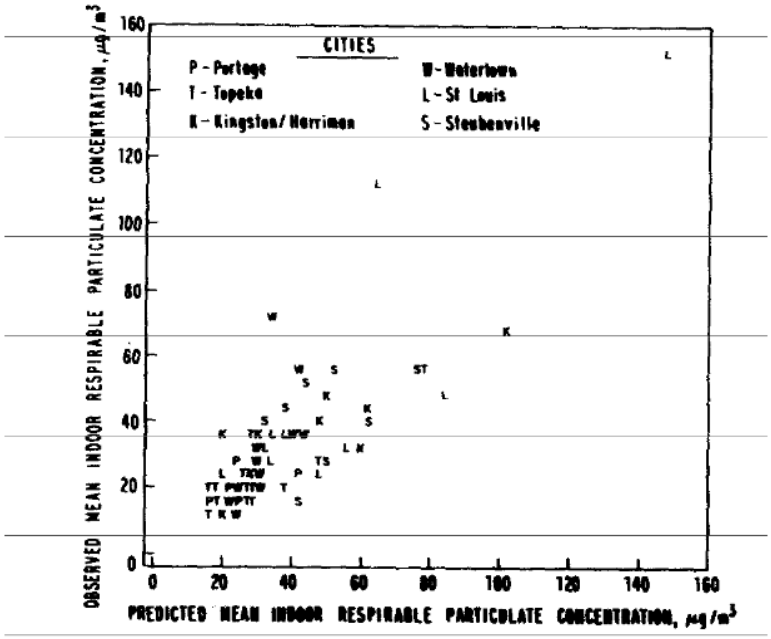

Figure 18. Experimental mean indoor particle concentrations vs. predicted concentrations given by (2.11) for the six cities under investigation by Dockery and Spengler (1981).

Another similar study was performed by Thatcher and Layton (1995) which investigated total particle concentration fluctuations in air due to different effects, including outdoor particle penetration and resuspention of indoor particles, such as settling of particles on surfaces within the building. Studies were performed in a single, two-story home during the summer months in Southern California. Particle concentration measurements were calculated using a 'sampling tube,' for which air could be purged/taken in for testing purposes. Indoor and outdoor sampling tubes

were placed at average adult breathing heights. Particle concentrations were measured using an optical particle tracking technique. Penetration factors stated by Thatcher and Layton (1995) were of unity or higher; however, the methodology used to calculate 'penetration factors' included particles generated by internal sources, such as a person entering a room and bringing in particles with them. In this sense the 'penetration factor' as stated by Thatcher and Layton is not an actual penetration factor in the normal sense. After subtracting out the particle deposition due to internal sources, penetration factors in the Thatcher and Layton study were found to be in the range of 0.2 to 0.6. Studies into adjusted particle infiltration with five different ranges of particle diameter can be seen in Figure 19.

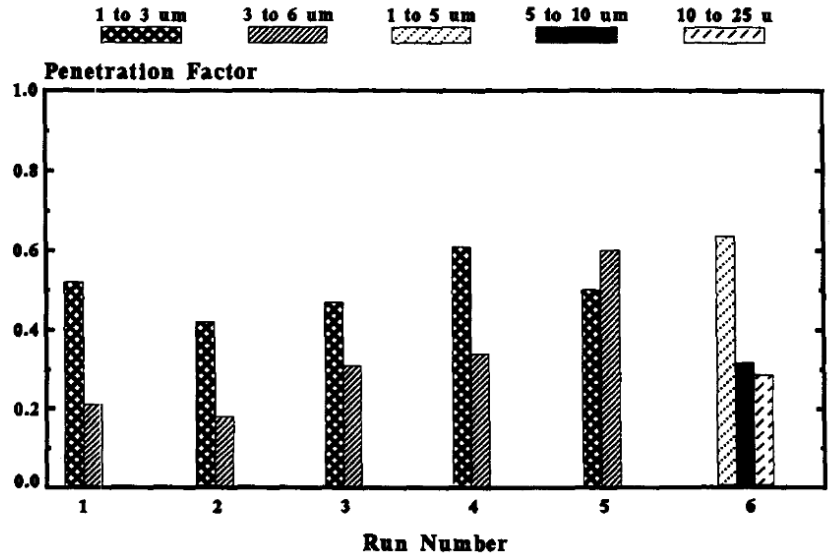

Figure 19. Penetration factors for several test runs and ranges of particle diameters reported by Thatcher and Layton (1995).

A fourth experimental study into total building particle concentration was performed by Tung et al. (1999). This study was performed in an office building in Hong Kong, where outdoor air pollution is a very serious problem. The study consisted of measurements taken at night over a period of approximately one month. Tests were performed at night when there were no occupants of the office and the air conditioning was turned off such that internal sources of particulate matter were minimized. Portable, real-time aerosol monitors, which used a light scattering technique to actively track particles, were used to measure indoor and outdoor particle concentrations. To include indoor particle concentration decay due to gravitational settling and ventilation, a modified equation for penetration factor P was used (Tung et al. 1999) where

$$P = \frac{\lambda C_{ind}}{(ACH)_{eff} C_{out}}. \tag{2.12}$$

In this equation, λ is the indoor dust decay parameter (units of 1/min), an empirical coefficient relating to the rate of indoor particle removal via settling and diffusion, and $(ACH)_{eff}$ is an empirically found coefficient for the effective air change rate out of the building. Tung et al. (1999) found penetration factors in the range of 0.69-0.86 for the duration of their testing.

While there are many experimental studies into total building particle penetration, they all have a few things in common. Most notably is that penetration

factors found through various studies can range extensively, even when building sites under survey are relatively similar. This is an indication that there are physical mechanisms involved which dictate the penetration factor. Experiments such as the one reported above are done for entire building concentration levels, and as a consequence the degree to which such studies can address fundamental issues associated with particle filtration during infiltration through individual cracks and gaps is limited. In light of this, several studies have been performed in order to better understand the principles of particle infiltration through individual gap sites.

An analytical investigation of air leakage rates through gaps in doors was performed by Gross (1991). This study was performed to estimate smoke infiltration through barriers such as doors, windows, etc. in the event of a building fire. The study included flow through straight, rectangular gaps as well as those with bends or obstructions. As internal flow of air and smoke during a building fire is induced by pressure gradients between burning and non-burning zones, flow rates through gaps were found as a function of pressure difference and gap thickness (Gross 1991). An example of tabulated curves for volumetric flow rate through a straight channel can be seen in Figure 20. While this yields values of fluid flow rate, it does not take into account filtration effects that smoke particles experience while traveling through narrow passages and therefore highly overestimates the concentration of smoke particles at the exit of the gap in question.

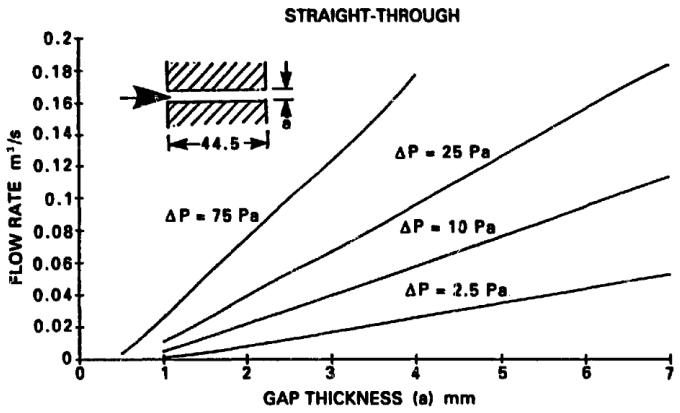

Figure 20. Fluid flow rate as a function of gap thickness and pressure difference for straight gaps reported by Gross (1991).

The study by Gross (1991) is effectively missing the inclusion of the particle penetration factor. More thorough investigations of particle transport through gaps have been performed which include and try to examine penetration factor. One such examination was performed by Liu and Nazaroff (2001). An analytical approach was used to generate models for penetration factor of cracks in building envelopes. The cracks were assumed to be rectangular channels, some straight and some with any number of 90º bends. To examine the causes of particle impaction in cracks, penetration factor was separated into three main sources: gravitational settling, diffusion due to Brownian motion, and impaction due to bends in the crack. Individual penetration factors from these three sources were solved for separately, and then it was assumed that the multiplication of each separate penetration factor would yield the total penetration factor (Liu and Nazaroff 2001). All three of the equations for individual penetration factors were based upon the assumption that

particle concentration distribution at the crack inlet is fully developed and the same as that for air outside of the crack.

The expression for penetration factor due to gravitational settling, P_G, used by Liu and Nazaroff (2001) was derived by Fuchs (1964), stating

$$P_G = 1 - \frac{v_G L}{HU}, \tag{2.13}$$

where v_g is the settling velocity, L is the length of the channel, H is the height of the channel, and U is the average fluid velocity in the channel. The expression for penetration due to Brownian diffusion, P_B, was empirically derived by De Marcus and Thomson (1952) using mass conservation and advection of particles due to Brownian motion, where

$$P_B = 0.915\exp(-1.885\phi) + 0.0592\exp(-22.3\phi) + 0.026\exp(152\phi) + \ldots \tag{2.14}$$

In this equation, ϕ is defined as

$$\phi = \frac{4BL}{H^2 U}, \tag{2.15}$$

where B represents the Brownian diffusion coefficient. Finally, the expression for impaction penetration factor due to bends in the crack, P_I, was examined based upon results from rectangular impactor nozzles (Marple and Willeke 1976). However, this term was disregarded as the vast majority of particles subject to impaction on bends were assumed to be affected by gravitational settling first (Liu and Nazaroff 2001). Multiplication of P_G and P_B was tabulated by Liu and Nazaroff (2001) for multiple particle diameters, crack diameters, and pressure differences across the crack and can be seen in Figure 21.

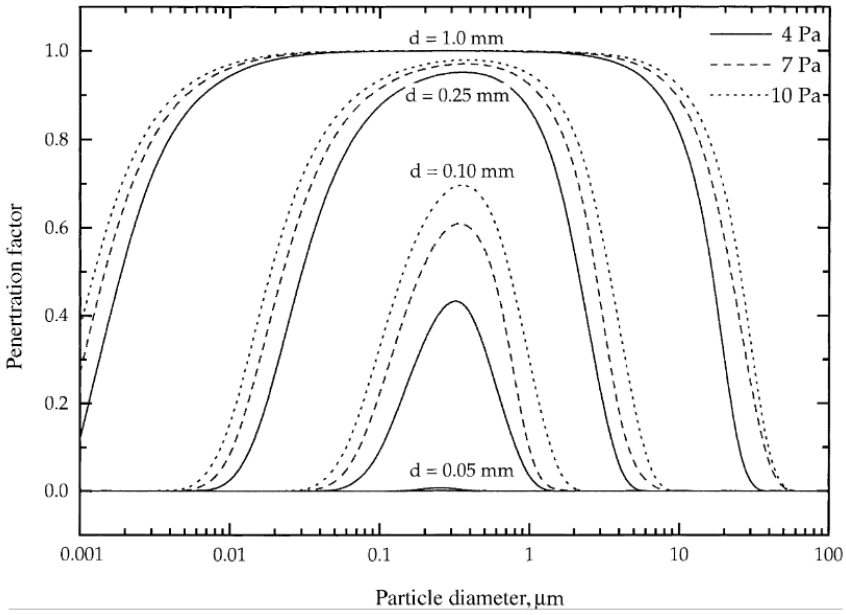

Figure 21. Particle penetration factor as a function of particle diameter, channel height, and pressure difference for a channel length of 3cm using the assumption of the multiplication of Settling and Diffusive penetration factors (Liu and Nazaroff 2001).

This study omits particle capture due to entrance effects, assuming that these effects are small. Additionally, it does not account for entrance particle

concentration deviations for a normal distribution due to said entrance effects. A computational approach was used by Chen and Korjack (1980) to study the effects of the entrance region on particle capture in a vertical channel, with the computational domain restricted to the inside of the channel. The governing equations for fluid motion were solved using a finite difference method, and particle capture due to gravitational settling and Brownian diffusion were solved with a modified diffusion equation to account for both effects. The primary goal of this study was to examine the effect of flow profile development in the entrance region on particle capture. However, because the computational domain did not include the inlet reservoir upstream of the crack channel, the lateral particle inertia that is developed as particles are driven into the channel is not included in the study by Chen and Korjack (1980). This exclusion means that the study is lacking some fundamental physics behind entrance region flow being funneled into a crack.

An experimental study into various physical causes of penetration factor was performed by Mosley et al. (2001). A carefully constructed experiment for particles of varying size traveling through a narrow, rectangular slot was used. This experiment consisted of two large square reservoir chambers separated by a narrow, horizontal, and rectangular channel of dimensions 0.5x122mm. A pressure difference was created between the two reservoir channels to create flow through the gap. The chamber with higher pressure represents the ‘outside’ of a building, while the second chamber is the ‘inside.’ Mixing fans were present in both chambers to ensure relatively even particle distributions in the air. For a test,

particles were injected into the first chamber and the gap closed until an even concentration of particles was reached. Then, the gap was opened and a pressure difference held to create flow between the two chambers. Particle concentrations in both chambers were measured using two instruments and techniques. The first was an aerodynamic particle sizer (APS), which uses a Venturi arrangement to sort particles by size and identify particle concentrations. The second technique was an electrical low pressure impactor (ELPI), which measured particle size and concentration by bombarding the particles with electrons and measuring charge collected on cascade impactor stages.

To calculate penetration factor from a difference in particle concentration percentages between the two chambers, Mosley et al. (2001) developed a model for which empirical data could be used to generate penetration factor. The model states that

$$\frac{C_{in}}{C_{out}} \approx \frac{PQ}{V} t . \tag{2.16}$$

Values of volumetric flow rate Q and total volume V were fixed and known, so linear regression could be performed on experimental data to find the value of $\frac{PQ}{V}$, and consequently calculate P (dimensionless). An analytical model was also used to compare to data taken from laboratory testing. This model assumed that the only mechanisms of particle capture during transport through the gap were from

gravitational settling and Brownian diffusion. Similar to Liu and Nazaroff (2001), it was assumed that these two mechanisms were independent, such that their penetration factors could be multiplied to find total penetration factor P. Mosley et al. (2001) used the same expression for gravitational penetration factor used by Liu and Nazaroff (2001), which was originally derived by Fuchs (1964) given in equation (2.13). However, a different equation for diffusive penetration factor was used by Mosley et al. (2001); originally derived by Lee and Gieseke (1980) to be

$$P_B = \exp\left(-\frac{7.868\,D_b L}{H^2 U}\right), \tag{2.17}$$

where D_b is the Brownian diffusion coefficient $D_b = k_B T / 3\pi\mu d$. This equation was found by Mosley et al. (2001) to yield similar results as the empirical equation given by (2.14); hence analytical results presented by Mosley et al. (2001) are practically identical to those given by Liu and Nazaroff (2001).

During the experimental trials, pressure difference and particle diameter were varied. For each data pair ($\Delta P, D$), 7-12 trials were run to ensure statistical accuracy. An example trial, showcasing data collected with the APS, ELPI, and analytical techniques can be seen in Figure 22. While the model fits reasonably well for particle diameters <2μm, for larger particle sizes the analytical model drastically overestimates penetration factor. This suggests that the current model is missing a mechanism or mechanisms for particle capture, especially at higher particle

diameters. Such a cause could be inertial impaction in the entrance region due to high particle inertia, which would be the case for particles of larger diameters.

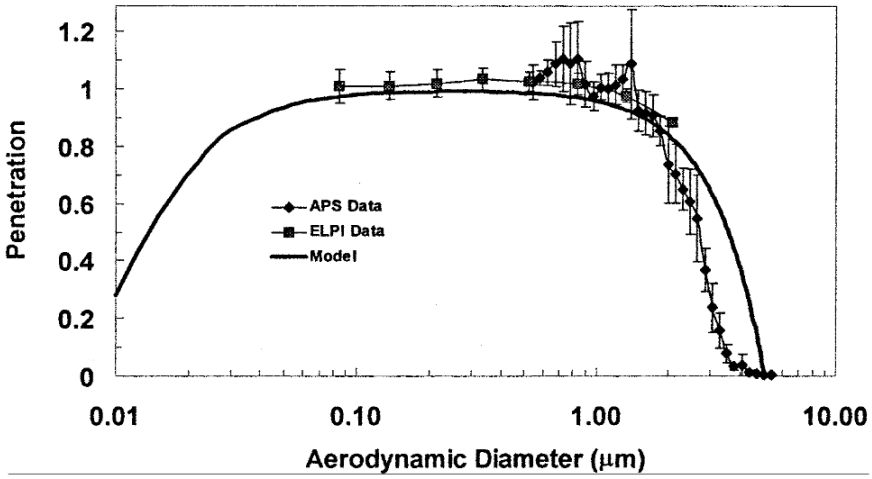

Figure 22. Comparison of penetration factors from experimental measurements and the analytical model for a pressure difference of 10 Pa, as reported by Mosley et al. (2001).

CHAPTER 3: LOCAL AIR LEAKAGE DETECTION AND MEASUREMENT

Chapter 3 of this thesis is dedicated to the presentation of a new, local tracer gas technique for measurement of air leakage flow rates. Current methods of leakage detection, especially for building envelopes, only test entire building leakage with high levels of uncertainty. These techniques have no ability to measure leakage rates of individual fixtures, in which the knowledge of leakage rate could lead to the decision to replace said fixture. The method proposed in Chapter 3 would allow the testing of leakage flow rates for individual, suspected leakage sites, such as a window, in such a manner that does not disturb normal use of the building. In this chapter the design, data reduction, uncertainty, and validation via comparison with numerical simulations and empirical correlations will be overviewed. Concluding remarks regarding the successful laboratory testing of this method are given in Chapter 5.

3.1. Experimental Method

3.1.1. Design Considerations

The design of a method for local air leakage detection and characterization was developed which uses a tracer-gas approach, thereby allowing the determination of the air leakage rate using only pressure and concentration sensor measurements, and avoiding issues with accuracy of mass flow meters at very low flow rates. CO_2 was selected as a tracer gas because it is inexpensive and readily

available, but also only present in low concentrations in the ambient atmosphere. Two design concepts were considered, both of which require access to only one side of the structure (i.e., either the inside or the outside of the wall) and involve only local testing, rather than pressure reduction within the entire structure.

The first design concept, shown in Figure 23a, maintains a constant vacuum pressure within a chamber placed against the wall location where a leak is suspected. Appropriate sealing and support is used so as to eliminate leakage at the seals between this chamber and the wall. The pressure within this chamber is maintained constant, even in the presence of a leakage air flow into the chamber, by bleeding air into a second chamber through a pressure regulator valve. The second chamber is maintained at a lower vacuum pressure than the first chamber with use of a vacuum pump attached to the second chamber. Experiments are conducted by first evacuating both chambers to a set pressure, then adding CO_2 to both chambers to achieve a specified CO_2 concentration. The valve connecting the two chambers is then closed and the second chamber is further evacuated to a (lower) second vacuum pressure setting. Finally, the pressure regulator valve is activated, so that gas is allowed to pass from the first chamber to the second so as to maintain a specified vacuum pressure in the first chamber. By continually mixing the gas mixture within the first, measurement chamber to maintain uniform gas composition and monitoring the rate of change of the CO_2 concentration in the first chamber, the leakage air flow rate of atmospheric air into the first chamber can be determined.

The second design concept, shown in Figure 23b, uses only a single constant-volume chamber, to which a vacuum pump is attached. Both a pressure sensor and a CO_2 concentration sensor are placed within the chamber, and the chamber is placed against the wall as discussed in the previous paragraph. This chamber is initially evacuated to a specified vacuum pressure, after which the valve to the vacuum pump is closed. CO_2 is then injected into the chamber to a set concentration, and the gas within the chamber is maintained in a mixed state by two small fans placed inside the chamber. The pressure and CO_2 concentration are monitored in time, from which the leakage rate can be determined.

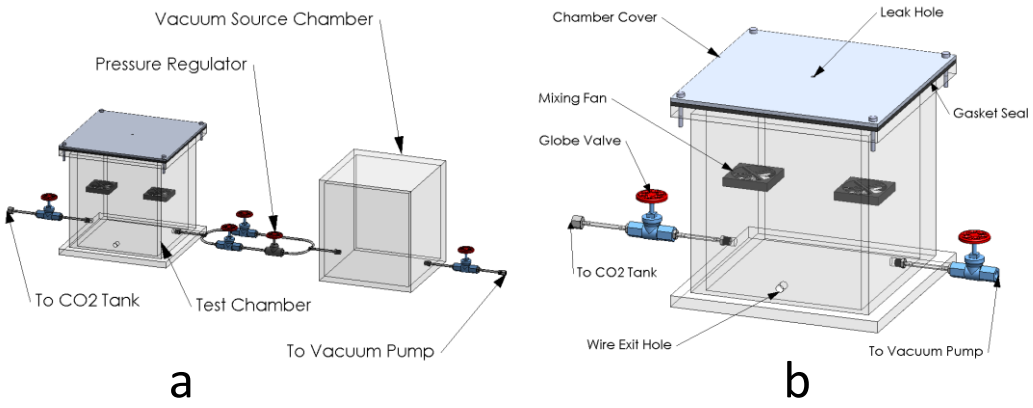

Figure 23. Schematic diagrams of (a) constant-pressure and (b) constant-volume design concepts used for the laboratory experiments.

Both of the above designs have been implemented in laboratory tests. The first design concept was the primary approach initially due to the fact that it allows the determination of leakage rate with constant values of the pressure difference, whereas in the second design the pressure difference varies throughout the experiment. However, after conducting experiments with both approaches, it is

evident that the second design has numerous advantages compared to the first design. In particular, the pressure regulator valve used in the first design only allows gas flow between the two chambers when the difference between the first chamber pressure and the set pressure has exceeded a critical value. This fact introduces significant noise and uncertainty in the leakage rate measurements. The second design is also considerably less expensive and less cumbersome than the first, because it requires a single chamber and no pressure regulator valve. To enable sufficiently long test durations in the first design, the second chamber would have to have a significantly greater volume than the first chamber, making the system unnecessarily large and bulky. Even the fact that the pressure varies with time in the second design turned out to be an advantage, because leakage rates for a wide range of pressure difference values could be determined in a single test, provided that the leakage flow rate is sufficiently slow compared to the time scale required to obtain uniform mixing within the chamber. For these reasons, all data reported in the thesis are for the second (constant-volume) design concept.

3.1.2. Experimental Apparatus and Method

Laboratory experiments were performed to examine the accuracy of the leak detection design concept. The test chamber used in these experiments is made from 13 mm thick acrylic plastic (Plexiglas) and has a volume $V_t = 0.028 \pm 0.0002\ \mathrm{m}^3$. The top of the test chamber has a removable cover, in the center of which is a 0.89±0.01 mm diameter hole that represents the leak to be tested. A section of

rubber sheet is used to block this hole when desired. The top cover is placed on a large gasket to prevent side leaks and secured onto the test chamber using eight screws. Leak testing was performed to ensure that residual air leakage of the test chamber was negligible, which is detailed in Section 3.3.3. Inside of the test chamber are a non-dispersive infrared (NDIR) CO_2 sensor (CO2Meter.com, COZIR Ultra Low Power Carbon Dioxide Sensor GC-0005-DEV) and two mixing fans. The mixing fans are used to ensure that the CO_2 level remains nearly uniform throughout the chamber. There is also a small exit hole for the wires of the mixing fans and the CO_2 sensor, which is sealed using a rubber stopper and silicone sealant to ensure stable vacuum conditions during testing.

The test chamber has both inlet and outlet lines. The inlet is connected via flexible tubing to a CO_2 tank, which is used to supply the tracer gas. The inlet gas can be controlled using a globe valve in the inlet line. The outlet leads from the test section to a digital pressure transducer (Omega Engineering, Brass Pressure Transducer PX182B-015VACI), which is used to monitor the pressure level inside of the test chamber. Downstream of the pressure sensor, the outlet line connects to a globe valve and a vacuum pump, which exhausts into the environment.

Experiments are performed by first opening both globe valves and closing the leak hole with the rubber sheet. The vacuum pump is turned on and run until the vacuum pressure in the test chamber has a set value (nominally 7–10 kPa), after which the vacuum globe valve is closed and the pump turned off. The regulator on the CO_2 tank is opened to allow a small amount of CO_2 into the test chamber. While

experiments have been conducted with several different initial CO_2 levels, an initial concentration of about 7% by mass has been found to be most desirable. Once the specified value is reached, the globe valve leading to the CO_2 tank is closed. The leak cover is removed and air is allowed to flow into the system through the leakage hole. Data on CO_2 concentration and system pressure are recorded as functions of time using the LabView data acquisition system, with a one-second sampling rate. The test is continued until the vacuum pressure inside of the chamber has reached a second specified value.

The pressure and CO_2 concentration sensors were pre-calibrated by the manufacturer, but additional calibrations were performed prior to experimental testing using the manufacturer-provided calibration programs in order to avoid any error associated with sensor drift. The CO_2 sensor was calibrated by placing it in a gas of known CO_2 concentration, and similarly the pressure sensor was calibrated in a chamber of known pressure. A second pressure transducer and CO_2 concentration sensor were used to monitor the atmospheric conditions outside of the test chamber. These values are used in the data analysis when calculating the mass flow rate through the leak. In addition, temperature values were monitored every minute during testing both inside and outside of the chamber using digital thermometers.

3.2. Data Analysis

3.2.1. Data Reduction

The measured CO_2 concentration and pressure within the test chamber can be related to the mass flow rate through the leakage hole using the mass conservation equation for CO_2. This equation equates the rate of change of CO_2 in the test chamber to the rate that CO_2 is carried into the chamber by atmospheric air flow through the leak, which gives

$$\frac{d}{dt}[C_i(t)M_t(t)] = C_a Q(t)\rho_a . \tag{3.1}$$

In this equation, $C_i(t)$ and C_a are the mass concentrations of CO_2 in the test chamber and in the atmosphere, respectively, where for standard atmospheric conditions (101 kPa and 298 K) $C_a \cong 0.000394\,\%$ CO_2 by mass. Also, $M_t(t)$ is the total mass of all gases inside the test chamber, $Q(t)$ is the volume flow rate of leakage air, and ρ_a is the gas density within the test chamber. The rate of change of the total mass within the test chamber is given by a mass balance for air as a whole as

$$\frac{dM_t}{dt} = Q(t)\rho_a = \dot{m}(t), \tag{3.2}$$

where $\dot{m}$ is the mass flow rate of leakage into the system. Substituting (3.2) and using the chain rule, (3.1) becomes

$$\frac{dC_i}{dt} M_t + C_i \dot{m}(t) = C_a \dot{m}(t) . \tag{3.3}$$

Solving for $\dot{m}$ yields

$$\dot{m}(t) = \frac{M_t}{C_a - C_i} \frac{dC_i}{dt} . \tag{3.4}$$

Writing the mass of the gas in the chamber as $M_t = \rho_i V_t$, where $\rho_i(t)$ is the density of the gas mixture inside the chamber, (3.4) becomes

$$\dot{m}(t) = \frac{\rho_i V_t}{C_a - C_i} \frac{dC_i}{dt} . \tag{3.5}$$

The ideal gas law was used to find the gas mixture density. A molar mass of the mixture was obtained by comparing the mass fractions of air and CO_2 in the mixture. The molar mass of the mixture, $\overline{M}_i$ (kg/mol), was calculated from $\overline{M}_i = \left[\sum_{n=1}^{N} w_n / M_n \right]^{-1}$, where w_n is the mass fraction and M_n is the molar mass of the nth gas component. It is assumed that there are two components in the mixture,

standard air and CO_2. The ideal gas law then gives the mixture gas density as $\rho_i = p_i M_i / R_u T_i$, where p_i and T_i are the absolute pressure and temperature inside of the test chamber and R_u is the universal gas constant. It is noted that for pressures of approximately 1 bar and temperatures of approximately 300 K, the compressibility factor of air is Z=0.9999 (Perry and Green, 1984), so the use of the ideal gas law is well justified.

3.2.2. Data Smoothing

The leakage flow rate given by (3.5) is proportional to the rate of change of the CO_2 concentration C_i inside the test chamber. The value of C_i measured by the CO_2 concentration sensor is subject to noise due to sensor uncertainty and slight concentration fluctuations as the air flow within the test chamber is mixed by the turbulence generated by the fans. While the amount of noise is reasonably small, numerical differentiation of noisy data leads to a high level of uncertainty for dC_i / dt, and hence in the measured flow rate. However, because the time scale typical of the noise (≈1 Hz) in the concentration data is much smaller than that associated with the change in concentration rate due to leakage flow into the test chamber (≈0.0025 Hz), it is possible to smooth the concentration data to eliminate much of the effects of these fluctuations.

Two data smoothing approaches were used in this study. The first approach involves a spectral filtering of the C_i data using a method similar to that introduced by Orszag and Gottlieb (1980). Given a data stream for C_i over a time interval

(0,*T*), the spectral filter involves the following four steps: (1) reflect the data over the *t*=0 axis to generate a periodic data set over the time interval (−*T*,*T*), (2) expand the data stream in a Fourier series with N_F terms (the other terms being truncated), (3) multiply each coefficient of this series by a factor g_n, given by

$$g_n = \frac{1-\exp[-(N_F^2 - n^2)/N_o^2]}{1-\exp[-N_F^2/N_o^2]}, \tag{3.6}$$

where N_o is an adjustable parameter set to $2N_F$, and (4) compute the filtered data stream from the truncated Fourier series. The number of Fourier modes was selected to be $N_F = 25$ in the present experiments. A comparison of the filtered and unfiltered data obtained using this procedure is shown in Figure 24a.

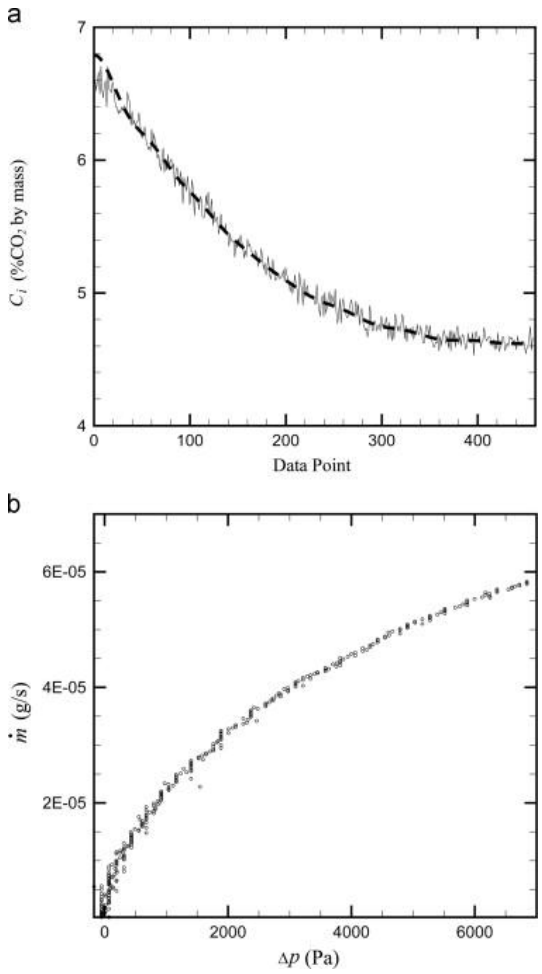

Figure 24. (a) Example showing the effect of the spectral filter (dashed) for removing high frequency noise from the experimental data (solid) and (b) sample results for flow rate through the leakage hole as a function of pressure difference. Experiments starting at different initial pressures fall unto nearly the same curve.

While the spectral filter removes the short time-scale oscillation in C_i, additional smoothing was implemented by use of the moving least-square procedure for differentiation of the measured data. In the moving least square method, a quadratic polynomial of the form

$$q_n(t) = a_n + b_n(t - t_n) + c_n(t - t_n)^2 \tag{3.7}$$

is fit to a set of M data points on each side of the point n at which the derivative is desired. The coefficients in (3.7) are set so as to minimize a least-square error of the form

$$E = \sum_{i=n-M}^{n+M} [C_i - q(t_i)]^2 , \tag{3.8}$$

which yields a 3×3 matrix equation for a_n, b_n and c_n. Once these coefficients are obtained, the derivative of the data stream at n is given by

$$\frac{dC}{dt}\Big|_n = b_n . \tag{3.9}$$

If M=1, the moving least-square procedure is equivalent to the centered difference scheme for numerical differentiation. Setting M>1 serves to smooth out fluctuations in the data. In the current study, the derivative of the CO_2 concentration was computed using M=20. An example of the mass flow rate data obtained from (3.5) using both of these smoothing methods is given in Figure 24b.

3.3. Error Assessment

3.3.1. Sensitivity to Initial Conditions

In order to assure the assumptions and equations used in the laboratory tests are valid, two tests were performed. The first test was conducted to ensure that mixing of the injected CO_2 is rapid and complete. To examine the effect of mixing on the experiments, tests were conducted both with and without the mixing fans turned on. The chamber was sealed, including the leak hole, and a small amount of CO_2 was injected into the test chamber. The concentration was monitored over time and the results of the tests can be seen in Figure 25. The results of these tests show that without the mixing fans in use, it took upwards of 30 min for the CO_2 concentration to reach a steady-state level. With the fans on, it only took around 10 s from the beginning of injection for a steady condition to appear (Figure 25b). This mixing time scale is much faster than the time scale associated with pressure change due to leakage into the test chamber (5–7 min), which shows that the assumption of a fully mixed flow is well satisfied when the mixing fans are turned on.

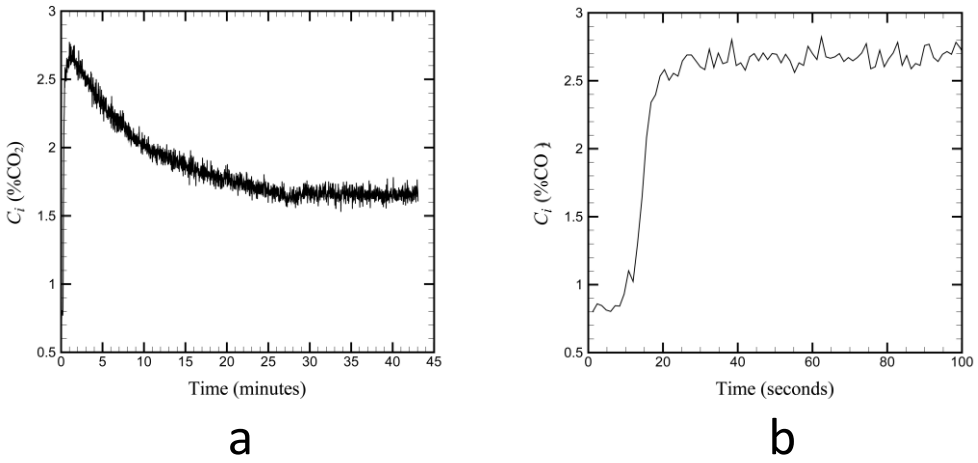

Figure 25. (a) Mixing test with CO_2 concentration monitored over 45 minutes with the mixing fans turned off; and (b) first minute and a half shown for mixing with the fans on.

The second test was conducted to ensure that the measured leakage flow rate is not sensitive to the initial value of the CO_2 concentration in the test chamber. To examine this issue, tests were repeated with five different initial concentrations values, all other variables being the same. Results of these tests are plotted in Figure 26. All five initial concentrations chosen are shown to collapse onto a single profile, validating Eq. (3.5). There is, however, a noticeable variation in measured leakage flow rate at values of vacuum pressure difference above 4.0 kPa, which appears to be due to transient error at the beginning of the tests. All tests were started with vacuum pressure $\Delta p = 5.0\text{kPa}$, and when air started flowing through the leakage hole it took several seconds for the entire system and data collection to reach a quasi-steady state. The size of the transient error was determined by comparison of the results to that of tests with higher values of the initial vacuum pressure. While this transient error occurs for all of the test cases examined, the error was smaller

for higher values of the initial CO_2 concentration. The best results during this transient period were observed for cases with 4–7% initial CO_2 concentration.

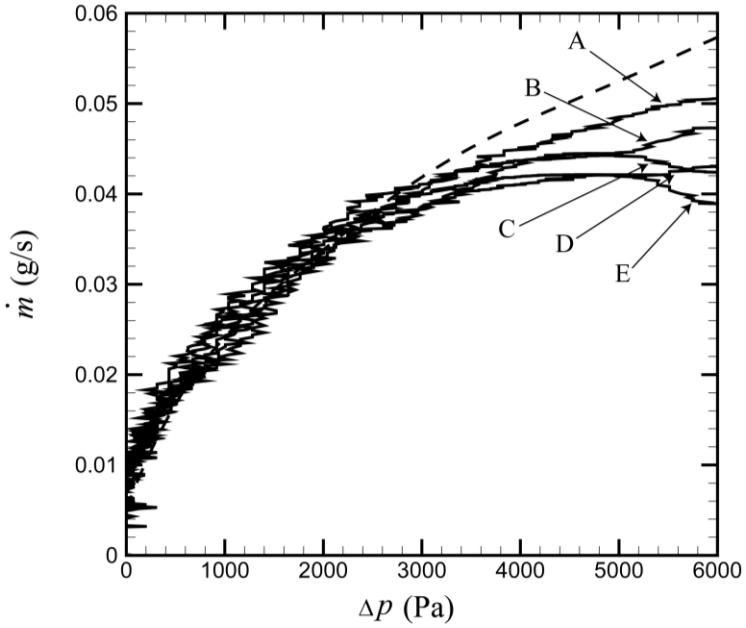

Figure 26. Laboratory tests with different initial CO_2 concentrations: 5.0% (line A), 3.8% (line B), 2.6% (line C), 2.0% (line D),1.5% (line E), and test results for a higher initial Δp (dashed). Higher values of initial CO_2 concentration yield more accurate results in the beginning part of the tests.

3.3.2. Uncertainty Estimate for Laboratory Experiments

Five of the measured variables introduce uncertainty in calculation of the leakage flow rate: (1) the test chamber volume V_t, (2) the density of the gas mixture inside the chamber ρ_i, (3) the CO_2 concentration in the atmospheric air C_a, (4) the CO_2 concentration in the test chamber C_i, and (5) the change in CO_2 concentration dC_i / dt. The gas mixture density also has error induced by the measureable variables of pressure, temperature, and CO_2 concentration inside of the chamber.

The uncertainty of the test chamber volume V_t was found by first examining uncertainty in measurement of the test chamber length, L. This uncertainty was based upon the resolution of the rule used to measure length, given by ΔL =0.0008 m. The volume measurement uncertainty is therefore given by $\Delta V_t = (L + \Delta L)^3 - L^3 \cong 3L^2 \Delta L \cong 2.2 \times 10^{-4}\,\mathrm{m}^3$. Both the atmospheric and chamber CO_2 concentrations were measured with a CO_2 concentration sensor that has a rated uncertainty of 3.0% of the sensor's reading (CO2Meter.com), or 0.01% CO_2.

Pressure values were measured using a digital pressure transducer (Omega Engineering) with rated accuracy of 0.3% of the sensor's full scale reading, or 300 Pa. Tests were performed only at room temperature, so that uncertainties in pressure measurements due to temperature variations do not affect uncertainty. The atmospheric temperature was measured with a digital thermometer with rated accuracy of 0.0556 °C. Additionally, temperature deviations during the laboratory testing process were recorded for uncertainty of temperature measurements. For the example case shown in Figure 24, atmospheric temperature variation during testing was approximately 0.11 °C.

The estimated uncertainty for the rate of change of concentration was challenging to determine because it was influenced both by sensor uncertainty as well as by the data filtering and smoothing methods associated with the spectral filtering and moving-least square numerical differentiation. Rather than trying to calculate this uncertainty directly from the uncertainty in C_i, it was chosen instead to determine it by comparing results for dC_i / dt from multiple test runs with the

same initial pressures and CO_2 concentrations. From a comparison of 10 tests, the experimental standard deviation in dC_i/dt based on root-mean-square difference of the results was found to be 5.2% of the measured value, yielding an expanded uncertainty of 10.4% of the measured value with a 95% confidence level.

The combined standard uncertainty in the leakage flow rate measurement, σ_Q, was obtained using the uncertainty propagation formula (Joint Committee for Guides in Metrology 2008)

$$\sigma_Q = \left[\sum_{i=1}^{N_V} \left(\frac{\partial Q}{\partial V_i} \right)^2 \sigma_i^2 \right]^{1/2}, \tag{3.10}$$

where V_i represents one of the i=1,…,N_V variables upon which Q depends and σ_i is the associated standard uncertainty in this variable. Substituting (3.5) into (3.10) and substituting the stated uncertainty values yields the desired measurement uncertainty results for leakage flow rate. A total expanded uncertainty with a given confidence level, E_Q, can be found by multiplying the combined standard uncertainty σ_Q by a factor k. For a 95% confidence level the value of k is approximately 2; so effectively the total expanded uncertainty is twice that of the combined standard uncertainty. For the purposes of this report, all values stated as 'expanded uncertainty' are given with a confidence level of 95%, including those found in the literature.

3.3.3. Estimation of Residual Leakage Flow Rate

Care was taken during fabrication of the laboratory testing device to ensure that leakages in the device itself were minimal. To determine a base leakage rate (i.e., the leakage from the system with the top cover closed), the test chamber was injected with CO_2 (to a 7% concentration) and adjusted to have the same vacuum pressure as in a standard laboratory test case (7 kPa). The system pressure, temperature, and CO_2 concentration were monitored for an extended period of time with the leak hole covered. After a period of approximately 10 min, the pressure in the chamber dropped by 120 Pa. During this testing period, the CO_2 concentration decreased by approximately 0.03817% by mass, which using (3.5) yields a residual leakage flow rate $\dot{m}_{res} = 3.3 \times 10^{-4}$ g/s. This residual leakage mass flow rate is two or more orders of magnitude less than that observed during testing with the leak hole open, and the pressure decrease is less than one percent of that observed in the tests with the leak hole open.

3.3.4. Comparison of Uncertainty with Other Leak Measurement Methods

While the error associated with other leak measurement methods can change based upon many factors such as the equipment used, precision of the instruments used to record data, geometry of the leak area, etc., a few sample cases are discussed for comparison with the proposed method. For instance, Sherman and Palmiter (1995) provide an uncertainty analysis for one type of blower door test

outlined in the ASTM standards, and the resulting expanded uncertainty in leakage rate was found to range between 16% and 29% of the measured values depending on the testing conditions. Sandberg and Blomqvist (1985) examined some different techniques for measuring leakage flow in a building or room with the tracer gas method. Expanded uncertainties were found to vary between 6% and 24% for the different techniques examined. However, the uncertainty values in the latter paper are likely underestimated because a constant concentration of tracer gas could not be guaranteed in the tests, which was not taken into account in the uncertainty calculation. A mass-spectrometry method for detection of the presence of a leak within a closed refrigeration system by Morgado et al. (2010) estimates total expanded uncertainty of about 5% or less depending on testing conditions. For testing higher flow rates with the use of flow meters in vacuum piping systems, Maqsood et al. (2013) found an expanded uncertainty for leakage rate of 8% for the stated testing conditions. Uncertainty for methods such as ultrasonic and infrared leak detection are not available for comparison, as these methods provide only a qualitative indication of leakage locations, instead of the leakage flow rate.

The combined standard uncertainty for leakage mass flow rate using the proposed method was estimated to be approximately 6%, giving an expanded uncertainty of 12% of the measured value, with uncertainty in pressure measurements of 300 Pa. While the proposed method has slightly higher expanded uncertainty than the best competing methods for specific applications, it has a significant improvement from the uncertainty of methods measuring leakages in

buildings and it has the ability to find local values of leakage rates in a variety of situations.

3.4. Numerical Simulation of Leakage through a Hole

3.4.1. Overview of Computational Method

Numerical simulations of flow through a hole in a plate, across which is imposed a pressure difference, were conducted in order to provide comparison data with which to validate results from the experimental leak detection apparatus. The computations were performed for an axisymmetric domain with steady-state, incompressible flow using an in-house CFD code (U2RANS) (Lai 2000). The highest velocities simulated had a magnitude of approximately 15.5 m/s, yielding a Mach number less than 0.05. This value is well below the commonly accepted upper bound of 0.3 for use of the incompressible flow assumption.

A multi-block structured grid was used composed of three blocks, as shown in Figure 27. The first (left-most) block is a square section representing the outside of the test chamber, where the left and top sides represent the inlets (atmosphere), the right side represents the wall of the test chamber, and the bottom side is the line of symmetry. The second block is a long rectangular region which composes the hole within the test chamber wall. The top surface represents the outside wall of the hole, and the bottom side is the line of symmetry. The final block is a mirror of the first block, and represents the inside of the test chamber. The grid spacing is rectangular and non-uniform. The non-uniform grid spacing was selected because

certain regions of the flow need higher resolution than others. For instance, regions near the inlets and outlets of the simulation involve nearly uniform flow and do not need many cells, whereas regions near the hole entrance and exits will have more complicated flow patterns and require more grid points for good resolution.

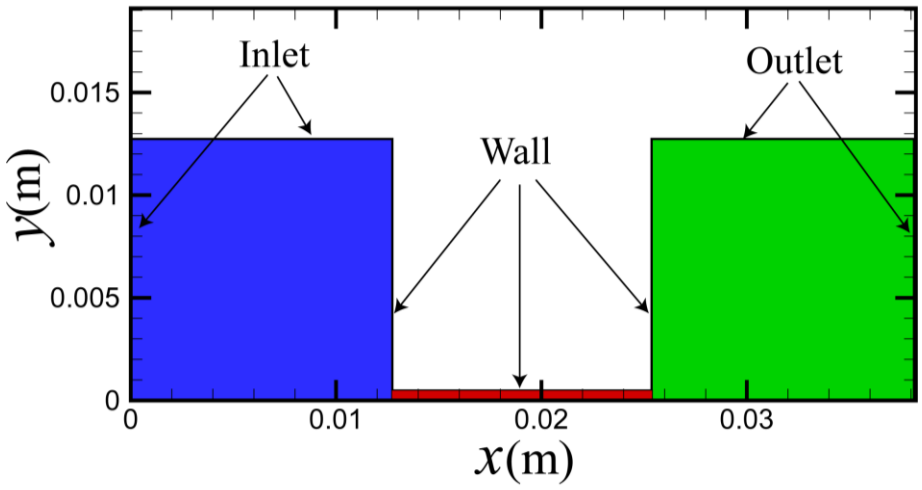

Figure 27. Sketch of the simulation domain slice in the *x*–*y* plane, where *x* is the axial and *y* is the radial coordinate of a cylindrical–polar coordinate system. Boundary conditions are labeled on inlet, wall and outlet boundaries. The *x*-axis represents the line of symmetry about which the domain is rotated. The blue block is the inlet region, the red block is the leak hole, and the green block is the outlet region.

The flow experienced in the leak detection device is a pressure-driven system; a pressure difference between higher pressure atmospheric air on the outside of the wall and the partial vacuum air–CO_2 mixture inside of the test chamber causes outside air to flow through the leak and into the test chamber. Because of CFD code requirements, velocity boundary conditions were used at the inlet and the pressure difference was computed as part of the solution. The inlet

velocity was specified to agree with the velocity field imposed by an axisymmetric point sink, given by

$$u_x = \frac{m(x - x_0)}{4\pi[(x - x_0)^2 + y)^2]^{3/2}}, \qquad u_y = \frac{my}{4\pi[(x - x_0)^2 + y^2]^{3/2}}, \tag{3.11}$$

here x is the coordinate along the hole axis, y is the radial coordinate of a cylindrical-polar coordinate system, and (x_0,0) is the position of the sink centroid. A point sink boundary condition was chosen to best model the flow field of a pressure driven system through a channel; where velocity is dependent on radial position away from the leak location and the sink centroid is taken to be the inlet of the leak. An iterative approach varying sink strength was then used to select a sink strength that yielded the desired pressure difference across the leak hole.

A sample region of the flow field is shown in Figure 28, showing the velocity magnitude contours and streamlines near the entrance region of the flow domain. At the inlet section of the domain the fluid traveled towards the leak hole and the velocity magnitude increased as approximately an inverse function of radius as the flow approached the hole. A recirculating bubble-type separation region is visible, which reattaches to the wall over a length L_r downstream of the entrance. The highest velocity magnitudes occur at the hole centerline within the part of the hole where this recirculation bubble exists. A thin jet flow emanates from the leakage hole into the exit chamber, which causes surrounding fluid to be entrained

into the jet, accompanied by a slow increase in jet area with distance away from the leakage hole. The existence of a thin jet in the leak outlet further supports the need for mixing fans in the test chamber.

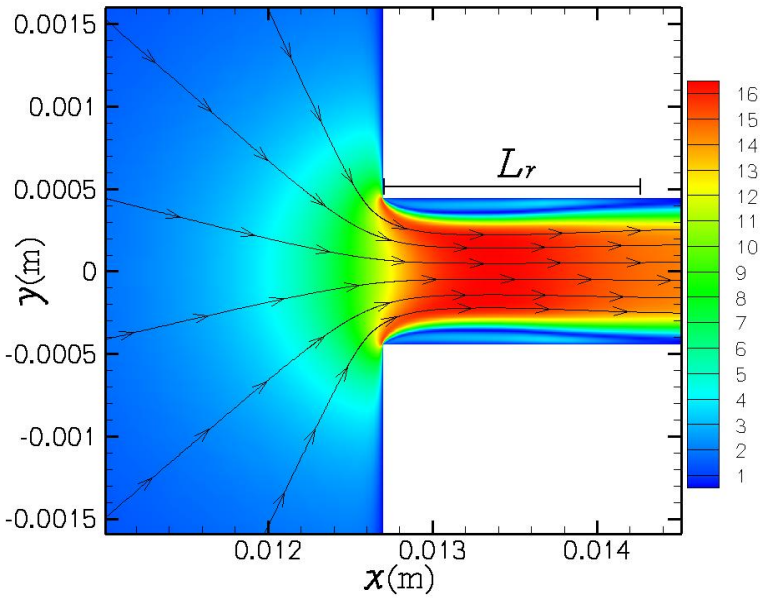

Figure 28. Simulation results for Δp=5.0kPa showing velocity magnitude contours (in m/s) for the entrance region to the hole with streamlines and length of recirculation region L_r.

To ensure realistic and reliable results from the simulation, a grid independence study was performed to ensure that the simulation results are not dependent on the grid size chosen. This test was performed by varying the number of cells in the axisymmetric computational domain from around 12,000 cells to 198,000 cells. Four parameters were monitored and plotted for varying cell numbers, including the pressure difference between the inside and outside of the test chamber (Δp), the length of the recirculation region (L_r) within the hole, the average velocity of the air exiting the leak hole (U_{av}), and the maximum velocity

inside the leak hole (U_{max}). Plots of these parameter values as functions of the number of grid cells are given in Figure 29. It was found that a change from roughly 122,000 to 198,000 cells had negligible change in all four parameters. From this result, it is safe to assume that the results of a simulation with a cell count of 122,000 are approximately independent of grid size.

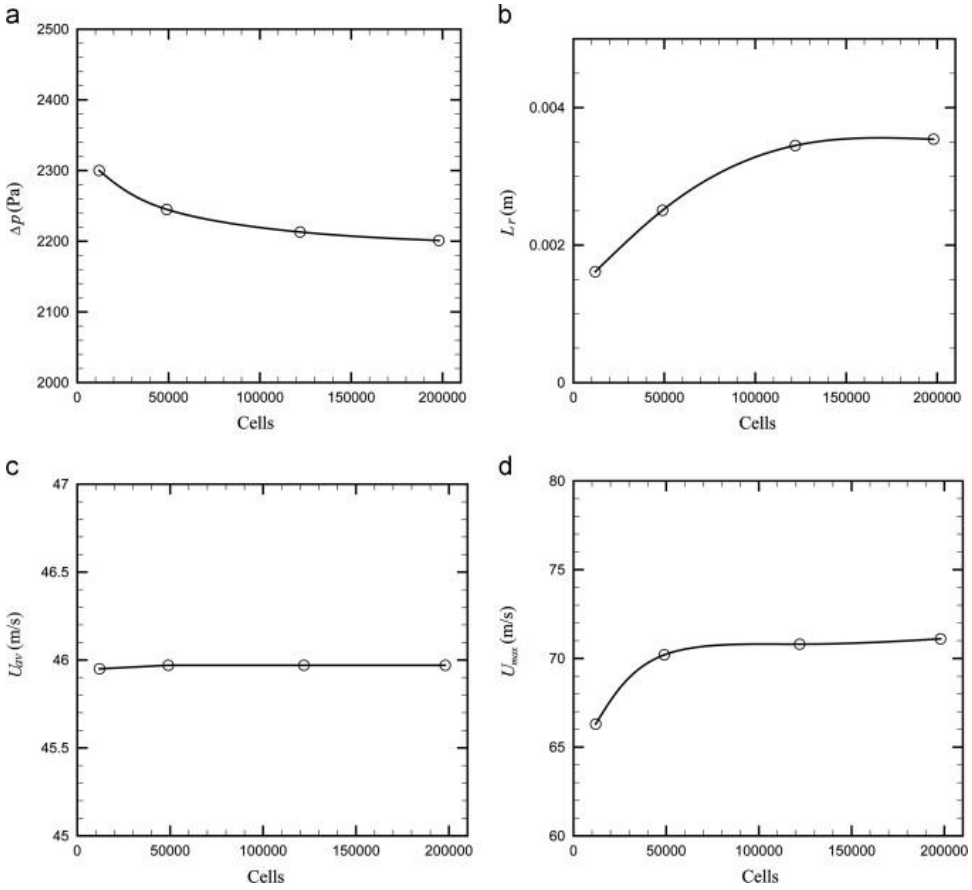

Figure 29. Grid independence study for: (a) change in pressure across leak hole (ΔP); (b) length of the recirculation region after the hole entrance (L_r); (c) average velocity of fluid exiting the leak hole (U_{av}); and (d) maximum velocity of fluid in the leak hole (U_{max}).

3.4.2. Uncertainty Estimate for Simulation Results

The leakage mass flow rate from the simulation results is computed from the average hole velocity U_{av} using

$$\dot{m} = \rho_a A U_{av}, \tag{3.12}$$

where ρ_a is the density of the air entering the hole and A is the cross-sectional area of the hole. Uncertainty in the simulated mass flow rate is determined using an error propagation equation similar to (3.10) for each of the three variables on the right-hand side of (3.12).

The air density was determined from the specific version of the ideal gas law

$$\rho_a = \frac{p_a}{R_{air} T_a}, \tag{3.13}$$

where p_a and T_a are the absolute pressure and temperature in the testing facility $R_{air} = 0.2869 \text{kJ/kg} \cdot \text{K}$ is the specific gas constant for air. The atmospheric pressure is measured using a digital pressure transducer with rated uncertainty of 0.3% the sensor′s full scale reading, which is 300 Pa (Omega Engineering). The atmospheric temperature was measured with a digital thermometer with rated accuracy of 0.0556 °C. With typical testing conditions of 101.3 kPa and 20.6 °C, the air density

was found to be 1.20 kg/m^3 with a combined standard uncertainty of 0.00182 kg/m^3 and total expanded uncertainty of 0.0164 kg/m^3, or 1.4% of the measured value.

The uncertainty in hole diameter d was estimated based on the calipers used to be $1.0\times10^{-5}\,\mathrm{m}$, so the resulting uncertainty in hole cross-sectional area A is given by $\Delta A=(\pi/6)[(d+\Delta d)^2-d^2]\cong(\pi/3)d\Delta d=1.0\times10^{-8}\,\mathrm{m}^2$. The uncertainty in average velocity was found using the results from the grid independence study. It was assumed that the error associated with the simulation could be taken to be the difference in U_{av} between the last two grid study cases, which was 0.005 m/s. After application of the uncertainty propagation equation, the combined standard uncertainty of the computed mass flow rate was found to be approximately 2.3% of the measured value, giving an expanded uncertainty of 4.6%. From examination of the uncertainty propagation calculations, the uncertainty in the hole diameter was the greatest cause for total uncertainty in the mass flow results of the numerical simulations. In fact, under equal pressure differences, it was found that slight changes in the value of d could cause huge changes in mass flow rate measurements. Coupled with the small hole size, this contributed to the vast majority of uncertainty in $\dot{m}$.

3.4.3. Uncertainty Estimate for Simulation Results

A comparison of the experimental data for leakage mass flow rate and the predictions of the numerical simulation as a function of vacuum pressure difference is shown in Figure 30. For the test shown, data was recorded starting at an initial

pressure difference of 10.3 kPa and an initial CO_2 concentration of 6.8%. The expanded uncertainty for the experimental measurements obtained in Section 3.3.4 was found to be approximately 12% of the measured mass flow rate value and 300 Pa for the measured pressure difference. The mass flow rate uncertainty is indicated by the two dashed lines on either side of the data. The uncertainty for the numerical predictions obtained in the current section is indicated by error bars in the figure. It is observed that in all cases the predictions of the numerical simulations are within the uncertainty range of the experimental data.

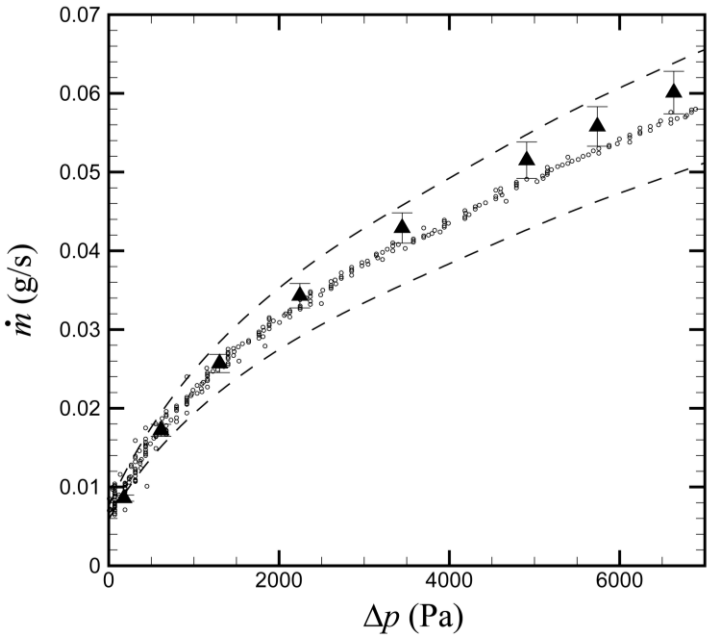

Figure 30. Comparison of leakage mass flow rate between experimental data (open circles) and the predictions of the numerical simulations (filled triangles) as a function of the vacuum pressure difference Δp. The expanded uncertainty for the experimental measurements is indicated by the dashed lines on either side of the data. The expanded uncertainty for the numerical predictions is indicated by error bars

3.5. Validation by Comparison with Correlation Data

A second type of validation of the experimental method is performed by comparing the experimental data with results of various empirical correlations obtained in the literature between volume flow rate and vacuum pressure difference with circular holes. A number of different correlations were identified, each with slightly different approaches and results.

A correlation was developed for air leakage rate through door assemblies and other small gaps by Gross and Haberman (1998) as

$$\dot{m} = \rho_a B A (\Delta p)^n , \tag{3.14}$$

where B is an empirical discharge coefficient, A is the cross-sectional area of the hole, Δp is the vacuum pressure difference across the gap, and n is an empirical exponent, with a value usually selected between 0.5 and 0.65. This equation can be seen to be identical to that of (2.5). Because of the heavy reliance on empirical parameters B and n, this equation exhibits significant variability in prediction of flow rates.

A study of fixed-area expansion devices used in the HVAC industry is given by Fang (1999). This study examines the literature for three main cases – orifices, short tubes, and capillary tubes – and also examines effects of two-phase flow on the flow rate in each case. As reported by Fang, many of the studies for multiphase flow through an orifice extend a simple equation for single-phase flow reported in

the ASHRAE Handbook – Fundamentals (1997), which gives the mass flow rate through a circular hole as

$$\dot{m} = C_d \rho_a A \sqrt{\frac{2\rho_a \Delta p}{1-\beta^4}}, \tag{3.15}$$

where the discharge coefficient C_d is given by

$$C_d = \begin{cases} 0.9199 - 0.014256 \log R_e + 0.016185 (\log R_e)^2 & 300 \le R_e \le 10^5 \\ 0.6 & R_e > 10^5 \end{cases} \tag{3.16}$$

Here, $\beta = d/\ell$ is the ratio of hole diameter d to length ℓ, and R_e is the Reynolds number, defined by $R_e = U_{av} d/\nu$, where U_{av} is the average velocity within the hole, d is the hole diameter, and ν is the kinematic viscosity.

A correlation reported by Ramamurthi and Nandakumar (1999) for flow through cylindrical orifices with sharp corners at the inlet and outlet gives the leakage flow rate as

$$\dot{m} = C_f \rho_a A \sqrt{2\rho_a \Delta p}, \tag{3.17}$$

where C_f is a discharge coefficient, defined by

$$C_f = 0.827 - 0.0085(\ell / d) . \tag{3.18}$$

An analytic study of gas leakage through very small orifices is reported by Bomelburg (1977), who assumed adiabatic, isentropic compressible flow with small pressure difference across the orifice. The resulting expression for flow rate is given by

$$\dot{m} = \alpha A \rho_a \varphi \sqrt{2 g P_a \rho_a} , \tag{3.19}$$

where

$$\varphi \equiv \left(\frac{\gamma}{\gamma - 1} \right)^{1/2} \left[\left(\frac{P}{P_0} \right)^{2/\gamma} - \left(\frac{P}{P_0} \right)^{(\gamma+1)/\gamma} \right]^{1/2} . \tag{3.20}$$

Here, α is the area correlation factor, which is empirically determined and is usually less than unity. This coefficient accounts for frictional losses and cross-sectional area reduction due to boundary layer effects. Also, g is the acceleration of gravity, $\gamma = c_p / c_v$ is the ratio of specific heats, and P_a and P are the absolute pressures in the atmosphere and inside the gas chamber, respectively.

Uncertainty for these correlations is caused both by error in the correlations themselves (correlation uncertainty) and by uncertainty in the measured variables

used in the equations (measurement uncertainty). Unfortunately, the original sources did not report a detailed uncertainty analysis by which to determine the correlation uncertainty. The measurement uncertainty for these equations can be estimated using the error propagation Eq. (3.10). The expanded uncertainty in these estimates, neglecting correlation uncertainty, were obtained as 4.4–30.0% of the measured value for Eq. (3.14), 4.6–30.0% of the measured value for Eq. (3.15), and 5.2–30% of the measured value for Eq. (3.17). These uncertainty estimates are dominated by the pressure uncertainty for lower values of the pressure difference. The uncertainty for higher pressure differences corresponds to the lower numbers listed above, whereas the higher uncertainty values correspond to lower pressure differences. The measurement uncertainty for Eq. (3.19) depends in a more complicated manner on the mass flow rate, and the expanded uncertainty is shown using error bars in Figure 31.

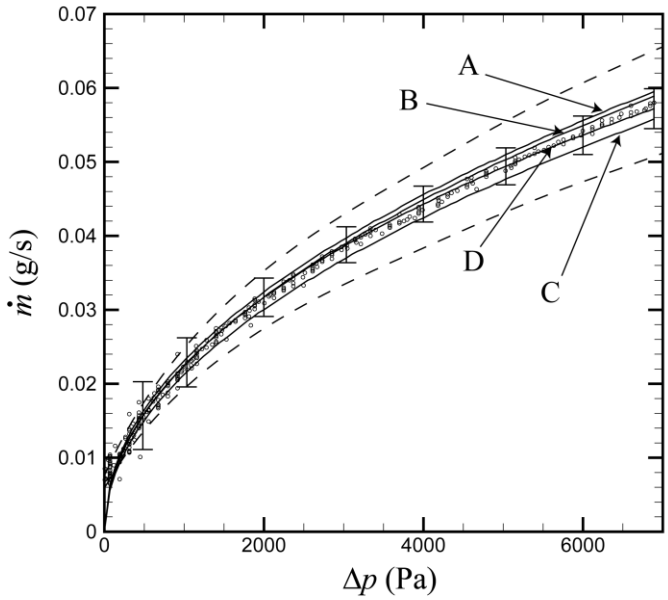

Figure 31. Comparison for leakage mass flow rate between experimental data (open circles) and correlations predictions from Eq. (3.14) with *B*=0.95 (line A), Eq. (3.15) (line B), Eq. (3.17) (line C), and Eq. (3.19) (line D) with α=0.24. The expanded uncertainty for the experimental measurements is indicated by the dashed lines on either side of the data. Expanded uncertainty for the first three correlations is stated in the text and error for Eq. (3.19) is shown by error bars.

A comparison of these leakage rate correlations with the experimental data from the leakage detection device described in Chapter 3.2 is plotted in Figure 31. The correlations given by (3.15) and (3.17) contain no adjustable parameters, and these correlations are therefore the primary means of empirical validation. By contrast, each of Eqs. (3.14) and (3.19) have an adjustable parameter that must be fit to the data, so while comparison with these correlations is also included; it must be regarded as a secondary type of validation. The experimental data shown in Figure 31 is found to be in close agreement with predictions of both of the correlations (3.15) and (3.17), as well as with predictions from (3.14) with a

discharge coefficient of B=0.95 and with predictions of (3.19) with α=0.24. In all cases, the agreement between the empirical results and the data obtained from the proposed leakage measurement approach were well within the margins of error for the laboratory experiments.

CHAPTER 4: PARTICLE CAPTURE DURING TRANSPORT THROUGH A CRACK

Chapter 4 of this thesis is an overview of the work pertaining to particle infiltration through cracks. As unwanted particles can be transported into buildings through such cracks, it is of great interest to understand the physics of how building envelopes can protect against particle infiltration via particle capture during such transport through cracks. Current models for particle penetration are based upon independent capture mechanisms of gravitational settling and Brownian diffusion and the multiplication of associated penetration factors. Prior research, however, neglects entrance effects on particle capture. Work expressed in this chapter is to better understand the fundamental mechanisms of particle capture due to entrance effects, and the non-linear interactions said entrance effects can have on the other two modes of particle capture. The studies performed use a purely numerical approach, in which fluid and particle simulations will be outlined. Many runs were performed which vary a number of important flow parameters, which will be discussed further in the following sections. Comparisons between numerical results to the current theory are performed such to (1) validate numerical results and (2) examine flaws in the current theory. Concluding remarks about this study can be seen in Chapter 5.

4.1. Computational Method

The numerical computations were performed for an incompressible fluid flow carrying particles from an upstream reservoir with pressure p_1 through a two-dimensional gap in a plane wall. The flow exits into a second reservoir with pressure $p_2 < p_1$, where the average fluid velocity within the gap separating the two reservoirs is denoted by *U*. To simplify the computations, it was assumed that both the particle concentration and the particle size are sufficiently small that particles do not influence the fluid flow.

4.1.1. Fluid Flow

Fluid flow computations were performed for two-dimensional, incompressible, steady-state flow using the CFD program Numeca FINE/Open. The computations were performed using a finite-volume method on an unstructured mesh formed with triangular elements. The mesh resolution is made very fine near the corner regions of the domain, where the gap channel joins the vertical walls shown in the schematic diagram of the flow domain in Figure 32, in order to ensure that fluid streamlines do not cut off the corners at the gap entrance. At these corners, the side length of the triangular element is reduced to 10% of the particle diameter. The flow domain consists of three regions: a square "inlet reservoir" on the left side of the domain, a long, thin rectangular section representing the gap channel, and a square "outlet reservoir" on the right side of the domain. Both the inlet and outlet reservoirs were chosen to be squares with side length 5*H*, where the

gap channel has width H and length L. The gap width and length were held fixed, with $L/H = 20$.

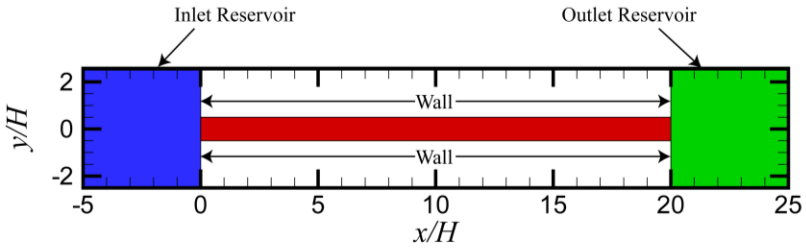

Figure 32. Sketch of the simulation domain in the *x*-*y* plane, where *x* is the axial and *y* is the radial coordinate of a cylindrical-polar coordinate system. The blue block is the inlet region, the red block is the channel hole, and the green block is the outlet region.

The flow through the gap is prescribed on the sides of the inlet reservoir using the assumption that far from the gap, the flow field is given approximately by that from a two-dimensional sink with volumetric flow rate q per unit distance along the line sink. This is the same boundary condition for the simulations discussed in Chapter 3 of this thesis given by (3.11), except for a sink located at the origin, where the velocity field far from the sink is given by

$$u_x = \frac{qx}{2\pi(x^2+y^2)^{1/2}}, \qquad u_y = \frac{qy}{2\pi(x^2+y^2)^{1/2}}. \tag{4.1}$$

An iterative approach was used to select a sink strength that yielded the desired pressure difference. Again, this boundary condition was needed because the program used to perform the simulation required velocity boundary conditions, and

a point-sink model of fluid velocity estimates the solution to a pressure driven flow through a uniform channel. For this case, the sink strength was varied until a non-dimensional average velocity of fluid in the channel of unity was reached. A sample flow field is shown in Figure 33, showing the velocity magnitude contours. Within the inlet reservoir, the fluid travels towards the gap and the velocity magnitude increases as approximately an inverse function of radius.

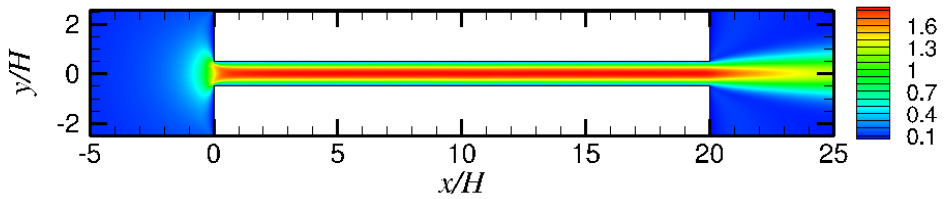

Figure 33. Fluid flow simulation result colored by dimensionless velocity magnitude $|\mathbf{u}|/U$.

A grid independence study for the fluid flow was performed to ensure that the simulation results are not dependent on the grid size chosen. This test was performed by varying the number of cells in the computational domain from around 51,000 cells to 493,000 cells in discrete steps. Two parameters were monitored and plotted for varying cell numbers – the pressure difference between the two reservoirs $\Delta p/\rho_f U^2$ and the maximum velocity inside the gap channel U_c/U. Plots of these parameter values as functions of the number of grid cells are given in Figure 34. The change in these parameters as the number of grid cells varies from roughly 281,000 to 493,000 is about 1.1% for the pressure difference and 0.02% for the maximum gap channel velocity. These small changes indicate that the numerical

solution has achieved a nearly grid-independent state with cell count of about 281,000 cells.

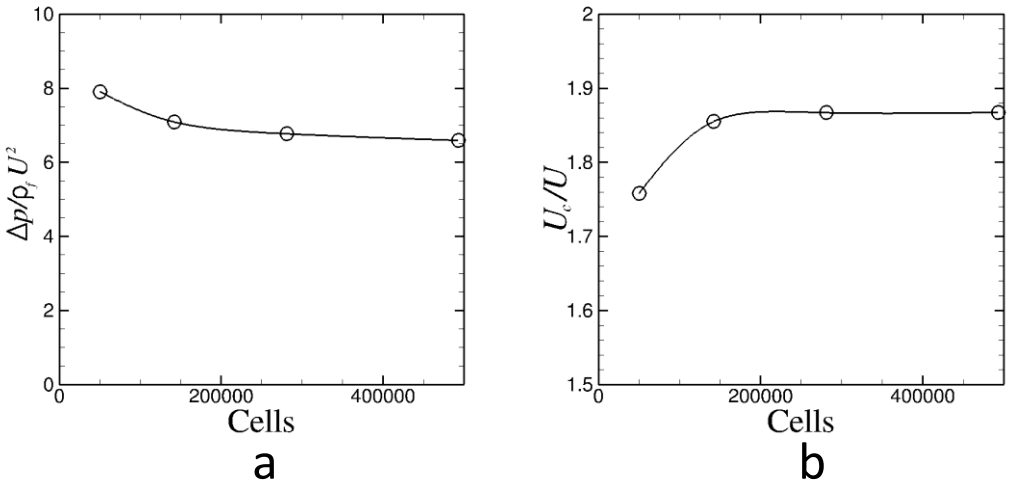

Figure 34. Grid independence study for: (a) change in pressure across the leak hole and (b) maximum velocity of the fluid in the leak hole.

4.1.2. Particle Transport

Particles are transported using the solution of the particle momentum equation and the particle moment of momentum equation, given by

$$m\frac{d\mathbf{v}}{dt} = \mathbf{F}, \qquad I\frac{d\mathbf{\Omega}}{dt} = \mathbf{M}, \tag{4.2}$$

where m is the particle mass, I is the particle moment of inertia, $\mathbf{v}$ is the particle velocity, and $\mathbf{\Omega}$ is the particle rotation rate. The fluid force on the particle $\mathbf{F}$ is dominated by the fluid drag $\mathbf{F}_d$, and for sufficiently small particles also to be influenced by the Brownian force $\mathbf{F}_b$. Particles were assumed to be spherical in

shape. While this is not a perfect representation of potential pollutant or smoke agglomerate shapes, there are a number of benefits to using the spherical assumption. In fact, mainly due to the extreme computational complexity of irregular shapes, it is standard in modern particle computations to assume spherical properties. This assumption means that relatively simple equations of particle transport can be used. It also allows for the examination of entrance effects on more principle levels. As an area of particle capture previously not well studied, for a first approach is it helpful to limit the potential number of parameters that can affect results. The inclusion of non-uniform geometry would complicate the examination of the physics behind entrance effects on the most basic level. Assuming small particle Reynolds number, the drag force is given for spherical particles by the Stokes drag law

$$\mathbf{F}_d = 3\pi\mu d(\mathbf{u} - \mathbf{v}), \tag{4.3}$$

where d is the particle diameter, $\mathbf{u}$ is the fluid velocity at the particle centroid (in the absence of the particle), and μ is the fluid viscosity. A viscous torque acts on the particle if the rotation rate is different than the rotation rate of the surrounding fluid element, and is given by

$$\mathbf{M} = \pi\mu d^3(\frac{1}{2}\boldsymbol{\omega} - \boldsymbol{\Omega}), \tag{4.4}$$

where $\boldsymbol{\omega}$ is the fluid vorticity.

The Boussinesq, added mass, and pressure gradient forces are negligible for this problem (Marshall and Li, 2014). The computations did include the Saffman lift force $\mathbf{F}_\ell$ and the Magnus lift force $\mathbf{F}_m$, given by

$$\mathbf{F}_\ell = -2.18\,\chi m\,\frac{(\mathbf{v}-\mathbf{u})\times\boldsymbol{\omega}}{\mathrm{Re}_P^{1/2}\,\alpha^{1/2}}, \qquad \mathbf{F}_m = -\frac{3}{4}\chi m\,(\frac{1}{2}\boldsymbol{\omega}-\boldsymbol{\Omega})\times(\mathbf{v}-\mathbf{u}), \quad (4.5)$$

where $\alpha \equiv \omega d/(2|\mathbf{v}-\mathbf{u}|)$, $\omega = |\boldsymbol{\omega}|$, and $\chi = \rho_f/\rho_p$ is the density ratio. The Saffman lift represents lift on a particle immersed in a uniform shear flow, where the particle is rotating at the same rate as the surrounding fluid elements. The Magnus lift represents an additional lift due to differential ratio rate between a particle and the surrounding fluid element. Bagchi and Balachandar (2002) showed that for particles rotating at some arbitrary rate in a shear flow, the sum of these two lift forces gives a close approximation to the total lift. The ratio of these forces to the drag force is given by $F_\ell/F_d = O(S^{1/2}d/H)$ and $F_m/F_d = O(S\,\mathrm{St}\;d/H)$, respectively, where $S \equiv \omega L^2/\nu$ is a dimensionless shear parameter and $\mathrm{St} \equiv \rho_p d^2 U/18\mu H$ is the particle Stokes number. The Stokes number represents a ratio of particle response time to fluid response time. Numerical results are

compared both with and without lift force to assess the significance of the lift force for this flow field.

Brownian diffusion is important for sufficiently small particle sizes. The Brownian force $\mathbf{F}_b$ is an uncorrelated random function with Gaussian probability distribution having zero mean and covariance given by

$$\left\langle \mathbf{F}_b(t)\mathbf{F}_b^T(t+\tau)\right\rangle = \mathbf{B}\delta(\tau), \tag{4.6}$$

where $\langle\cdot\rangle$ denotes the ensemble average and $\delta(t)$ is the Dirac delta. The coefficient **B** is a constant, second-order tensor given by

$$\mathbf{B} = 6\pi\mu d k_B T\,\mathbf{I}, \tag{4.7}$$

where k_B is the Boltzmann constant, T is absolute temperature, and **I** is the identity tensor. Substituting (4.3) and (4.7) into (4.2a) gives a stochastic differential equation for particle velocity of the form

$$m\,d\mathbf{v} + 3\pi d\mu(\mathbf{v}-\mathbf{u})\,dt = B^{1/2}d\mathbf{W}, \tag{4.8}$$

where $B = 6\pi\mu d k_B T$ and the components of the vector $d\mathbf{W}$ are independent random variables with Gaussian probability distribution having zero mean and variance dt.

Many of the applications with which particles infiltrate fluid barriers, such as smoke, are cases with either agglomerates of other smaller particles or liquid droplets. In either case, collision of the particle with a solid surface results in agglomeration of the particle onto the surface. Additionally, many of the larger sized pollutant particles have been found to have a high tendency to stick to any surface they come in contact with (Owen 1992). For this reason, in the current computations the particles are frozen in place when they collide with a solid surface either on the planar surface upstream of the gap or within the gap channel. Particles are not allowed to collide with other particles, due to the low particle concentrations considered, so these frozen particles are effectively removed from the computation.

The significance of particle inertia is characterized by the Stokes number St. The significance of the Brownian force is characterized by the particle Peclet number $\mathrm{Pe_p}$, which is defined by

$$\mathrm{Pe_p} \equiv v_S d / D_b , \tag{4.9}$$

where the characteristic particle slip velocity can be written as $v_S = |\mathbf{v} - \mathbf{u}| = O(\mathrm{St}\, U)$ and the Brownian diffusion coefficient is given by $D_b = k_B T / 3\pi\mu d$. The ratio of the magnitude of the Brownian diffusion force to drag force magnitude for a typical particle varies with the particle Peclet number as (Marshall and Li, 2014)

$$\frac{F_b}{F_d} = O\left(\mathrm{Pe_p^{-1/2}}\right). \tag{4.10}$$

The computations used a fixed value of the density ratio $\chi \equiv \rho_f / \rho_p = 0.0011$, and the ratio of particle diameter to gap width was varied over the interval $d/H = 5-15$. These values were taken from average smoke particle agglomerate diameter and density reported by Mulholland (1995), as well as common pollutant particles sizes reported by Owen (1992). The results are presented in terms of dimensionless variables, which are defined using the gap width *H* as a length scale and the mean velocity in the gap *U* as a velocity scale.

To generate fluid velocity values expressed at particle centers from the grid of the fluid simulations, two second order interpolation schemes were used. First, velocity values were interpolated from the unstructured grid into a uniform, structured grid with regions of varying grid size. Near the walls of the channel, grid spacing was chosen to be of the same dimension of the smallest triangular cell in the unstructured grid, with larger cell sizes used in regions far from the wall. This Cartesian grid was then used to interpolate velocity values onto particle center locations. Second order schemes were chosen for a number of reasons. First, interpolation schemes of higher order are difficult to implement when interpolating between triangular and rectangular mesh configurations. Additionally, second order interpolation schemes have been shown to be well performing for the flow conditions simulated in this study. Work by Yeung and Pope (1988) has shown that

higher order interpolation schemes are required to well-model particle transport in a turbulent flow; however for laminar flow (in which this study wholly examines) the use of second order schemes can be used with low error.

4.2. Results with Variable Stokes Number

A common parameter used to quantify capture of particles within a crack is the penetration factor P, defined as the ratio of particles that exit a crack to the total number of particles entering the crack for uniform upstream particle concentrations. There are a number of mechanisms that can give rise to hold-up of particles within the crack, including gravitational settling, Brownian motion, inertia, etc. The standard approach (Mosley et al., 2001) is to define a penetration factor for each of these mechanisms, such that the total penetration factor is the product of the individual penetration factors. The focus of this chapter is on particle collisions with the walls within the channel entrance region, so an entrance penetration factor P_E can be defined as the ratio of the number of particles passing through the entrance region to the total number of particles entering the entrance region. In this definition, the entrance region is taken to include the part of the flow domain just outside and just inside of the entrance within which the particles are strongly influenced by entrance effects.

In the computations reported in this section and the next section, the particles are injected randomly with a uniform probability distribution on a circular arc (called the particle injection arc) in the inlet (upstream) reservoir, spanning from

$\theta = \pi/2 - \varepsilon$ to $\theta = -\pi/2 + \varepsilon$, as shown in Figure 35. The small angular displacement ε is used so that the newly injected particles are not touching the side wall of the upstream reservoir. For the present computations, this is set so $\varepsilon = \sin^{-1}(d/2r_{inj})$, where r_{inj} is the radius of the semi-circle in which particles are injected. The objective of these computations is to sample the particle trajectory as a function of angular location on the particle injection arc. The ratio of number of particles to collide with the solid walls within the computational domain (either within the inlet reservoir or within the channel) to the total number of particles is defined as the capture fraction, F_c. It is noted that F_c is not equal to $1 - P_E$, as one might initially assume, because the radial velocity of the fluid on the particle injection arc is not uniform with position on the arc. If the particle concentration were uniform far away from the channel entrance, the particle injection rate at any location on the injection arc should be proportional to the radial velocity component. The results of the computations in this section will be converted into values for the entrance penetration factor in Section 4.4.1.

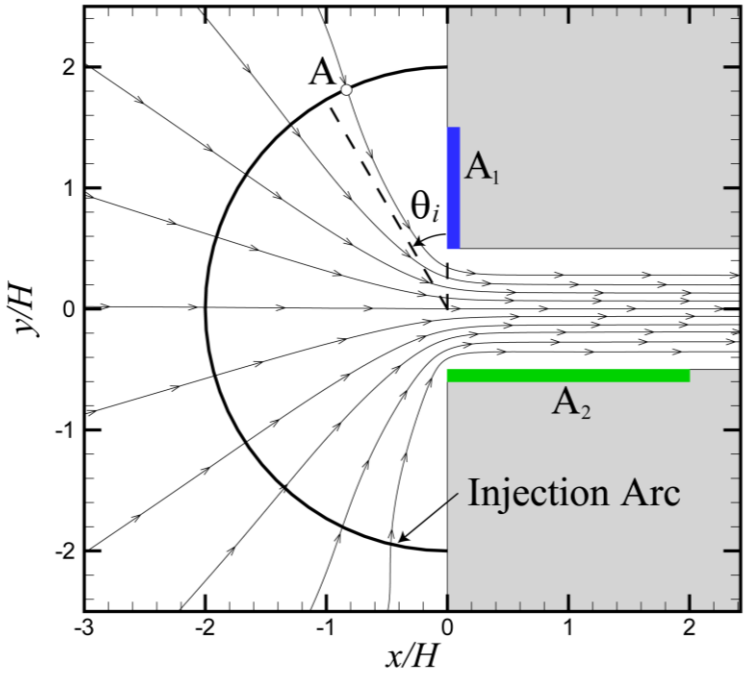

Figure 35. Crack inlet area with fluid streamlines, showing the particle injection arc (solid semi-circle) and the lines defining θ_i (dashed) for a particle A. Also shown are two regions, labeled A_1 and A_2, in which the particle tends to collide with the wall within the entrance region.

In the current section, particle transport within the entrance region for cases with no Brownian motion is examined. A range of Stokes numbers between 0 and 15 will be solved for three different particle diameters of d/H = 0.005, 0.010, and 0.015. Entrance region adhesion is caused by two distinct phenomena relating to how the fluid within the entrance region affects the particle trajectories. The method and location in which the particles adhere to the wall is strongly dependent on the Stokes number. Three distinct Stokes number ranges will be examined: (A) essentially zero Stokes number, (B) low Stokes numbers up to some critical value, and (C) Stokes numbers greater than the critical value. For Stokes number below a

critical value, the particles will collide with the wall on the outside of the entrance, within the inlet reservoir. For a particle A initiated in the upper part of the domain, this collision region is denoted by region A_1 in the schematic diagram in Figure 35. When the Stokes number exceeds a critical value, the particle's momentum is sufficient to allow it to cross over the channel and collide with the channel wall. This type of collision is indicated in Figure 35 by collision region A_2 for the particle A.

For a uniform crack located on a perfectly flat wall, fluid is funneled into the crack from all directions. Streamlines near the wall of the solid surface are seen to get closer and closer to the wall as they approach the crack inlet (see Figure 35). If the Stokes number is zero, particles follow fluid streamlines exactly. Therefore, if a particle is following such a streamline and the distance between the streamline and the wall becomes less than the particle radius, the particle will impact the wall within the inlet reservoir. For the assumption that particles always adhere to walls upon collision, this will equate to particle adhesion just outside of the crack inlet.

For the case of zero Stokes number, the fluid flow streamlines can be used to determine whether particles will collide with the wall for different values of the particle injection angle θ_i. The particle injection angle θ_i is defined as the angle between the vertical wall of the inlet reservoir and a line passing through the particle center at the time of initial injection and the center of the channel at the entrance (see Figure 35). The maximum value of θ_i that a particle can have in order to hit the wall at zero Stokes number, defined as $\theta_{i,\max}$, should coincide with

the particle colliding directly at the corner of the crack inlet. Assuming the particles are evenly distributed throughout the inlet region, $2\theta_{i,\max}/\pi$ will represent the percent of injected particles that hit the wall, and therefore the collision fraction is given by $F_c = 2\theta_{i,\max}/\pi$. A plot showing the capture fraction and value of $\theta_{i,\max}$ at zero Stokes number as a function of d/H is given in Figure 36. The values of the capture fraction shown in this plot are quite small, however.

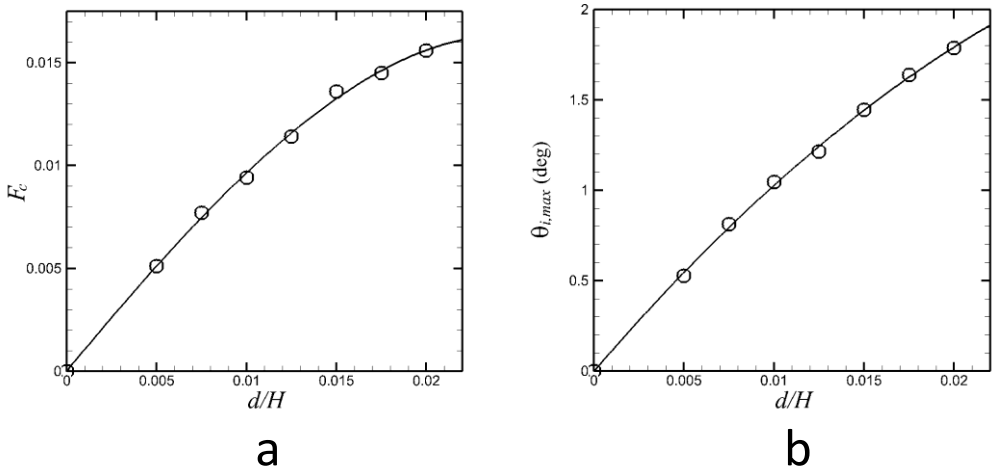

Figure 36. Results for a computation with zero Stokes number, showing (a) the capture fraction F_C and (b) the maximum collision angle $\theta_{i,\max}$, as functions of d/H.

When the Stokes number becomes finite, the particle pathlines start to deviate from the fluid streamlines because of particle inertia. Due to the streamline curvature as the flow passes around the inlet corner, particles drift away from the corner as they travel toward the crack inlet. This particle slip has the effect of decreasing the number of particles that hit the wall within the inlet reservoir, thus decreasing F_c. As Stokes number and particle inertia increase, this effect grows in

significance, such that fewer and fewer particles hit the wall within the inlet reservoir. A plot showing the particle capture fraction as a function of Stokes number is given in Figure 37a for the low Stokes number regime. The capture fraction exhibits significant decrease due to the streamline curvature effect as the Stokes number approaches unity, decreasing to less than half of the value observed for zero Stokes number. In these calculations, all particles with a value of θ_i less than $\theta_{i,\max}$ will collide with the wall of the inlet reservoir. A plot of $\theta_{i,\max}$ as a function of Stokes number is given in Figure 37b for this low Stokes number regime. Similar to the results in Figure 37a, there can be observed a significant decrease in $\theta_{i,\max}$ as St approaches unity as a result of streamline curvature.

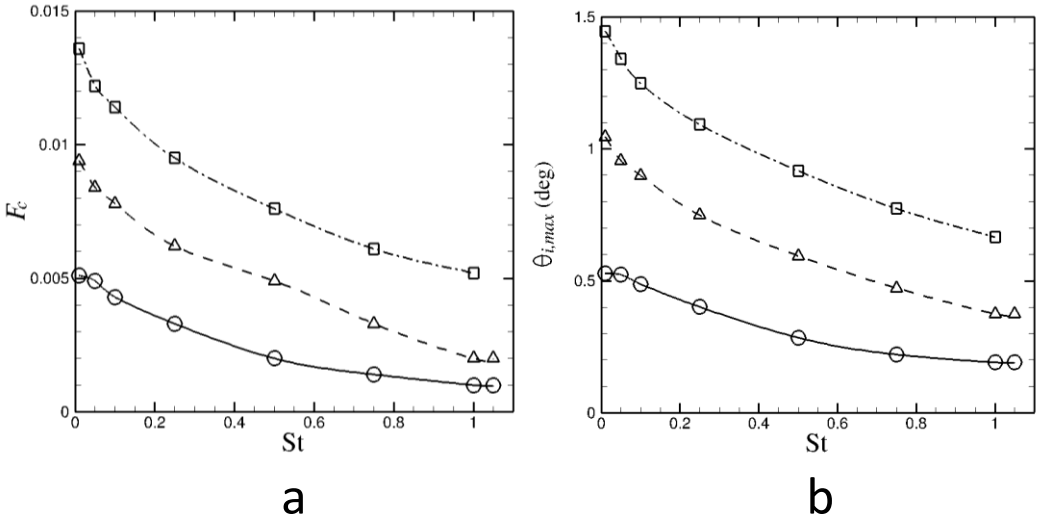

Figure 37. Plots showing (a) capture fraction F_c and (b) maximum collision angle $\theta_{i,\max}$ for particle collision as functions of Stokes number for the low Stokes number regime, with d/H of 0.005 (solid line with circles), 0.010 (dashed line with triangles), and 0.015 (dash-dot line with squares).

When the Stokes number exceeds a critical value (close to St ~1), a second type of particle capture occurs in which the particle inertia carries the particles across the channel within the entrance region and the particles collide with the wall on the opposing side of the channel. For instance, particle A in Figure 35 would collide in region A_2 in this case. For the d/H values examined in the range 0.005 – 0.015, the transition Stokes number occurred at $St_{trans} = 1.05 \pm 0.01$. While some particle collisions on inlet reservoir wall continued to occur after the transition Stokes number was passed, the number of collisions was low and continued to decrease as Stokes number increased. At sufficiently high Stokes number (between 3 and 5), no further collisions within the inlet reservoir were observed.

A plot of the capture fraction F_c as a function of Stokes number in the high St regime is given in Figure 38. For Stokes numbers between 1-3, computations with different values of d/H yield nearly the same values of capture fraction, but for Stokes numbers greater than about 3 the capture fraction exhibits significant differences for different values of d/H. Furthermore, the plots of F_c appear to achieve a maximum at a finite value of St and then to decrease with further increase in Stokes number. Both of these behaviors were unexpected for particles dominated by a balance between particle inertia and drag force. Upon further investigation, it was found that computations all values of d/H converge to the same curve if the lift force on the particles is turned off. As shown in Figure 38, this curve exhibits the expected monotonic increase of the capture fraction with Stokes number. The variation from this 'no-lift' curve, leading to the unusual behavior described above,

is due to the lift force acting on the particles, which becomes increasingly important with increase in Stokes number, especially for cases with low values of d/H. When lift force is included, the case with $d/H = 0.005$ has a maximum capture fraction of approximately 0.725 at a Stokes number of 4, while the other two diameters both have a maximum capture fraction of approximately 0.75 around a Stokes number of 7.5.

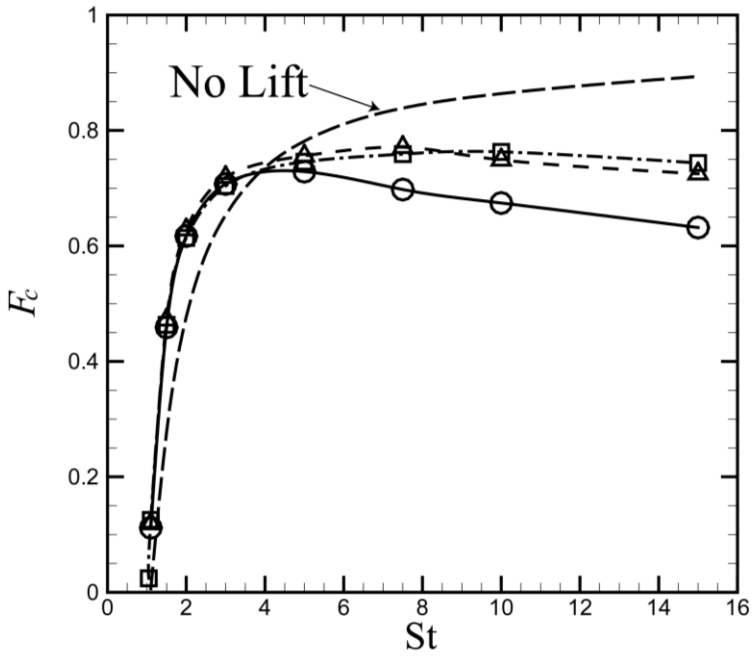

Figure 38. Capture fraction F_c plotted as a function of Stokes number for the high Stokes number regime, with d/H of 0.005 (solid line with open circles), 0.010 (dashed line with open triangles), and 0.015 (dash-dot line with open squares). The result from simulations without lift forces included is plotted using a long-dashed line, which was found to be independent of d/H.

For all particles that impacted the inside walls of the crack, the distance between the collision location and the corner was monitored. The ratio of this

distance with the channel width H is denoted by D_{edge}. A series of N_b bins were formed along the channel surface, and the number of particles colliding in each bin was counted during the computations. Dividing this number of collisions in each bin by the total number of injected particles and normalizing by bin length yields a collision distribution function f_d, which is plotted with $N_b = 100$ bins as a function of bin center location in Figure 39 for a computation with $d/H = 0.010$ and four different values of the Stokes number. The particle collision distribution has a strong one-sided structure, with the vast majority of particles impacting close to the leading edge the channel. In fact, there appears to be a minimum value of D_{edge}, which changes as a function of Stokes number, that yields the highest number of particle collisions, and beyond which the collision number drops to nearly zero. The value of this minimum collision distance, denoted by $D_{\min}$, is plotted in Figure 40 for a range of Stokes numbers and d/H values. The $D_{\min}$ values for all three values of d/H examined are observed to collapse onto a single curve.

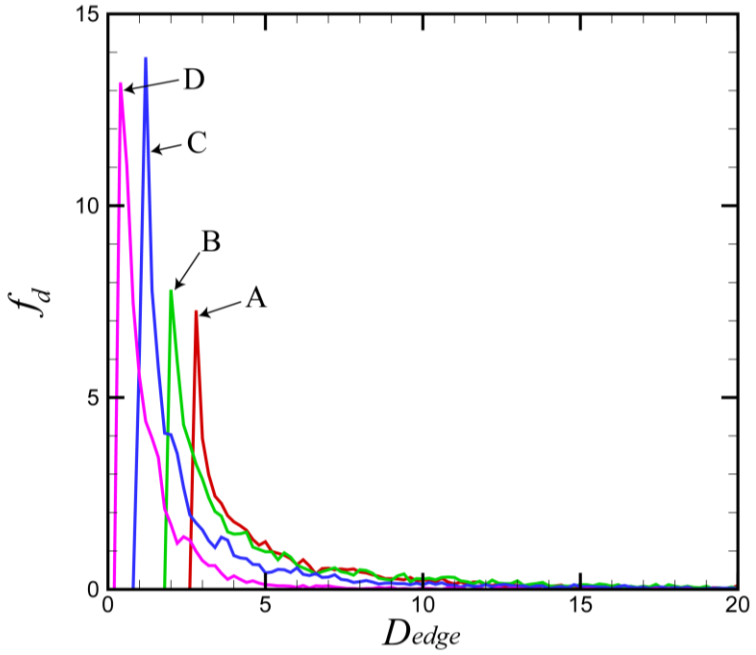

Figure 39. Plot showing the distribution of particle capture fraction, f_d, as a function of distance D_{edge} to the corner, for a calculation with 100 bins, each of width length $L/100$. The computations are for Stokes numbers of 2 (red line, A), 5 (green line, B), 10 (blue line, C), and 15 (magenta line, D).

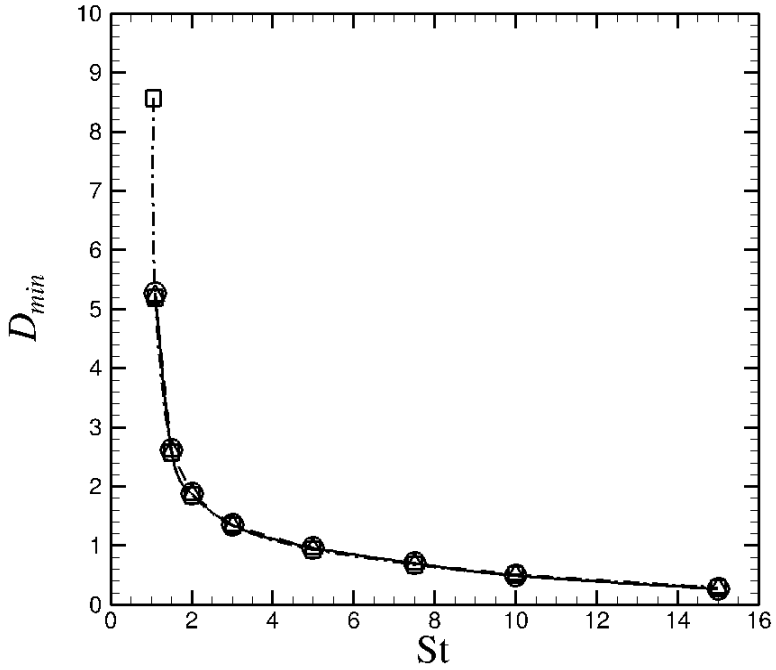

Figure 40. Minimum distance to the corner for particle collision, $D_{\min}$, plotted as a function of Stokes number for d/H of 0.005 (solid line with circles), 0.010 (dashed line with triangles), and 0.015 (dash-dot line with squares).

A plot of D_{edge} as a function of the particle injection angle θ_i is given in Figure 41 for a case with $d/H = 0.010$ and different values of the Stokes number. This plot is unusual in that there appears to be two values of θ_i that lead to particle collision on the channel wall at the same value of D_{edge}. The minimum value of D_{edge} corresponds to a critical injection angle value θ_{crit}, which varies as a function of Stokes number as shown in Figure 42a. This plot exhibits a local minimum of θ_{crit} around a Stokes number of 3 and a local maximum between a Stokes number of around 10-12. The phenomenon noted above occurs as a consequence of

boundary layer effects. In particular, for very small values of θ_i, the particle is close to the surface of the inlet reservoir and the fluid velocity within this boundary layer region is small. As a consequence, the particle has weak inertia as it approaches the channel corner. Even though the particle velocity is oriented directly toward the opposing wall of the channel when it moves past the corner, the particle lacks sufficient momentum to cross the channel. In the opposite extreme of large values of θ_i, particles are well outside of the boundary layer and have large momentum. However, in this case the particle velocity is primarily oriented down the channel, so the component of the velocity in the cross-channel direction is small. As a consequence, particles with vary large θ_i values are also unable to cross the channel to collide on the channel wall. Somewhere between these two extremes, there exists a range of θ_i values for which the particle is outside of the boundary layer (and hence has high momentum) and also has a trajectory such that a significant component of this momentum is oriented in the cross-channel direction, for which the net cross-channel momentum is a maximum. The value of θ_i in this latter case will correspond to θ_{crit}, associated with particles that collide at the minimum value of D_{edge}.

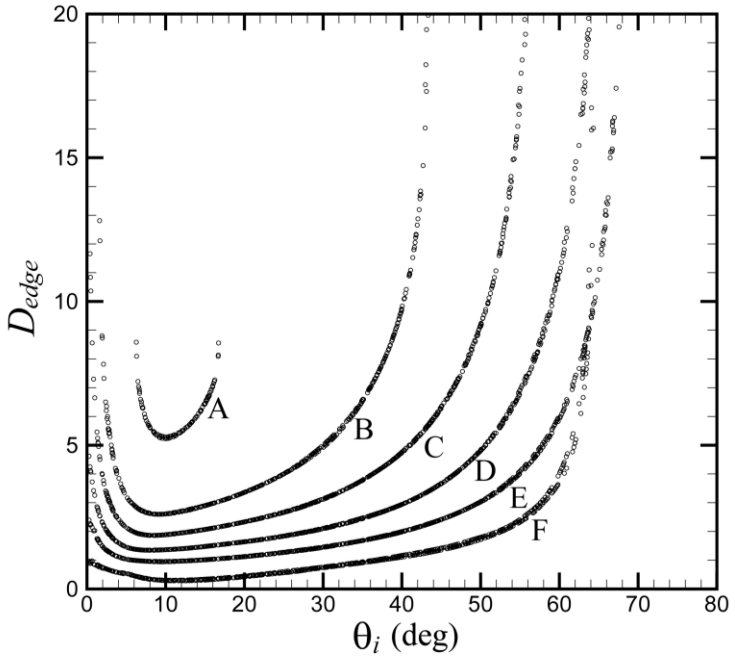

Figure 41. Collision distance from the corner, D_{edge}, plotted as a function of particle injection angle θ_i for $d/H = 0.010$ (open circles) with Stokes numbers of 1.1 (curve A), 1.5 (curve B), 2.0 (curve C), 3.0 (curve D), 5.0 (curve E), and 15.0 (curve F).

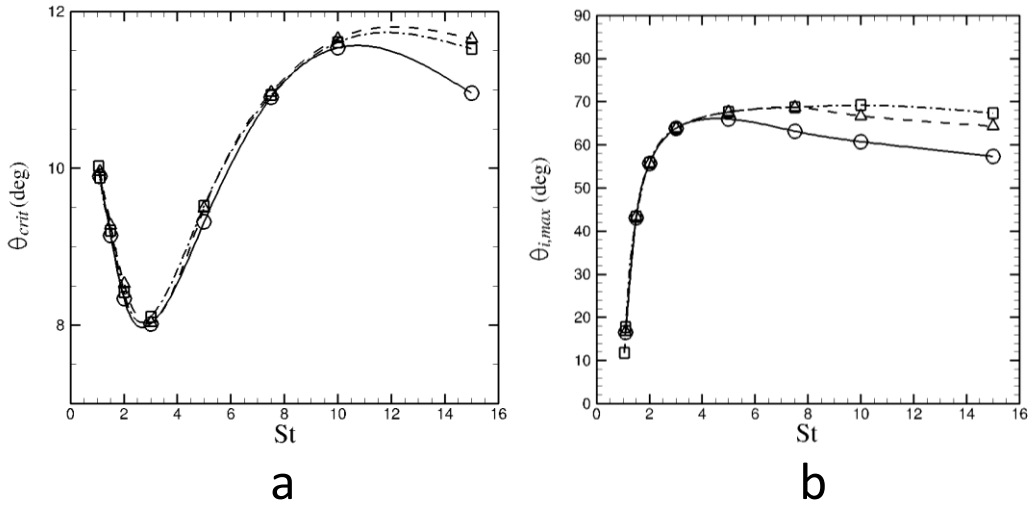

Figure 42. Plots showing (a) injection angle with smallest distance to the corner, θ_{crit}, and (b) the maximum injection angle for collision, $\theta_{i,\max}$, as functions of Stokes number in the high St regime for d/H of 0.005 (solid line with circles), 0.010 (dashed line with triangles), and 0.015 (dash-dot line with squares).

Also plotted in Figure 42 is the maximum value of θ_i, denoted by $\theta_{i,\max}$, beyond which particles do not collide with the channel wall. For $d/H = 0.005$, there is a peak $\theta_{i,\max}$ of around 65° at a Stokes number of 5. For d/H of 0.010 and 0.015, the peak occurs around a Stokes number of 10 with peak values of 66° and 68°, respectively. The general form of Figure 42b is similar to that for particle capture fraction shown in Figure 38.

4.3. Results with Variable Peclet Number

At very low Stokes numbers, Brownian motion forces can have significant effect on particle penetration into a crack, causing deposition of the particle both

within the crack channel and in the entrance region. As shown in (4.10), the significance of Brownian forces relative to the dominant drag force varies in proportion to the inverse square root of the particle Peclet number $\mathrm{Pe_p} \equiv v_S d / D_b$. Since the particle slip velocity v_S varies with time for each particle, the particle Peclet number is also time-varying. Additionally, a flow Peclet number $\mathrm{Pe_f}$ can be defined as $\mathrm{Pe_f} = UH / D_b$, which is constant for the flow field. Since for small Stokes number the particle slip velocity has the order of magnitude $v_S = O(\mathrm{St}\, U)$ (Marshall and Li, 2014), the flow and particle Peclet numbers are related by

$$\mathrm{Pe_p} = O\left(\frac{d}{H} \mathrm{St}\ \mathrm{Pe_f} \right). \tag{4.12}$$

Motivated by the above discussion, it is useful to plot the flow results in terms of a new parameter, called the Peclet coefficient C_P, by

$$C_P \equiv \frac{d}{H} \mathrm{St}\ \mathrm{Pe_f}\,. \tag{4.13}$$

From (10) we can write $F_b / F_d = O\left(C_p^{-1/2}\right)$, but the coefficient C_p is constant in time for a given flow.

A series of simulations were performed to examine effect of Brownian motion on capture of particles within the entrance region. For these simulations, the

Stokes number was fixed at 0.01 and the particle diameter was selected such that $d/H = 0.01$. The ratio of F_b/F_d was selected to vary from 0.15 to 4.5, which yields values of the flow Peclet number between 50 and 5,000,000 and of the Peclet coefficient C_p between 0.005 and 50. The injection arc is divided into 100 segments from 0-90°, and 100 particles are injected at the center of each segment of on the injection arc. Since the Brownian forces involve motion of the particles under a random force, the fate of each of these particles is tracked to develop collision probabilities for each segment of the injection arc.

Computations with small values of Peclet coefficient yield significant numbers of particle collisions both outside the crack near the inlet corner as well as on the walls of the crack channel. A plot showing the expected value of the capture fraction is given in Figure 43, with curves for particle collision on the inlet reservoir wall outside of the crack, within the crack channel, and total collisions. For the lowest value of Peclet coefficient considered, $C_P = 0.005$, the particles are strongly influenced by Brownian motion, resulting in a total capture fraction close to unity. Of this, about 20% of the particles collided outside the crack on the wall of the inlet reservoir, and the remaining 80% of the particles deposited within the crack. For the highest value of Peclet coefficient considered, $C_P = 50$, Brownian motion has little effect on the particle collisions and the value of capture fraction outside of the crack in Figure 43 is approximately the same as that given in Figure 37 with no Brownian forces.

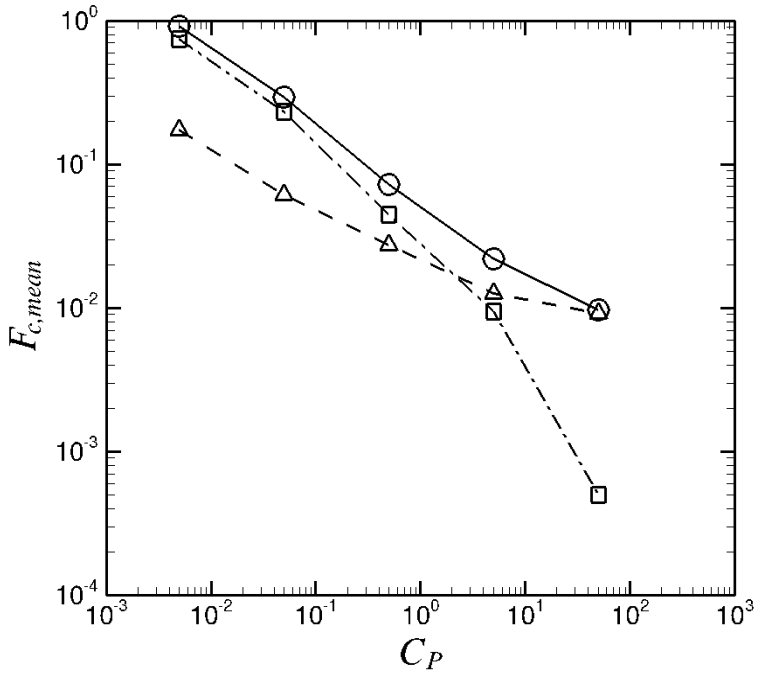

Figure 43. Mean capture fraction plotted as a function of the Peclet coefficient, showing total capture fraction (solid line and open circles), capture fraction for particles hitting outside the inlet corners (dashed line and open triangles), and capture fraction for particles hitting the inside channel walls (dash-dot line and open squares).

The collision probability is evaluated for each segment on the injection arc and plotted as a function of injection angle θ_i in Figure 44 both for collisions outside of the crack (Figure 44a) and within the crack channel (Figure 44b), denoted by $p_{c,corner}$ and $p_{c,chan}$, respectively. The random motion associated with Brownian forces gives particles an opportunity to collide with the crack wall when they otherwise would not collide from purely geometrical considerations. The distribution for $p_{c,corner}$ has high values, approaching unity, for low values of θ_i, since in these cases the streamlines carry the particles close to the walls. However, for low values of C_p, significant capture fractions were observed for values of θ_i

that are much higher than observed for simulations without Brownian motion. By way of comparison, with no Brownian motion the value $\theta_{i,\max}$ for this value of St and d/H was approximately 1°, whereas in the presence of Brownian motion with $C_p = 0.005$ the probability of particle capture is as high as 10% for $\theta_i = 40°$. The capture probability within the crack channel in Figure 44b is observed to have a maximum value at a finite value of θ_i, which increases with C_p, until for $C_p = 0.005$ the maximum occurs at $\theta_i = 90°$. The reason for this behavior is that particles with small values of θ_i tend to collide with the wall of the inlet reservoir outside of the crack channel, and so never pass into the crack. A study was performed in order to assure that the number of particles used was enough to generate an accurate probability density function. Simulations with twice and four times the normal amount of particles injected at each incremental injection degree were performed. Results from these tests yielded the same results and similar noise in probability density function values to that of the original trials, validating the use of 100 particles at each injection angle.

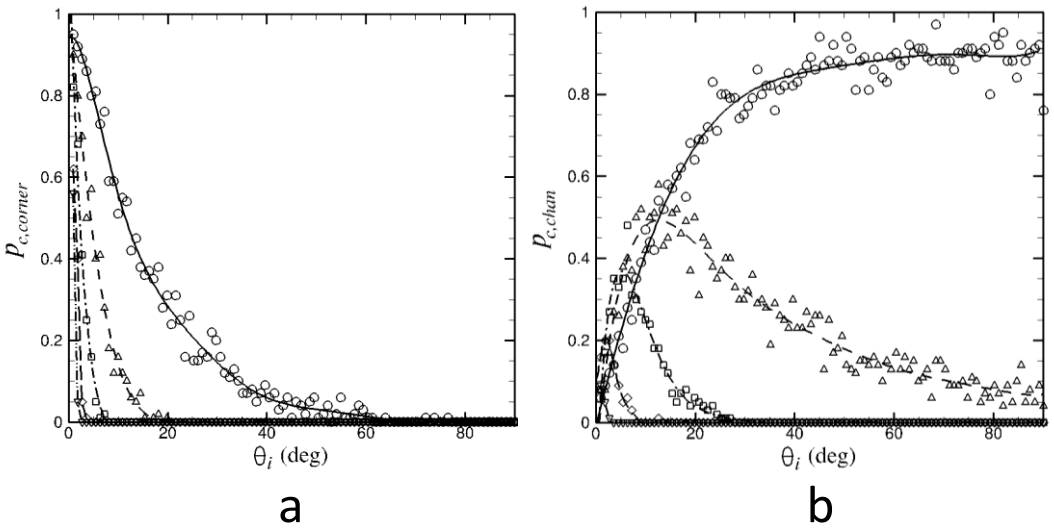

Figure 44. Collision probability of particles hitting (a) outside the inlet corners and (b) within the crack channel as a function of injection angle for $C_P = 0.005$ (circles and solid line), $C_P = 0.05$ (triangles and dashed line), $C_P = 0.5$ (squares and dash-dot line), $C_P = 5$ (diamonds and long dash line), and $C_P = 50$ (upside-down triangles and dash-dot-dot line). Curve fits are 10th order polynomials.

4.4. Discussion of Simulation Results

4.4.1. Calculation of Penetration Factor

The entrance region penetration factor P_E is defined as the fraction of the total injected particles that pass through the entrance region. Here, the entrance region is defined as that region of the flow within which particles are significantly influenced by the entrance effects, including the region just before the crack inlet and the part of the channel just downstream of the inlet. The penetration factor P_E can be related to the particle capture probability $p_c(\theta)$ by the following argument. Consider a problem in which the injection arc is subdivided into some number *M* segments, where *M* is sufficiently large that the arc across each segment can be taken as approximately a line segment with length $W = r_I \Delta\theta = \pi r_I / M$, where r_I is

the radius of the injection arc. Since the flow field is two-dimensional, an area-based concentration c is introduced and defined as the area of the flow field occupied by particles divided by the total area of the flow. If the absolute value of the radial velocity component at the ith segment on the injection arc is given by u_i and a new particle is injected at that segment with a time interval Δt_i, then the concentration can be written approximately as

$$c = \frac{\pi d^2 / 4}{r_I \Delta\theta u_i \Delta t_i}. \tag{4.14}$$

This expression becomes exact as $M \to \infty$. We now define an injection rate per unit arc length $\dot{n}_i$ by

$$\dot{n}_i \equiv \frac{1/\Delta t_i}{r_I \Delta\theta} = \frac{4 u_i c}{\pi d^2}, \tag{4.15}$$

where the latter expression is obtained after solving for Δt_i from (14). If we now take the limit $M \to \infty$, the penetration factor P_E can be written as

$$P_E = 1 - \frac{\int_0^{\pi} \dot{n}(\theta)\, p_c(\theta)\, r_I\, d\theta}{\int_0^{\pi} \dot{n}(\theta)\, r_I\, d\theta}. \tag{4.16}$$

Substituting the expression (15) for $\dot{n}(\theta)$ into (16) gives

$$P_E = 1 - \frac{\int_0^{\pi} u(\theta)\, p_c(\theta)\, d\theta}{\int_0^{\pi} u(\theta)\, d\theta}. \tag{4.17}$$

The radial velocity magnitude $u(\theta)$ was extracted from the fluid flow computation and is plotted in Figure 45. The capture probability $p_c(\theta)$ was determined numerically based on discrete element method computations in Sections 4.3 and 4.4. For the computations without Brownian motion, the capture probability is equal to unity if $\theta_i < \theta_{i,\max}$, and it is equal to zero otherwise. Plots of $\theta_{i,\max}$ versus Stokes number are given in Figure 37b for the low Stokes number regime and in Figure 42b for the high Stokes number regime. For computations with Brownian motion, the capture probability is plotted as a function of injection angle in Figure 44a for particle collisions on the outer surface of the inlet. Particle collisions within the channel due to Brownian motion occur all along the channel length; these collisions should be considered separately and not as part of the entrance penetration factor.

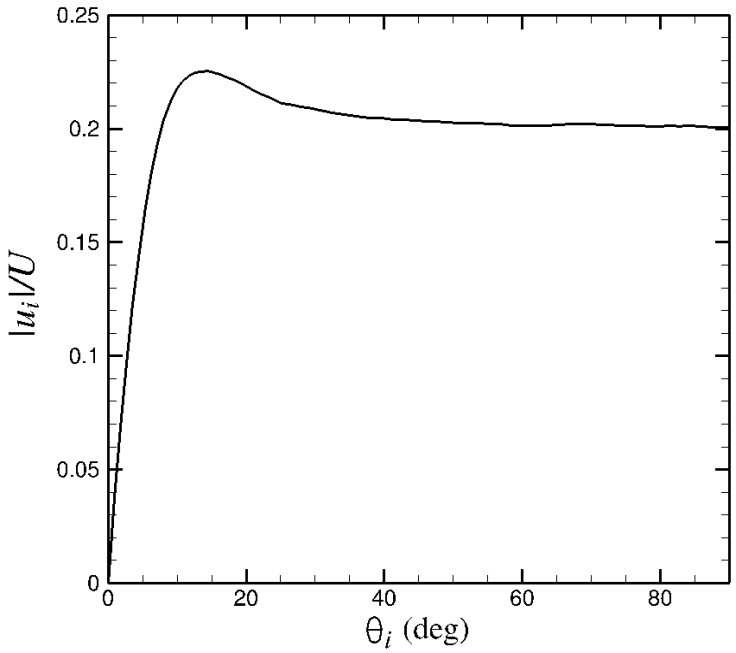

Figure 45. Plot showing fluid radial velocity magnitude as a function of angle on the injection arc, with resolution of 0.9 degrees.

The penetration factor is plotted as a function of Stokes number for computations without Brownian motion in Figure 46, for both the low and high Stokes number regimes. To recall from the discussion in Section 4.3, these two regimes correspond to different physical phenomena and particle collisions in different regions within the entrance region. The values of the entrance penetration facture shown in Figure 46a for the low Stokes number regime are very close to unity, with values above 0.9975 for all cases examined. As a consequence, it would appear that particle capture on the wall outside of the channel (region A_1 in Figure 35) is negligible for most practical cases without Brownian motion.

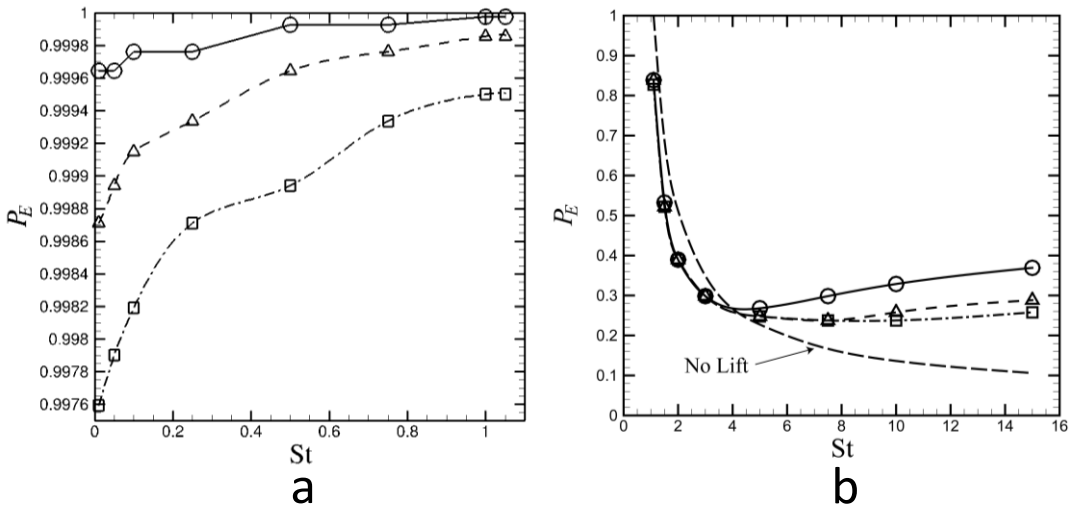

Figure 46. Entrance penetration factor plotted as a function of Stokes number for (a) the low Stokes number regime and (b) the high Stokes number regime, with d/H of 0.005 (solid line with circles), 0.010 (dashed line with triangles), and 0.015 (dash-dot line with squares). The case without lift forces included is given by the long-dashed line in (b).

The primary mechanism of particle capture due to the entrance region in the absence of Brownian motion would appear to be from collision with the opposing side of the channel as from that on which the particle enters (region A_2 in Figure 35), and collisions in this region only occur for sufficiently high values of the Stokes number. A rapid change in the value of P_E occurs between Stokes numbers of 1 and about 3, where the penetration factor decreases very rapidly from approximately unity at St = 1 to a value of about 0.28 at St = 3. As the Stokes number increases further the value of P_E in Figure 46b decreases very slowly, until it reaches a minimum value of 0.25 at about St = 7. For higher Stokes numbers the value of P_E does not exhibit significant change, but increases very gradually. The ability of the penetration factor to level out at high Stokes numbers and not decrease

further is due to the effect of lift force, as demonstrated by comparison to the results of the computation with no lift force shown in Figure 46b. The observation that up to 75% of the particles can collide with and be captured by the channel wall as a consequence of entrance effects for Stokes numbers above about 3 is a significant finding, which demonstrates the significance of entrance effects in particle passage through cracks at sufficiently high Stokes numbers.

4.4.2. Comparison of Brownian Penetration Factor with Theory

The other situation where entrance effects play a major roll on particle penetration is for cases with very low Stokes number where Brownian motion forces are significant. A plot of the entrance penetration factor as a function of the Peclet coefficient C_P is given in Figure 47 for computations with St = 0.01 and $d/H = 0.01$. For computations at small values of C_P, the penetration factor can be significantly reduced due to collision of particles outside of the channel entrance as a consequence of the random motion of particles that are carried close to the inlet reservoir wall by the converging fluid streamlines near the crack entrance. For instance, for $C_p = 0.005$ the value of entrance penetration factor was 0.86, indicating that about 14% of the particles are captured before they ever enter into the crack channel. As the Peclet coefficient increases to about 5 or greater, this effect becomes almost negligible and the entrance penetration factor approaches unity.

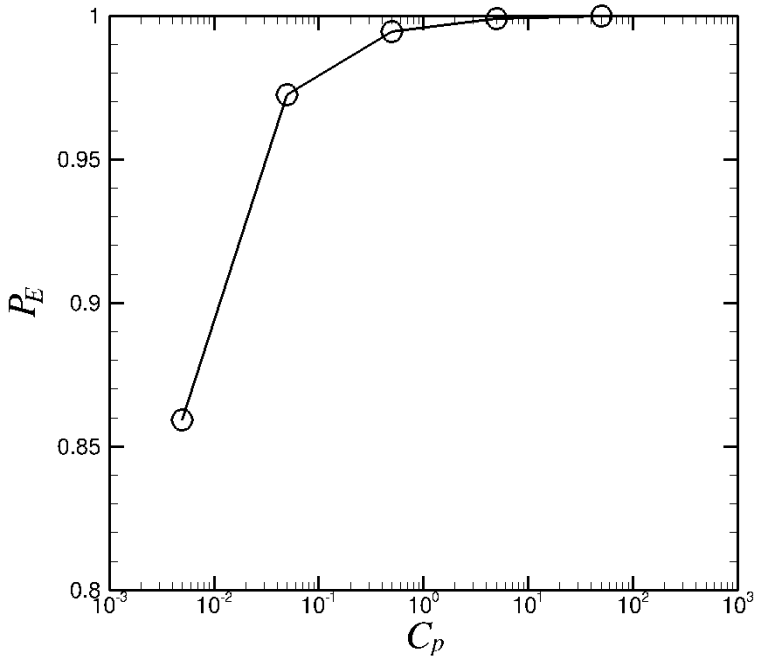

Figure 47. Entrance penetration factor for a computation with Brownian motion, with St = 0.01 and $d / H = 0.01$. The penetration factor is based on particles that collide outside the crack inlet corner.

The usual practice in prediction of dust infiltration through a crack, or other opening, is to write the total dust penetration factor *P* as the product of other penetration factors describing specific effects (Mosley et al., 2001). The dominant contributions to particle capture are usually assumed to be Brownian motion (for very small particles) and gravitational settling (for larger particles). The penetration factor for Brown motion within the channel derived by Lee and Gieseke (1980), given by (2.17), can alternatively be written in terms of the flow Peclet number $\mathrm{Pe_f}$ as

$$P_B = \exp\left(-\frac{7.868L}{H\ \mathrm{Pe_f}} \right). \tag{4.18}$$

One of the key assumptions used by Lee and Gieseke (1980) is that the particle concentration distribution $n(x, y)$ follows the equation

$$n(x, y) = n_\infty(x)\left[\frac{3}{2}\left(1 - \frac{2y}{H} \right) - \frac{1}{2}\left(1 - \frac{2y}{H} \right)^3 \right], \tag{4.19}$$

where x is the distance down the channel, y is the distance across the channel, and $n_\infty(x)$ is the channel center-line particle concentration.

Comparisons between (4.19) and the particle concentration profiles obtained from the DEM simulations are shown in Figure 48 for three different value of the Peclet coefficient. The concentration profiles are generated by counting the number of particles to pass through each of 100 different bins spanning the channel and then dividing by the total number of particles to pass through the channel cross section and normalizing by bin size. This procedure yields a normalized concentration value $n(x, y)/\bar{n}(x)$, where $\bar{n}(x)$ is the average particle concentration across the channel. The concentration distribution at the entrance ($x = 0$) is quite different from the expression (4.19) for all of the cases, but by $x/L = 0.1$ and at locations further downstream the concentration profiles agree reasonably well with (20) for the two cases with the highest Peclet number. The concentration profiles for the

case with the lowest Peclet coefficient appears to have more of a difference with the form (20) assumed by Lee and Gieseke (1980) even at the downstream locations.

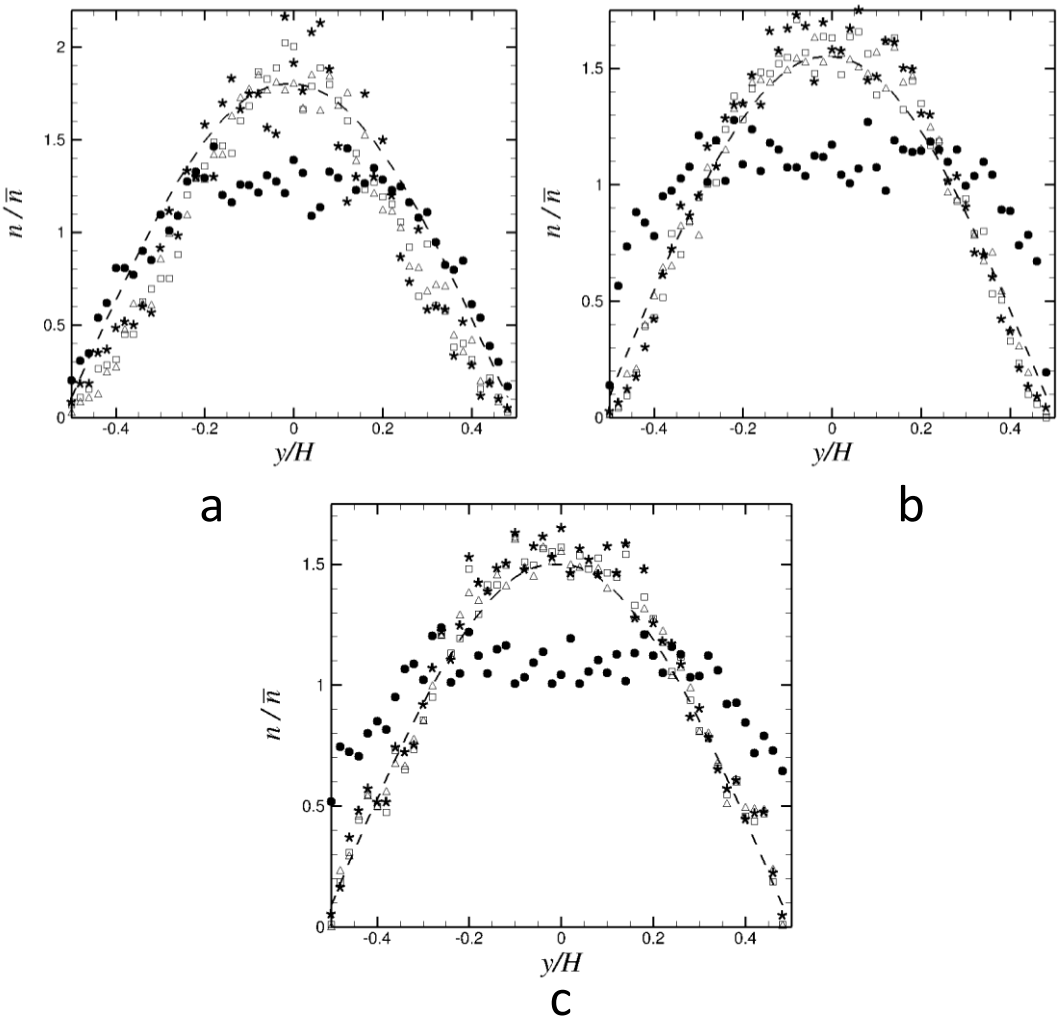

Figure 48. Profiles of the particle concentration $n(x,y)/\bar{n}$ at different distances along the channel for fluid Peclet numbers of (a) Pe_f = 50, (b) Pe_f = 500, and (c) Pe_f = 5000. The dashed line represents the concentration profile given by Eqn. (4.19), as assumed by Lee and Gieseke (1980). Profiles were taken at distances of zero (filled circles), $0.1L/H$ (open triangles), $0.25L/H$ (open squares), and $0.5L/H$ (asterisks) from the channel entrance. Values are normalized by the number of particles entering the channel as well as the bin size.

A comparison of the numerically computed Brownian penetration factor P_B, associated with capture of particles due to Brownian diffusion within the channel, with the theoretical expression (4.18) is given in Figure 49 as a function of channel length L/H. The numerical predictions are well fit by exponential curves, and for the two highest values of Peclet number considered the numerical data are close to the theoretical prediction (4.18). For the case with the lowest value of Peclet number, the theoretical prediction was somewhat lower than the numerical data. This difference is likely due to the aforementioned disagreement between the particle concentration profiles and the concentration profile (4.19) assumed by Lee and Gieseke (1980).

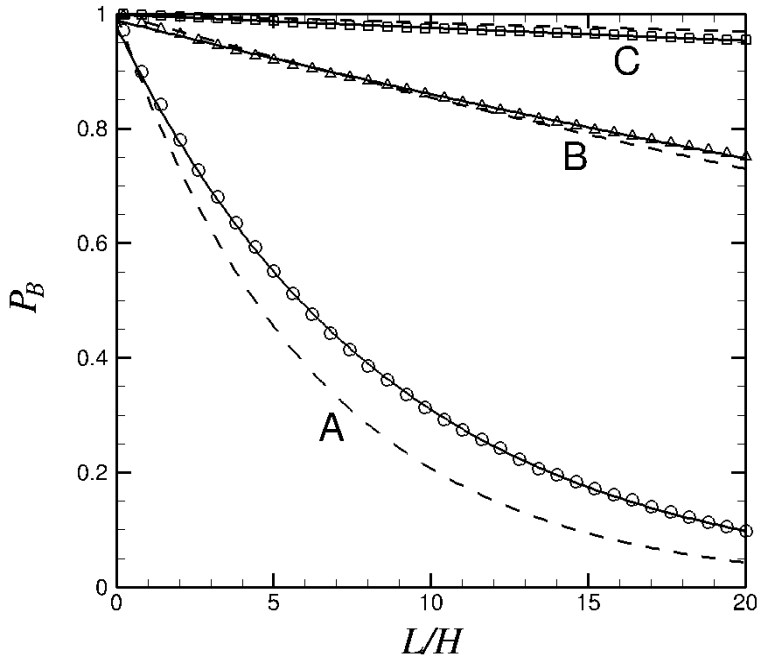

Figure 49. Comparison between the computed predictions for the Brownian penetration factor P_B inside the channel (symbols with solid exponential fit lines) and the theoretical prediction of Lee and Gieseke (1980) (dashed lines). Results are given for cases with fluid Peclet numbers of Pe_f = 50 (A, circles), Pe_f = 500 (B, triangles), and Pe_f = 5000 (C, squares).

4.4.3. Evaluation of Penetration Factor Independence

An expression for the penetration factor due to gravitational settling, P_G, was derived by Fuchs (1964) assuming uniform flow in the channel and uniform inlet particle concentration profile, which gives

$$P_G = 1 - \frac{v_G L}{HU} = 1 - \frac{\mathrm{St}}{\mathrm{Fr}^2}\frac{L}{H}, \tag{4.20}$$

where v_G is the terminal particle settling velocity and the Froude number is defined by $Fr = U/\sqrt{gH}$. For simulations at moderate to high values of the Stokes number, entrance effects can significantly modify the particle concentration distribution at the channel inlet, which leads to a nonlinear interaction between the entrance effects and the gravitational capture of the particles in the channel. To illustrate this effect, profiles of the normalized particle concentration $n(x,y)/\bar{n}(x)$ are shown in Figure 50 for a moderate Stokes number of 2. These profiles demonstrate clearly that the concentration field is far from uniform. At the crack inlet, the profile exhibits two strong peaks on either side of the centerline. By a distance of $x = 0.1L$, the profile has become nearly flat, but then as the particles progress down the channel the concentration peaks near the centerline, which likely occurs as a response of the particles to lift forces associated with the shear flow in the channel.

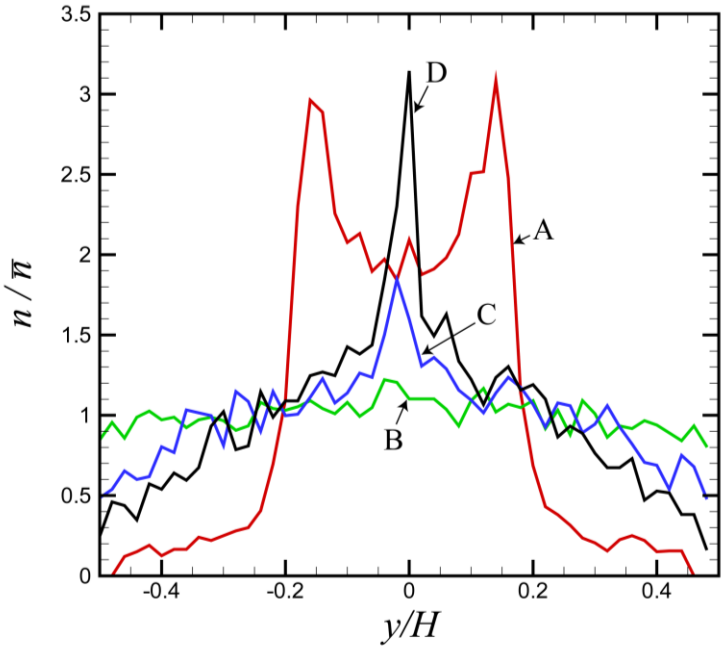

Figure 50. Profiles of the particle concentration $n/\bar{n}$ at a Stokes number of 2.0. Profiles were taken at distances from the channel entrance of zero (A, red line), $0.1L/H$ (B, green line), $0.25L/H$ (C, blue line), and $0.5L/H$ (D, black line).

A common practice in particle infiltration studies is to multiply the different penetration factors together to obtain the total penetration factor for the crack system (Mosley et al., 2001), which is based on the assumption that the different penetration factors are independent of each other. The fact that particle inertial effects within the entrance region can lead to highly non-uniform concentration profiles at moderate Stokes number values can lead to breakdown of the assumption of independence of the entrance region and gravitational settling penetration factors. The validity of the assumption of penetration factor independence was examined by performing a series of simulations for particle passage through the entrance region and channel with the gravitational force included for different

values of Stokes and Froude numbers. Computations are performed for Stokes numbers between 0 and 15 and for Froude numbers of 10 and 14.

The total computed penetration factor P_{tot} from these computations is compared in Figures 51 and 52 with the product of the entrance region penetration factor P_E obtained previously for simulation with no gravity as a function of Stokes number (Figure 46) and the theoretical expression (4.20) for the gravitational penetration factor P_G. The expression $P_{tot} = P_E \cdot P_G$, indicated by a dashed line in Figure 51, is the limit in which the two penetration factors are independent, so that P_E can be computed with no gravity and P_G can be computed without accounting for particle entrance or inertial effects. Each computation shown in Figure 52 was performed twice, once with lift force included (open symbols) and once without lift force (filled symbols). It is noted that in the lower portion of the channel, lift force counteracts gravitational force by pushing particles toward the channel center while the downward pull of gravity pushes the particles toward the channel wall.

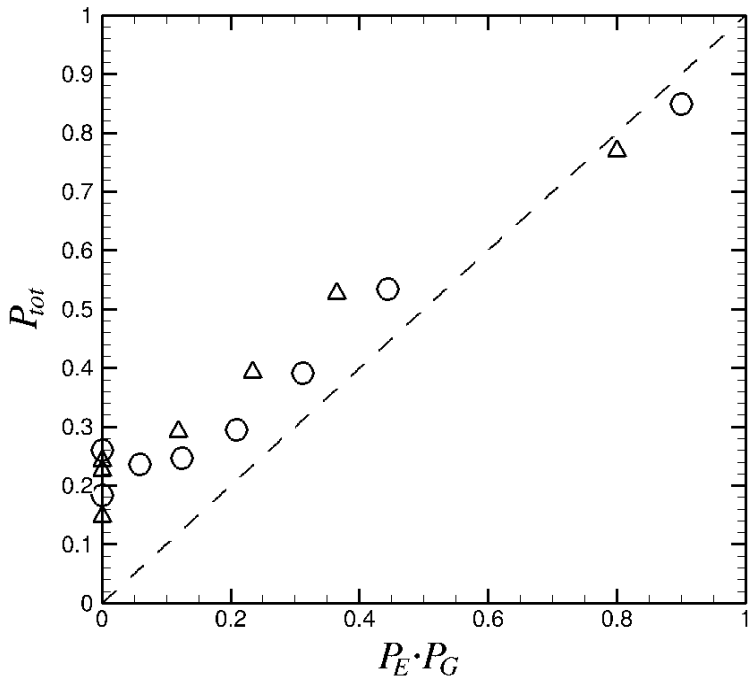

Figure 51. Comparison of the total penetration factor P_{tot} found in the numerical simulations with the product of P_E and P_G. Results for simulations are given for Fr = 10 (open triangles) and Fr = 14 (open circles). The dashed line represents the limit of independent penetration factors, for which $P_{tot} = P_E \cdot P_G$.

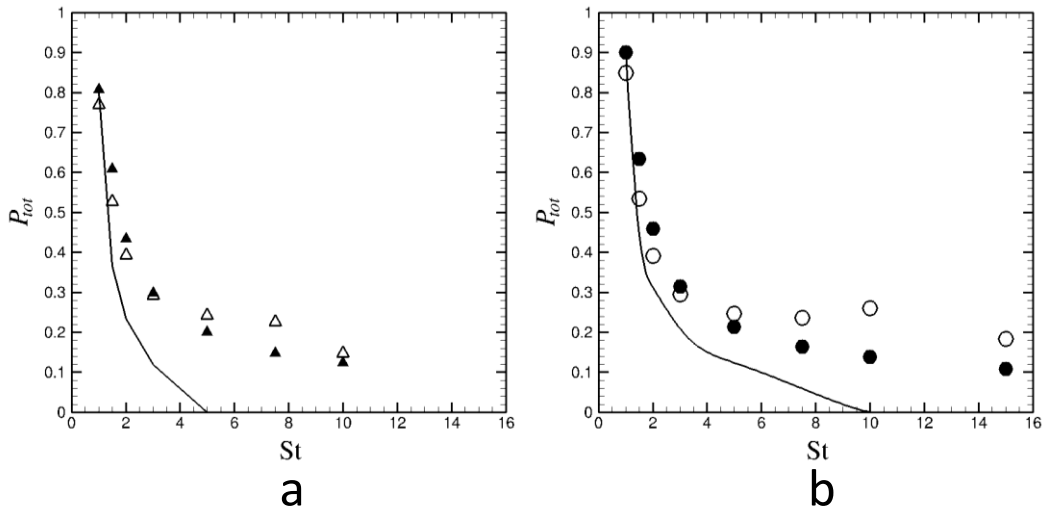

Figure 52. Plots of the total penetration factor P_{tot} found in the numerical simulations as a function of Stokes number for cases with (a) Fr = 10 and (b) Fr = 14. Open symbols denote numerical results with lift force included, filled symbols denote numerical results without lift force included, and solid lines denote the result $P_{tot} = P_E \cdot P_G$ obtained by the assumption of penetration factor independence.

Results for lower values of Stokes number yield values of P_E close to unity, for which case the total penetration factor is dominated by gravitational settling. Such cases correspond to the points with large values of P_{tot} in Figures 51-52. As the Stokes number increases, the values of both P_E and P_G decrease and become more comparable to each other. In these cases, with P_{tot} values between about 0.7 and 0.3, the penetration factor independence formula $P_{tot} = P_E \cdot P_G$ results in a significantly lower value of the total penetration factor than that observed from the full numerical simulations, as shown in Figure 51. As the Stokes number exceeds some critical value that depends on the Froude number and the channel length to

width ratio, the value of P_G in (4.20) decreases to zero, so that the product $P_E \cdot P_G$ yields a zero value of the total penetration factor. However, the numerical computations continue to result in a finite value of the total penetration factor (of about 0.2) for these cases.

This observation also applies for computations performed without lift force, only in this case the total penetration factor decreases gradually with Stokes number even at high values of the Stokes number (Figure 52). This difference appears to result from the cross-stream inertia that is imparted on the particles within the entrance region, which leads to the two peaks in the concentration profile at the channel entrance shown in Figure 50. Particles starting in the upper region of the inlet reservoir will quickly hit the bottom side of the channel due to the combination of particle inertia and gravity. However, particles starting in the lower region of the inlet reservoir will have vertical inertia that opposes the gravitational settling, which will delay the time required for the particles to settle to the channel bottom surface.

CHAPTER 5: CONCLUSION

Work in this thesis has examined both measurement and prediction of fluid and particle transport through narrow passages, such as through a crack in a window frame or door. Two different, but related, problems were addressed; the first concerning local measurement of the leakage flow rate through a crack and the second involving prediction of the entrance effect on particle penetration factor on passage through a crack. The next two sections of this conclusion focus on these different aspects of the thesis separately, followed by a discussion of possible applications of this research and of future work to be done.

5.1. Local Leakage Flow Rate Measurement

In Chapter 3 of this thesis, a new CO_2 tracer-gas method is proposed for local detection and characterization of leakage flow rates through a structure, such as a window or door, mounted on a flat surface. The leakage test for a given site can be conducted quickly (in a matter of a few minutes), merely by forming a vacuum within a test tank flooded with CO_2 and observing the change in CO_2 concentration as the pressure increases to atmospheric. Laboratory experiments using this approach for air leakage through a circular hole have been conducted, and a data analysis approach is developed by which to minimize measurement error. A careful uncertainty analysis and validation study of the experimental results was performed, both by comparison to predictions of numerical simulations and by comparison to empirical correlations available in the literature for this problem. The experimental

results are shown to be in close agreement with the numerical simulations and with four different empirical correlations found in the literature. This validation study confirms the utility of this leakage measurement approach, at least in controlled laboratory conditions. The uncertainty analysis also indicates the effect on the measured leakage flow rate of higher variation of system variables, which might be present in field implementations of this measurement approach.

5.2. Effect of Entrance Region on Particle Capture

In Chapter 4 of this thesis, a numerical study of particle collision and capture in the entrance region of a channel was performed for a computational domain that included the inlet reservoir, the channel, and the outlet reservoir. Different mechanisms of particle collision and capture within the entrance region were observed, depending on the values of the Stokes, Peclet, and Froude numbers. Some of these mechanisms resulted only in a small depletion of the total number of particles passing through the channel, whereas other mechanisms result in removal of a large percentage of the total particles. Collision of particles along the inlet channel wall just outside of the channel results in removal of only very few particles, and the number of particles captured via this mechanism decreased as the Stokes number increased, until the number vanished for a Stokes number of approximately unity.

For high Stokes number, the dominant particle capture mechanism within the entrance region was the collision of particles on the opposing channel wall,

which was caused by the particle cross-stream inertia generated by the radial flow field as the particle approached the entrance region. This inertial particle deposition mechanism was not included in previous studies of entrance region particle capture (e.g., Chen and Korjack, 1980) which do not include the inlet reservoir in the computational domain. For low values of the Peclet number, significant amount of particle deposition was observed to occur on the inlet reservoir wall just outside of the channel entrance due to the diffusive motion of the particles. Within the channel, the diffusive particle settling due to Brownian motion agreed reasonably well with the theory of Lee and Gieseke (1980).

A set of computations was also performed to investigate the assumption of penetration factor independence, which is commonly used to express the total penetration factor as a product of penetration factors associated with different effects, such as gravitational settling, Brownian motion, entrance region inertia, etc. If only gravitational settling and Brownian diffusion are considered, this assumption is always well satisfied since the Brownian penetration is very close to unity whenever the gravitational penetration factor is significantly less than unity, and vice versa. If entrance region effects are also considered, the situation is more complex. Specifically, we find that the assumption of penetration factor independence is well satisfied for problems with low Stokes and Peclet numbers, which are dominated by Brownian diffusion. For such cases the total penetration factor can be written as the product of the entrance region penetration factor (due to particle deposition on the inlet reservoir wall immediately outside the channel) and

the Brownian penetration factor (due to particle deposition inside the channel) with high accuracy.

For cases with Stokes number of order unity or higher and large values of Peclet number, the flow is controlled by particle inertia within the entrance region and gravitational settling. In such cases, the penetration factor independence assumption is found to substantially under-predict the total penetration factor. Indeed, many cases are noted in which the penetration factor independence assumption would yield zero total penetration factor, whereas direct computation yields penetration factors of between 0.15-0.20, where the difference can be attributed in part to inertial effects within the entrance region.

The current study shows that entrance effects can often have a significant influence on the penetration of particles through a crack. Entrance effects often increase the number of particles captured, resulting in a substantial decrease in the total penetration factor compared to what would be calculated without consideration of entrance effects. However, the effects of particle inertia within the entrance region on the particle concentration distribution within the channel can also give rise to nonlinear interaction of the particle deposition phenomena, resulting in some cases in an overall decrease in the number of particles captured, with associated increase in the total penetration factor. For these reasons, it is important to include entrance effects in determination of the total penetration factor for particle infiltration studies, particularly for cases with Stokes number equal to unity or greater.

These results can be used to further examine the work performed by Mosley et al. (2001). While the physical description of the experiment is not fully complete for which an accurate approximation of entrance penetration factor can be found, a range of Stokes numbers, and therefore a range of possible penetration factors, can be estimated. Values of flow rates and velocities of fluid traveling through the crack site were incomplete or totally lacking, which caused the need for such estimation. For trials performed with larger particle diameters by Mosley et al. (2001), Stokes numbers could be in the range of St = 1-5. If even larger particle diameter values up to $d/H = 0.015$ were used, which Mosley et al. (2001) did not test, this approximate Stokes number value could reach up to 10. This puts those larger particle diameter trials in the high Stokes number region discovered to induce significant reduction in entrance penetration factor, and could be a validation of the hypothesis that the prior model (which negates entrance effects) caused the disparity between the experimental and analytical results reported by Mosley et al. (2001).

5.3. Applications and Future Work

The work conducted in this thesis has addressed two important problems of the general area of fluid and particle infiltration into buildings or structures via passage through narrow cracks or gaps. The methods and knowledge gained through this investigation can help better analyze individual leakage sites and quantify the ability of building and structural envelopes for prevention of particle

infiltration. For the local leak detection method, leakage rates through individual sites can be identified and thus judgments made if there is a need to replace part of a structure (e.g., a window unit) or better seal the area to prevent air infiltration. Previous leakage testing methods for building air infiltration lack this ability. Localized leakage measurement can be especially helpful in cases such as historic buildings, in which the building envelope could be compromised due to age of the structure. With the case of an historic building, an entire overhaul to modern windows would harm the historic character of the building. Accurate local quantification of air leakage could therefore be used to selectively repair leakage sites while maintaining the building's historic characteristics. The robustness of this leakage measurement technique also implies that it can be applied to leakages sites other than that of buildings, such as for testing leaks from compressed gas containers.

The work presented in Chapter 3 of this thesis discusses an experimental validation of the leakage testing methodology conducted in the laboratory. The major next step in this research would be the design of a device to work in the field. Central to this design would be a method to seal the test chamber to the leakage area. Areas of high leakage, such as windows, can have a number of related, complex geometries other than a flat surface, for which the laboratory test model was designed to use. This potential uneven geometry has great potential for leakages of the testing apparatus itself. Windows also vary in size immensely, so a field model would have to be able to test leakage areas of multiple sizes and

dimensions. A potential change could be the implementation of a soft or flexible sealing joint that could fit over a number of surfaces. In the instance that a 'perfect' seal cannot be made, the testing procedure could be modified in such a way as to include a calibration run to test for residual leakage in the sealing fixture.

The numerical analysis into particle capture during transport through cracks, outlined in Chapter 4, has led to new insight into fundamental mechanisms of particle capture within the crack entrance region. With a better understanding of particle capture physics, the effectiveness in mitigating harmful particle transport by a building envelope of fluid barrier can better be modeled. The assumption of penetration factor independence, used in a number of previous studies, was found to be violated for certain with large particle Stokes numbers, as might be typical of dust particles in air. This knowledge can help improve models for penetration factor and help explain observed deviations of existing penetration factor models with experimental data.

In future work, the numerical results found in this study could be validated with careful experimental results focused on the entrance region effect. Laboratory tests of particle infiltration through cracks could be performed in which particle tracking is used to examine entrance inertial effects on particle-wall collisions. The results from both simulations and experiments could be used to create correlations (equations) which could estimate the entrance penetration factor as a function of relevant flow parameters (St, Pe, Fr, etc.). Such correlations would allow more accurate prediction of building envelope particle infiltration. Approximation of

crack flow rate conditions (such as using (2.6) and (2.7)) and crack density can be used in conjunction with new penetration factor correlations to accurately model building envelope filtration. For examination of individual leakage sites, the testing apparatus presented in Chapter 3 could be used in conjunction with correlations of particle penetration from Chapter 4 to estimate local particle penetration from potentially high leakage sites. For example, if most of a building has relatively low leakage rate but a few sites have significant leakage, local indoor particle concentrations could be high even if building-wide leakage testing might indicate otherwise. The work in Chapters 3 and 4 could be used to obtain a much more accurate approximation for potentially harmful indoor particle concentrations for such a situation.

REFERENCES

[1]. Ahmed, A., Tripathi, S.K., Sawant, P.S., Muhkarjee, D., and Shah, B.K.. (2012). In-service leak testing of vacuum furnace. Journal of Physics: Conference Series, 390 (012048).

[2]. Alzona, J., Cohen, B.L., Rudolph, H., Jow, N.H., and Frohliger, J.O.. (1979). Indoor-outdoor relationships for airborne particulate matter of outdoor origin. Atmospheric Environment, 13, 55-60.

[3]. ASHRAE Fundamentals Handbook, Chapter 22. (1997). American Society of Heating Refrigeration and Air-conditioning Engineers, Atlanta, Georgia.

[4]. ASTM Standard E741. (2011). Standard test method for determining air change in a single zone by means of tracer gas dilution. West Conshohocken, PA, ASTM International.

[5]. ASTM Standard E779. (2011). Standard test method for determining air leakage rate by fan pressurization. West Conshohocken, PA, ASTM International.

[6]. ASTM Standard E1186. (2011). Standard practices for air leakage site detection in building envelopes and air barrier systems. West Conshohocken, PA, ASTM International.

[7]. ASTM Standard E1827. (2011). Standard test method for determining air tightness of buildings using an orifice blower door. West Conshohocken, PA, ASTM International.

[8]. Arden-Pope, C. and Dockery, D.W.. (2006). Health effects of fine particulate air pollution: lines that connect. Journal of the Air and Waste Management Association, 56 (6), 709-742.

[9]. Bagchi, P. and Balachandar, S.. (2002). Effect of free rotation on the motion of a solid sphere in linear shear flow at moderate Re. Physics of Fluids, 14(8), 2719-2737.

[10]. Bévenot, X., Trouillet, A., Veillas, C., Gagnaire, H., and Clément, M.. (2000). Hydrogen leak detection using optical fibre sensor for aerospace applications. Sensors and Actuators B: Chemical, 67 (1-2), 57-67.

[11]. Bomelburg, H.. (1977). Estimation of gas leak rates through very small orifices and channels. Technical Report BNWL-2223 / NRC-12, Nuclear Regulatory Commission.

[12]. Chen, R.Y. and Korjack, T.A.. (1980). Deposition of suspensions in the entrance region of a vertical channel. Powder Technology, 25, 121-124.

[13]. De Marcus, W. and Thomson, J.W.. (1954). Theory of a diffusion battery. Atomic Energy Commission.

[14]. Dockery, D.W., and Spengler, J.D.. (1981). Indoor-outdoor relationships of respirable sulfates and particles. Atmospheric Environment, 15 (3), 335-343.

[15]. Etheridge, D.W.. (1977). Crack flow equations and scale effect. Building Environment, 12, 181-189.

[16]. Fang, X.. (1999). Advances in fixed area expansion devices. Technical Report ACRC CR-20, Air Conditioning and Refrigeration Center, University of Illinois.

[17]. Fox, C.G. and Alder, J.F.. (1989). Surface acoustic wave sensors for atmospheric gas monitoring. Techniques and Mechanisms in Gas Sensing, Adam Hilger, Bristol.

[18]. Fuchs, C.N.. (1964). The Mechanics of Aerosols. New York; Pergamon Press, 108-110.

[19]. Gross, D.. (1991). Estimating air leakage through doors for smoke control. Fire Safety Journal, 17, 171-177.

[20]. Gross, D. and Haberman, W.. (1988). Analysis and prediction of air leakage through door assemblies. Proceedings of the Second International Symposium on Fire Safety Science, pp. 169-178.

[21]. Hodgkinson, J., Shan, Q., and Pride, R.D.. (2006). Detection of a simulated gas leak in a wind tunnel. Measurement Science and Technology, 17, 1586-1593.

[22]. Holand, S., Chimenti, D.E., Roberts, R., and Strei, M.. (2007). Locating leaks in manned spacecraft using structure-born noise. Journal of the Acoustic Society of America, 121 (6), 3484-3492.

[23]. Joint Committee for Guides in Metrology. (2008). Evaluation of measurement data – Guide to the expression of uncertainty in measurement. Bureau International des Poids et Mesures.

[24]. Jones, J., McMullen, M.J., and Dougherty, J.. (1987). Toxic smoke inhalation: Cyanide poisoning in fire victims. The American Journal of Emergency Medicine, 5 (4), 17-21.

[25]. Lai, Y.G.. (2000). Unstructured grid arbitrarily shaped element method for fluid flow simulation. AIAA Journal, 38(12), 2246-2252.

[26]. Lee, K.W. and Gieseke, J.A.. (1980). Simplified calculation of aerosol penetration through channels and tubes. Atmospheric Environment, 14, 1089-1094.

[27]. Liddament, M.W. and Orme, M.. (1998). Energy and ventilation. Applied Thermal Engineering, 18 (11), 1101-1109 (9).

[28]. Liu, D.L. and Nazaroff, W.W.. (2001). Modeling pollutant penetration across building envelopes. Atmospheric Environment, 35, 4451-4462.

[29]. Lyberg, M.D.. (1997). Basic air infiltration. Building and Environment, 32 (2), 95-100.

[30]. Maqsood, M., Ali, J., Usman, A., and Farooq, M.. (2013). Design and development of primary plate orifice flowmeter. Journal of Physics: Conference Series, 439 (012035).

[31]. Marple, V.A. and Willeke, K.. (1976). Impactor Design. Atmospheric Environment, 10, 891-896.

[32]. Marshall, J.S. and Li, S.. (2014). Adhesive Particle Flow: A Discrete Element Approach. Cambridge University Press, New York.

[33]. McMaster, R.C.. (1982). Nondestructive testing handbook. Volume 1 – Leak testing.

[34]. Morgado, I., Legras, J.C., and Clodic, D.. (2010). Primary standard for the calibration of refrigerant leak flow rates. Metrologia, 47 (3), 135.

[35]. Mosley, R.B., Greenwell, D.J., Sparks, L.E., Guo, Z., Tucker, W.G., Fortmann, R., and Whitfield, C.. (2001). Penetration of ambient fine particles into the indoor environment. Aerosol Science and Technology, 34, 127-136.

[36]. Orszag, S.A. and Gottlieb, D.. (1980). Approximation Methods for Navier-Stokes Problems. Lecture Notes in Mathematics **771**, 381-398

[37]. Owen, M.K. and Ensor, D.S.. (1992). Airborne particle sizes and sources found in indoor air. Atmospheric Environment, 26 (12), 2149-2162.

[38]. Perry, R.H. and Green, D.W.. (1984). Perry's Chemical Engineers' Handbook, 6ed ed., McGraw-Hill, New York.

[39]. Ramamurthi, K. and Nandakumar, K.. (1999). Characteristics of flow through small sharp edged orifices. Flow Measurement and Instrumentation, 10, 133-143.

[40]. Sandberg, M. and Blomqvist, C.. (1985). A quantitative estimate of the accuracy of tracer gas methods for the determination of the ventilation flow rate in buildings. Building and Environment, 20(3), 139-150.

[41]. Sarnat, S.E., Coull, B.A., Ruiz, P.A., Koutrakis, P., and Suh, H.H.. (2006). The influence of ambient particle composition and size on particle infiltration

in Los Angeles, CA, residences. Journal of the Air and Waste Management Association, 56 (2), 186-196.

[42]. Sheen, S.H., Chien H.T., Apostolos C.R.. (2000). Ultrasonic techniques for detecting helium leaks. Sensors and Actuators B, 71, 197-202.

[43]. Sherman, M.H.. (1980). Air infiltration in buildings. University of California at Berkley, University Microfilm, ([LBL-10712]).

[44]. Sherman, M.H.. (1987). Estimation of infiltration from leakage and climate indicators. Energy and Buildings, 10, 81-86.

[45]. Sherman, M.H.. (1988). Uncertainty in airflow calculations using tracer-gas measurements. Building Environment, 24 (4), 347-354.

[46]. Sherman, M.H. and Palmiter, L.. (1995). Uncertainties in fan pressurization measurements. In: Modera M.P., Persily A.K., editors. Airflow Performance of Building Envelopes, Components, and Systems, no. 1225, 266-278.

[47]. Slade, D.H.. (1968). Meteorology and Atomic Energy. Atomic Energy Commission, 364-366.

[48]. Thatcher, T.L. and Layton, D.W.. (1995). Deposition, resuspension, and penetration of particles within a residence. Atmospheric Environment, 29 (13), 1487-1497.

[49]. Tung, T.C.W., Chao, C.Y.H., and Burnett, J.. (1999). A methodology to investigate the particulate penetration coefficient through building shells. Atmospheric Environment, 33, 881-893.

[50]. Walker, I.S. and Wilson, D.J.. (1993). Evaluating models for superposition of wind and stack effect in air infiltration. Building and Environment, 28 (2), 201-210.

[51]. Yeung, P.K. and Pope, S.B.. (1988). An algorithm for tracking fluid particles in numerical simulations of homogenous turbulence. Journal of Computational Physics, 79, 373-416.